Point-by-Point Response to Co-Editor Comments, Including Relevant Changes Made in the Manuscript, and Marked-Up Manuscript and Supplement

J. S. Wang et al.

Co-editor's comments below are in *italics*, and our responses are in regular text style.

Dear James,

Thank-you for the work that you and your co-authors have undertaken to address the reviewers comments on your manuscript. Overall I think you have answered the majority of the concerns sufficiently. There are a small number of comments that I think could benefit from some further minor revisions, particularly where more than one reviewer raised an issue. In addition, my re-reading of the manuscript identified some technical corrections.

Thanks very much for your careful and helpful review of our manuscript, Rachel. We have made many of the changes you suggested. Please see our individual responses below.

Description of uncertainties*: Each reviewer asked for clarification around the observation uncertainties. Adding the model-data mismatch in Table S1 is helpful, but we still do not get a sense of how much that element contributes to the total uncertainty (which I suspect contributes to the confusion of reviewers 2 and 3 about the minimum of 0.01 ppm), or how the flask uncertainties compare to those from the continuous in-situ data or the satellites. I suggest adding a column to Table S1 to give the mean (total) uncertainty for each site (with the factor 2 inflation) so that the reader understands how much the between-flask variability adds to the model-data mismatch, and how the mean uncertainty on the 30s or 1 hour observations compares. With this extra information, I think the reference to the 0.01 ppm minimum could be removed since it presumably has no significant impact on the total uncertainty, which in that case will be dominated by the model-data mismatch. In this case, I suggest the following revision to the paragraph starting at line 228:*

'We estimate the uncertainties for the flask-air observations as the root sum square (RSS) of two components: (a) the standard deviation of the observations from multiple flasks within that hour or 0.3 ppm if there is only one sample and (b) a simple estimate of model transport/representation error. The transport/representation error … from 0.4 to 4 ppm (Table S1). For the continuous measurements, we take the RSS of two components: (a) the afternoon root mean square (RMS) of the uncertainties [replace with standard deviation?] of the 30-second (NOAA) or hourly (JMA) observations divided by the square root of the number of observations, and (b) the standard deviation of all the 30-second/hourly …. In addition, we enlarged all in situ … by a factor of 2 (mean values in Table S1)…'

It would also be useful to include the typical uncertainty applied to the GOSAT data. I suggest adding an extra sentence at line 271 perhaps giving the mean, minimum and maximum uncertainty used for

the GOSAT data, possibly divided into land and ocean data if they are different (as implied by the different inflation factors).

As you suggested, we have added a column to Table S1. We've also made most of the suggested revisions to the paragraph, including removing the reference to the 0.01 ppm minimum and adding the references to Table S1. Finally, we've calculated the mean, minimum and maximum uncertainty for GOSAT data, separately for land and ocean, and added a sentence in the text providing this information.

Global total source difference between inversions*: I remain curious about the large difference in global flux in the June-May period. Given your comment about the sensitivity to period being considered, I wonder if that points mostly to retrieval bias as the cause of the difference, particularly given the northern Africa issue that you raise in relation to Fig 6, and that most of the in-situ/GOSAT difference is found in the tropics.*

We think that both satellite retrieval bias and the surface-only sampling of the in situ data set could contribute to the difference, as we suggested in our response to the reviewers. Note that a constant retrieval bias over time would not cause a difference in inferred annual atmospheric growth rate; rather, there would need to be a trend or interannual variability in bias. For a short period such as a year, incomplete sampling of the atmosphere in combination with natural interannual variability in fluxes can presumably result in large differences in total fluxes inferred from different observing systems. We now add the phrase "e.g. total column vs. surface only" after "given their sampling of different regions of the atmosphere" in the first paragraph of Section 3.2 (line 567). We also add the following sentence in lines 568-570: "In addition, the GOSAT data may be affected by modest trends and interannual variability in biases, as reported by Kulawik et al. (2016)."

Also, as we pointed out in our response to the third reviewer (regarding lines 734-735), the in situ + GOSAT inversion results suggest that there is some degree of independence of the GOSAT-inferred tropical regional result from the global result.

Length of paper*: At least two reviewers mention the length of the text or suggest where it could be compacted, and I also agree that it is a long paper. Although you have moved two figures to the supplementary material and removed some text, the additions in response to other comments have made the results section longer than originally. While ultimately the choice is yours, I think that a shorter paper is more likely to be read, and gives more focus to your main points. Here are some suggested deletions:*

- *Delete sentence 'Our objectives …' (line 31-34) from abstract*

  OK, done.
- *Figure 2 could be reduced (to one flask and one continuous site) and/or moved to supplementary material, given that it is barely discussed in the text. For those, like me, who are much less familiar with the satellite data, the figure would be more interesting if it included satellite data from an ocean grid-cell and a well-sampled land grid-cell, especially if it these were chosen to be close to an in-situ site.*

We have reduced the figure by half so that it fits on a single page. We would prefer to keep it in the main body rather than the supplement, since it is discussed in three separate places in the text, including in the transport model description (Section 2.3). To keep the figure small and avoid introducing additional discussion, we have decided not to add point comparisons with satellite data. However, we think the existing Fig. 3 provides an informative and visually effective summary of model-GOSAT data comparison over the entire data set.

- *How useful is Figure 5 and the associated discussion (line 471-499) for the main message of the paper? Apart from highlighting that you solve for fluxes every 8 days, it mostly just shows noisier versions of the results presented in Fig 6 – and as noted by at least one reviewer, since the uncertainties are not shown on Fig 5 (while they are on Fig 6), it is not easy to assess how much of the week to week fluctuations are outside the uncertainty range anyway. If this text is deleted, also delete 'Again' from line 683.*

  Although this discussion may not be critical for presentation of our main messages, we believe it provides important background for the issues of temporal fluctuations and error correlations in the fluxes that are brought up later in the paper. Given that the feature of large fluctuations in the in situ inversion results can be seen in the monthly means in Figs. 6 and 7, we think it's important for the explanation to also show results at the original temporal resolution of the inversion, i.e. 8 days. The discussion here provides quantitative information on how much of the variance in the results is "real" (signal) and how much is spurious (noise), and on the degree of complementarity of the in situ and GOSAT data sets. Besides, we thought it would be of interest to present at least some results at the original resolution, given that we highlight our relatively high flux optimization resolution in the Introduction and elsewhere. (As for the original spatial resolution, the 2010-2009 flux difference maps in Fig. 13 give readers a sense of that.)

- *Line 504-507: I don't think the shift in sink is easily seen in Figure 6, so I suggest deleting this sentence and only discussing the shift in Sec 3.2. If this change is made, delete 'As was noted earlier in Section 3.1' at line 572.*

  We agree that the shift in sink is not easily seen in the figure, and we have deleted that sentence as well as the reference to it at line 572. In order to put the "unusual features" in the following sentence in a larger context, we modify that sentence thus: "The GOSAT inversion exhibits systematic differences from the prior and the in situ inversion, together with some unusual features."

- *Line 520-554 and Figure 7: I think this section is less important than other parts of the paper since it is not relevant to the GOSAT inversion, only the in-situ one. The comparison to CT2013B could be restricted to Sec 3.2. Some of the information about the CT2013B inversion would need to be moved but it may be sufficient to give a reference rather than as much detail as is currently included.*

  There are several reasons we would like to keep this section; however, we will remove some less relevant material. Although the comparison of our in situ posterior fluxes with CT2013B here may be somewhat mundane, we think it's useful to show these monthly fluxes first before showing the longer-term mean fluxes in Section 3.2, to give a better idea of where

the inversions are similar and where they differ. Furthermore, although this section is not directly relevant to the GOSAT inversion, it points out the effect of CT2013B's tight priors in restricting flux adjustments, especially for the ocean; this becomes important in the discussion in Section 3.3 of the large ocean sink in our results for both the GOSAT and the in situ inversion and the connection to flux error correlations. In addition, this section provides further discussion on the size of temporal fluctuations of in situ posterior fluxes, which was first brought up earlier in Section 3.1.

We delete several lines of text with details on the observation sites and flux optimization regions used in CT2013B, and instead add a very brief description of the flux regions in the second sentence of the paragraph.

- *Delete all the flux numbers from line 575-578 and line 583-586, since readers can find these in the Table if they are interested in the detail.*
  OK, done. (We added the word "notable" in the first set of lines to indicate that only the regions making major contributions to the shift are listed here.)
- *The prior could be dropped from Fig 9 to simplify the figure, and the sentence (line 614-616) deleted.*
  Although the prior could indeed be dropped from the figure without major impact, the omission would make the figure inconsistent with Fig. 10 (comparison with HIPPO), where the prior is included and figures somewhat more prominently in the discussion. In addition, the point in lines 614-616 about the prior mole fractions being generally too high is not made explicitly anywhere else in the paper; thus, we think it's worthwhile to keep the sentence.
- *Fig 13. You have said (line 839-840) that you are focussing this analysis on the GOSAT inversion, so perhaps delete the left and middle column from Fig 13 and only show the GOSAT posterior. In this case, lines 844-846 could be deleted.*
  We think it is still useful to include the prior and in situ inversion flux maps, since they provide a contrast to the GOSAT inversion map, in which a positive flux anomaly over western Russia is more apparent. Furthermore, one of our main findings is that the CASA-GFED prior may give a more accurate interannual flux difference over that region than the possibly exaggerated GOSAT inversion results, so it is necessary to include the prior in the figure and the discussion.
- *Line 917-918: delete the sentence in parentheses, since you've already said you are focussing on the GOSAT inversion.*
  Our earlier statement about focusing on the GOSAT inversion is actually specific to the case of the northern summer heat waves and fires. In between that case and the one on the Amazon drought that lines 917-918 refer to, we discuss another case, anomalous wetness in North America, for which we state that we consider the in situ inversion result to be reliable and thus report it along with the GOSAT inversion result. So we think it is reasonable to mention during the Amazon discussion our reason for not reporting the in situ results for this particular region.
- *Line 966-967: delete 'a shift in the … in situ inversion' and replace ';' with ','*
  OK, done.

- *Fig 11. Since the figures are symmetric in the diagonal, could the two panels be combined with the in-situ inversion in the top-right and the GOSAT inversion in the bottom left?*
  OK, done.

Technical corrections:

- *Line 112: I think you can claim higher temporal resolution than other batch inversions but not higher spatial resolution. Rayner et al, GBC, 2008 included batch inversions with 146 and 116 regions.*

  OK, we have added the word "most" between "relative to" and "previous batch inversions". We also make that change later on at the beginning of Section 2.
- *Line 180-182. Suggest moving this sentence to line 192, and delete 'discussed below'.*
  OK, done.
- *Line 188-189. Suggest re-writing the sentence starting 'The total amount …' as 'Together these oxidation emissions are estimated to be ~ 1Pg C y^{-1} (for year 2006; Nassar et al., 2010).'*
  OK, done.
- *Line 208: add reference to Table S1 after Fig 1a.*
  Done.
- *If Figure 7 retained, Replace first sentence of paragraph (line 520-521) with sentence starting 'Results from our …' (line 535-537) and add 'In Fig. 7,' before 'the two sets …' in line 537.*
  OK, we have made those changes.
- *Line 618, add '(Fig 10)' after 'Pacific'*
  Done.
- *Line 620, replace 'seen in the' with 'seen in Fig. 9 for'*
  Done.
- *Line 650-653: I am not sure whether this explanation for the better fit of the high altitude data is correct. In either inversion, it is only ever surface fluxes that are adjusted, so any signal at higher altitude must be driven by the lower level concentrations. In the GOSAT case it seems difficult to explain how the 800-300 hPa data can be too low but the 300-150 hPa data are OK while the opposite is seen for the in-situ inversion but both inversions use the same transport. Perhaps the age of the air at 300-150 hPa is important and maybe any fitting of the initial condition?*

  We agree that this explanation was not completely correct. For one thing, bias in a GOSAT column average retrieval should affect all altitudes, so a comparison of model concentrations resulting from assimilation of GOSAT data with aircraft observations would presumably show a similar bias at all altitudes. However, the feature in question is seen mainly at high latitudes, where there are few GOSAT retrievals during the times of year of the HIPPO missions (fall and spring), especially over the ocean; even at lower latitudes, there are relatively few observations over the ocean. Thus, the surface flux adjustments in these

regions are driven largely by flux error correlations rather than directly by local observations. Together with the fact that air parcels at different altitudes can have different origins, this allows for the possibility of posterior concentrations disagreeing with aircraft observations at lower altitudes while agreeing at higher altitudes. A possible explanation for the better agreement at higher altitudes is that, as we explained in the text, air parcels at higher altitudes consist of mixtures of air originating from broader areas of the surface, so that regional flux errors may cancel out (e.g. due to combining of negatively correlated errors). Similarly, the posterior concentrations for the in situ inversion can disagree with aircraft observations higher up even if they agree closer to the surface because of different air origins and the fact that no upper-air observations are assimilated.

We have rewritten this section of the manuscript, incorporating an improved explanation. Note that our original statement about in situ inversion concentrations staying close to the prior because of a lack of high-altitude constraints is not necessarily true, so we have revised it to say that the inversion should not be expected to improve agreement with high-altitude aircraft observations given that it does not assimilate any observations at those altitudes.

As for the suggestion that the fitting of the initial condition could have an important influence on the posterior concentrations at high altitudes, the adjustments of the initial condition and offset parameters are actually significantly larger in our in situ inversion results than in our GOSAT inversion, so that doesn't seem to explain the larger overall concentration adjustments at high altitudes in the GOSAT inversion.

- *Line 778: suggest add 'slightly' before 'better'.*
  OK, done.
- *Figure 6 caption: perhaps note how monthly means are constructed from 8 day fluxes.*
  OK, we've added a sentence.
- *Figure 10 caption: now that you have added labels (a-f) on the panels, these should be referenced in the caption.*
  Done.

Please feel free to contact me by email if any of these comments are not clear.

Regards,

Rachel Law, rachel.law@csiro.au

A Global Synthesis Inversion Analysis of Recent Variability in CO_2 Fluxes Using GOSAT and In Situ Observations

James S. Wang,[1,2] S. Randolph Kawa,[2] G. James Collatz,[2] Motoki Sasakawa,[3] Luciana V. Gatti,[4] Toshinobu Machida,[3] Yuping Liu,[5,2] and Michael E. Manyin[5,2]

[1]Universities Space Research Association, Columbia, MD, USA, james.s.wang@nasa.gov

[2]NASA Goddard Space Flight Center, Greenbelt, MD, USA

[3]National Institute for Environmental Studies, Center for Global Environmental Research, Ibaraki, Tsukuba Onogawa, Japan

[4]Instituto de Pesquisas Energéticas e Nucleares (IPEN)–Comissao Nacional de Energia Nuclear (CNEN), Sao Paulo, Brazil

[5]Science Systems and Applications, Inc., Lanham, MD, USA

Submitted to Atmospheric Chemistry and Physics (as part of Special Issue "The 10th International Carbon Dioxide Conference (ICDC10) and the 19th WMO/IAEA Meeting on Carbon Dioxide, other Greenhouse Gases and Related Measurement Techniques (GGMT-2017)")

Abstract

The precise contribution of the two major sinks for anthropogenic CO_2 emissions, terrestrial vegetation and the ocean, and their location and year-to-year variability are not well understood. Top-down estimates of the spatiotemporal variations in emissions and uptake of CO_2 are expected to benefit from the increasing measurement density brought by recent in situ and remote CO_2 observations. We uniquely apply a batch Bayesian synthesis inversion at relatively high resolution to in situ surface observations and bias-corrected GOSAT satellite column CO_2 retrievals to deduce the global distributions of natural CO_2 fluxes during 2009-2010. ~~Our objectives include evaluating bottom-up prior flux estimates, assessing the value added by the satellite data, and examining the impacts of inversion technique and assumptions on posterior fluxes and uncertainties.~~ The GOSAT inversion is generally better constrained than the in situ inversion, with smaller posterior regional flux uncertainties and correlations, because of greater spatial coverage, except over North America and northern and southern high-latitude ocean. Complementarity of the in situ and GOSAT data enhances uncertainty reductions in a joint inversion; however, remaining coverage gaps, including those associated with spatial and temporal sampling biases in the passive satellite measurements, still limit the ability to accurately resolve fluxes down to the sub-continental/sub-ocean basin scale. The GOSAT inversion produces a shift in the global CO_2 sink from the tropics to the north and south relative to the prior, and an increased source in the tropics of ~2 Pg C y^{-1} relative to the in situ inversion, similar to what is seen in studies using other inversion approaches. This result may be driven by sampling and residual retrieval biases in the GOSAT data, as suggested by significant discrepancies between posterior CO_2 distributions and surface in situ and HIPPO mission aircraft

46 data. While the shift in the global sink appears to be a robust feature of the inversions, the
47 partitioning of the sink between land and ocean in the inversions using either in situ or GOSAT
48 data is found to be sensitive to prior uncertainties because of negative correlations in the flux
49 errors. The GOSAT inversion indicates significantly less CO_2 uptake in summer of 2010 than in
50 2009 across northern regions, consistent with the impact of observed severe heat waves and
51 drought. However, observations from an in situ network in Siberia imply that the GOSAT
52 inversion exaggerates the 2010-2009 difference in uptake in that region, while the prior CASA-
53 GFED model of net ecosystem production and fire emissions reasonably estimates that quantity.
54 The prior, in situ posterior, and GOSAT posterior all indicate greater uptake over North America
55 in spring to early summer of 2010 than in 2009, consistent with wetter conditions. The GOSAT
56 inversion does not show the expected impact on fluxes of a 2010 drought in the Amazon;
57 evaluation of posterior mole fractions against local aircraft profiles suggests that time-varying
58 GOSAT coverage can bias estimation of flux interannual variability in this region.
59

1. Introduction

About one-half of the global CO_2 emissions from fossil fuel combustion and deforestation accumulates in the atmosphere (Le Quéré et al., 2015), where it contributes to global climate change. The rest is taken up by land vegetation and the ocean. The precise contribution of the two sinks, their location and year-to-year variability, and the environmental controls on the variability are, however, not well understood. Top-down methods involving atmospheric inverse modeling have been used extensively to quantify natural CO_2 fluxes (e.g. Enting and Mansbridge, 1989; Ciais et al., 2010). An advantage of this approach over bottom-up methods such as forest inventories (Pan et al., 2011; Hayes et al., 2012) or direct flux measurements (Baldocchi et al., 2001; Chevallier et al., 2012) is that measurements of atmospheric CO_2 mole fractions generally contain the influence of fluxes over a spatial scale substantially larger than that of individual forest plots or flux measurements, so that errors from extrapolating measurements to climatically relevant scales (e.g. ecosystem, sub-continental, or global) are mitigated. However, the accuracy of top-down methods is limited by incomplete data coverage (especially for highly precise but sparse in situ observation networks), uncertainties in atmospheric transport modeling, and mixing of signals from different flux types such as anthropogenic and natural.

With the advent of retrievals of atmospheric CO_2 mole fraction from satellites, including the Japanese Greenhouse gases Observing SATellite (GOSAT) (Yokota et al., 2009) and the NASA Orbiting Carbon Observatory-2 (OCO-2) (Crisp, 2015; Eldering et al., 2017), data coverage has improved substantially. Making measurements since 2009, GOSAT is the first satellite in orbit designed specifically to measure column mixing ratios of CO_2 (as well as

82 methane) with substantial sensitivity to the lower troposphere, close to surface fluxes. A number
83 of modeling groups have conducted CO_2 flux inversions using synthetic GOSAT data (Liu et al.,
84 2014) and actual data (Takagi et al., 2011; Maksyutov et al., 2013; Basu et al., 2013; Saeki et al.,
85 2013a; Deng et al., 2014; Chevallier et al., 2014; Takagi et al., 2014; Reuter et al., 2014;
86 Houweling et al., 2015; Deng et al., 2016). Unlike in situ measurements, which are calibrated
87 directly for the gas of interest, remote sensing involves challenges in precision and accuracy
88 stemming from the measuring of radiance. The retrievals rely on modeling of radiative transfer
89 involving complicated absorption and scattering by the atmosphere and reflection from the
90 surface (e.g. Connor et al., 2008; O'Dell et al., 2012). Passive measurements that rely on
91 reflected sunlight are more prone to errors than active measurements, as they are affected by not
92 only errors related to meteorological parameters and instrument noise but also systematic errors
93 related to scattering by clouds and aerosols, which can dominate the error budget (Kawa et al.,
94 2010; O'Dell et al., 2012). Furthermore, passive measurements have coverage gaps where there
95 is insufficient sunlight and where there is excessive scattering.
96 In addition to the model transport examined by a number of inversion intercomparison
97 studies (e.g. Gurney et al., 2002; Baker et al. 2006), the inversion technique and assumptions can
98 contribute to substantial differences in results. For example, Chevallier et al. (2014) found that
99 significant differences in hemispheric and regional flux estimates can stem from differences in
100 Bayesian inversion techniques, transport models, a priori flux estimates, and satellite CO_2
101 retrievals. Houweling et al. (2015) presented an intercomparison of 8 different inversions using
102 5 independent GOSAT retrievals, and also found substantial differences in optimized fluxes at

103 the regional level, with modeling differences (priors, transport, inversion technique) contributing
104 approximately as much to the spread in results on land as the different satellite retrievals used.
105 In this paper, we present inversions of GOSAT and in situ data using a distinct technique,
106 which are compared with results from other studies. All of the previous GOSAT satellite data
107 inversions have used computationally-efficient approaches, such as variational and ensemble
108 Kalman filter data assimilation, to handle the large amounts of data generated by satellites and
109 the relatively large number of flux regions whose estimation is enabled by such data. The
110 computational efficiency of these approaches results from numerical approximations. In this
111 study, we apply a traditional, batch, Bayesian synthesis inversion approach (e.g. Baker et al.,
112 2006) at high spatiotemporal resolution relative to most previous batch inversions to estimate
113 global, interannually varying CO_2 fluxes from satellite and in situ data. Advantages of this
114 technique include generation of an exact solution along with a full-rank error covariance matrix
115 (e.g. Chatterjee and Michalak, 2013), and an unlimited time window during which fluxes may
116 influence observations, unlike the limits typically imposed in Kalman filter techniques. The
117 major disadvantages of the batch technique are that computational requirements limit the
118 spatiotemporal resolution at which the inversion can be solved and the size of the data set that
119 can be ingested, a large number of transport model runs is required to pre-compute the basis
120 functions (i.e. Jacobian matrix), and the handling of the resulting volume of model output is very
121 time-consuming at relatively high resolution.
122 We estimate natural terrestrial and oceanic fluxes over the period May 2009 through
123 September 2010. The analysis spans two full boreal summers; longer periods were prohibited by
124 the computational effort. The objectives of this study are: 1) to understand recent variability of

125 the global carbon cycle, 2) to evaluate the bottom-up flux estimates used for the priors, 3) to
126 compare fluxes and uncertainties inferred using in situ observations, GOSAT observations, and
127 the two data sets combined and to assess the value added by the satellite data, and 4) to generate
128 inversion results using a unique Bayesian inversion technique for comparison with other
129 approaches.

130 Section 2 provides details on the inputs and inversion methods. Section 3 presents prior
131 and posterior model CO_2 mole fractions and their evaluation against independent data sets, fluxes
132 and uncertainties at various spatial and temporal scales, and comparisons with results from
133 inversions conducted by other groups. We discuss the robustness of results, and examine in
134 particular their sensitivity to assumed prior flux uncertainties. We then analyze the possible
135 impacts of several climatic events during the analysis period on CO_2 fluxes. Section 4 contains
136 concluding remarks.

137

138

139 **2. Methods**

140 Our method is based on that used in the TransCom 3 (TC3) CO_2 inversion
141 intercomparisons (Gurney et al., 2002; Baker et al. 2006) and that of Butler et al. (2010), the
142 latter representing an advance over the TC3 method in that they accounted for interannual
143 variations in transport and optimized fluxes at a higher spatial resolution. Our method involves
144 further advances over that of Butler et al. (2010), including higher spatial and temporal
145 resolution for the optimized fluxes, and the use of individual flask-air observations and daily
146 averages for continuous observations rather than monthly averages. Inversion theoretical studies

147 and intercomparisons have suggested that coarse resolution for flux optimization can produce
148 biased estimates, i.e. estimates that suffer from aggregation error (Kaminski et al., 2001; Engelen
149 et al., 2002; Gourdji et al., 2012). Although observation networks may not necessarily provide
150 sufficient constraints on fluxes at high resolutions, Gourdji et al. (2012) adopted the approach of
151 estimating fluxes first at fine scales and then aggregating to better-constrained resolutions to
152 minimize aggregation errors. The high spatiotemporal resolution of our inversion relative to
153 most other global batch inversions would be expected to reduce aggregation errors. Similarly,
154 use of higher temporal resolution observations allows our inversion to more precisely capture
155 variability due to transport and thus more accurately estimate fluxes. Details on our inversion
156 methodology are provided in the sub-sections below.
157
158 2.1. A priori fluxes and uncertainties
159 Prior estimates for net ecosystem production (NEP = photosynthesis − respiration) and
160 fire emissions (wildfires, biomass burning, and biofuel burning) come from the Carnegie-Ames-
161 Stanford-Approach (CASA) biogeochemical model coupled to version 3 of the Global Fire
162 Emissions Database (GFED3) (Randerson et al., 1996; van der Werf et al., 2006; 2010). CASA-
163 GFED is driven with data on fraction of absorbed photosynthetically active radiation (FPAR)
164 derived from the AVHRR satellite series (Pinzon et al, 2014; Los et al., 2000), burned area from
165 MODIS (Giglio et al, 2010), and meteorology (precipitation, temperature, and solar radiation)
166 from the Modern-Era Retrospective Analysis for Research and Applications (MERRA)
167 (Rienecker et al., 2011). CASA-GFED fluxes are generated at 0.5° x 0.5° resolution. For use in
168 the atmospheric transport model, monthly fluxes are downscaled to 3-hourly values using solar

169 radiation and temperature (Olsen and Randerson, 2004) along with MODIS 8-day satellite fire
170 detections (Giglio et al., 2006). In general, the biosphere is close to neutral in the CASA-GFED
171 simulation, i.e. there is no long-term net sink although there can be interannual variations in the
172 balance between uptake and release. In the version of CASA used here, a sink of ~100 Tg C y^{-1}
173 is induced by crop harvest in the U.S. Midwest that is prescribed based on National Agriculture
174 Statistics Service data on crop area and harvest. Although respiration of the harvested products
175 is neglected, the underestimate of emissions that is implied is geographically dispersed and in
176 principle correctable by the inversion.

177 For air-sea CO_2 exchange, monthly, climatological, measurement-based fluxes are taken
178 from Takahashi et al. (2009) for the reference year 2000 on a 4° x 5° lat/lon grid. In contrast to
179 the CASA-GFED flux being close to neutral on a global basis, the prior ocean flux forms a net
180 sink of 1.4 Pg C y^{-1}. ~~(Note that the uncertainties we assign to the prior fluxes, discussed below,~~
181 ~~are large enough to accommodate possible biases, e.g. the neutral biosphere rather than a sizable~~
182 ~~net land sink as suggested by the literature.)~~ For fossil CO_2, 1° x 1°, monthly- and interannually-
183 varying emissions are taken from the Carbon Dioxide Information Analysis Center (CDIAC)
184 inventory (Andres et al., 2012). This includes CO_2 from cement production but not international
185 shipping and aviation emissions. Oxidation of reduced carbon-containing gases from fossil fuels
186 in the atmosphere (~5% of the emissions; Nassar et al., 2010) is neglected, and the entire amount
187 of the emissions is released as CO_2 at the surface. Similarly, CO_2 from oxidation of biogenic and
188 biomass burning gases is neglected. ~~The total amount of CO_2 chemical production from fossil-~~
189 ~~fuel and biospheric gases~~ Together these oxidation sources ~~is~~ are estimated to be ~1 Pg C y^{-1} (for
190 year 2006; Nassar et al., 2010).

A priori flux uncertainties are derived from those assumed in the TC3 studies (Table 1), rescaled to our smaller regions and shorter periods with the same approach as Feng et al. (2009). ~~(Note that t~~The uncertainties ~~we assign to the prior fluxes, discussed below,~~ are large enough to accommodate possible biases, e.g. the neutral biosphere rather than a sizable net land sink as suggested by the literature.~~)~~ A priori spatial and temporal error correlations are neglected in our standard inversions. The neglect of a priori spatial error correlations is justified by the size of our flux optimization regions, with dimensions on the order of one thousand to several thousand km, likely greater than the error correlation lengths for our 2° × 2.5° grid-level fluxes. For example, Chevallier et al. (2012) estimated a correlation e-folding length of ~500 km for a grid size close to ours of 300 km × 300 km based on comparison of a terrestrial ecosystem model with global flux tower data.

2.2. Observations and uncertainties

For constraining fluxes at relatively high temporal resolution, observations are chosen that consist of discrete whole-air samples collected in glass flasks approximately weekly and continuous in situ tall tower measurements of CO_2 mole fraction from the NOAA ESRL Carbon Cycle Cooperative Global Air Sampling Network (Dlugokencky et al., 2013; Andrews et al., 2009) supplemented with continuous ground-based measurements at 3 sites in East Asia from the Japan Meteorological Agency (JMA) network (http://ds.data.jma.go.jp/gmd/wdcgg/cgi-bin/wdcgg/catalogue.cgi, accessed 14 Mar 2013; Tsutsumi et al., 2006). Both data sets are calibrated to the WMO-X2007 scale. In the present study, these data sets are referred to collectively as "in situ" observations. The 87 sites (Fig. 1a; Table S1) are chosen based on data

213 availability for the analysis period, Mar 2009-Sep 2010. Individual flask-air observations are
214 used in the inversions (with the average taken where there are multiple measurements at a
215 particular hour—up to two pairs of duplicate ~~samples~~flasks), and for the continuous
216 measurements, afternoon averages are used (between 1200 and 1700 local standard time),
217 avoiding the difficulty of simulating the effects of shallow nighttime boundary layers. For the
218 towers, data from the highest level only is used. We apply minimal filtering of the data. For the
219 NOAA data sets, we exclude only the flask samples or 30-second-average continuous data with
220 "rejection" flags, retaining data with "selection" flags (NOAA uses statistical filters and other
221 information such as wind direction to flag data that are likely valid but do not meet certain
222 criteria such as being representative of well-mixed, background conditions), since the reasonably
223 high-resolution transport model used here (Sect. 2.3) captures much of the variability in the
224 observations beyond background levels. Furthermore, observations strongly influenced by local
225 fluxes are typically assigned larger uncertainties by our scheme (described below), and therefore
226 have less weight in the inversion. For the JMA data, we omit only the hourly data with flag = 0,
227 meaning the number of samples is below a certain level, the standard deviation is high, and there
228 is a large discrepancy with one or both adjacent hourly values. Although some of the
229 observation sites used in our inversion are located close to each other, there is never any exact
230 overlap in grid box (altitude and/or longitude-latitude) or in time. Thus, all of those sites are
231 kept for the inversions, with observations at each site and day treated as independent (i.e.
232 neglecting error correlations).

233 We estimate the uncertainties for the flask-air observations as the root sum square (RSS)
234 of two ~~uncertainty~~ components: 1) the standard deviation of the observations from multiple

flasks within~~at a particular~~an hour or 0.3 ppm if there is only one sample, and 2) a simple estimate of the model transport/representation error. ~~For the first uncertainty component, we assign a value of 0.3 ppm if there is only one sample, and apply a minimum value of 0.01 ppm to avoid uncertainty values of 0.~~ The transport/representation error estimation is similar to that of the NOAA CarbonTracker (CT) CO_2 data assimilation system (prior to the CT 2015 version) (Peters et al., 2007; http://carbontracker.noaa.gov), whereby a fixed "model-data mismatch" is assigned based on the type of site, e.g. marine, coastal, continental, or polluted, ranging from 0.4 ~~ppm~~ to 4 ppm (Table S1). For the continuous measurements, we take the RSS of two uncertainty components: 1) the afternoon root mean square (RMS) of the uncertainties of the 30-second (NOAA) or hourly (JMA) ~~average~~ observations reported by the data providers, ~~(~~divided by the square root of the number of observations, N~~)~~, and 2) the standard error of all the 30-second/hourly mole fractions within an afternoon period. This represents an attempt to account for instrument error as well as transport/representation error. In addition, based on initial inversion results, we enlarged all in situ total observation uncertainties by a factor of 2 (mean site values in Table S1) to lower the normalized posterior cost function value (defined in Section 2.4) closer to 1 as appropriate for the chi-squared (χ^2) distribution (the final value of which is shown in Table 2). (Another test showed that further enlargement of the uncertainties to 3 times the original values, while lowering the cost function value further, does not substantially change the posterior fluxes overall.)

GOSAT measures reflected sunlight in a sun-synchronous orbit with a 3-day repeat cycle and a 10.5 km diameter footprint when in nadir mode (Yokota et al., 2009). The spacing between soundings is ~250 km along-track and ~160 km or ~260 km cross-track (for 5-point/3-

point sampling before/after Aug 2010). We use the ACOS B3.4 near infrared (NIR) retrieval of column-average CO_2 dry air mole fraction (XCO_2), with data from June 2009 onward (O'Dell et al., 2012; Osterman et al., 2013). Filtered and bias-corrected land nadir, including high (H) gain and medium (M) gain, and ocean glint data are provided. Three truth metrics were used together to correct biases (separately for H gain, M gain, and ocean glint) (Osterman et al., 2013; Lindqvist et al., 2015; Kulawik et al., 2016): 1) an ensemble of transport model simulations optimized against in situ observations, 2) coincident ground-based column observations from the Total Carbon Column Observing Network (TCCON), which are calibrated to aircraft in situ profiles linked to the WMO scale (Wunch et al., 2011), and 3) the assumption that CO_2 mole fraction ought to exhibit little spatiotemporal variability in the Southern Hemisphere mid-latitudes, other than a seasonal cycle and long-term trend. For our inversions, we use the average of all GOSAT observations falling within a given 2° latitude × 2.5° longitude transport model column in a given hour. Figure 1b shows the frequency of the ACOS GOSAT observations across the model grid.

The values assumed for the GOSAT uncertainties are based in part on the retrieval uncertainties provided with the ACOS data set. Following guidance from the data providers, these are inflated by a factor of 2 over land and 1.25 over ocean for more realistic estimates of the uncertainties (C. O'Dell, pers. comm., 2013); Kulawik et al. (2016) recommended an overall scale factor of 1.9 for the similar ACOS B3.5 data set. In the case of multiple observations within a model grid, we estimate the overall uncertainty as the RMS of the uncertainties of the individual observations, divided by the square root of N. Final uncertainty values are in the range of 0.31-3.20 ppm over land and 0.26-1.94 ppm over ocean, with corresponding means of

1.48 and 0.77 ppm. Error correlations between observations in different model grids and at different hours are neglected.

Inversions are conducted using different combinations of data, including the in situ data ("in situ-only"), the GOSAT data ("GOSAT-only"), and both ("in situ + GOSAT").

We use several additional data sets for independent evaluation of the inversion results. Aircraft measurements from the HIAPER Pole-to-Pole Observations (HIPPO) campaign consist of vertical profiles of climate-relevant gases and aerosols from the surface to as high as the lower stratosphere, spanning a wide range of latitudes mostly over the Pacific region (Wofsy et al., 2011). Five missions were conducted during different seasons in 2009-2011, with two of the missions overlapping with our analysis period. We use the "best available" CO_2 values derived from multiple measurement systems from the merged 10-second data product (Wofsy et al., 2012). Another data set, the 'Amazonica' aircraft measurements over the Amazon basin, is useful for evaluating inversion performance over tropical land. These measurements consist of profiles of several gases including CO_2 determined from flask samples from just above the forest canopy to 4.4 km altitude over 4 sites across the Brazilian Amazon starting in 2010, taken approximately biweekly (Gatti et al., 2014, 2016). Finally, the Japan-Russia Siberian Tall Tower Inland Observation Network (JR-STATION) of towers provides continuous in situ measurements of CO_2 and CH_4 over different ecosystem types across Siberia beginning in 2002 (Sasakawa et al., 2010; Sasakawa et al., 2013). The JR-STATION data have been used in combination with other in situ observations in CO_2 flux inversions (Saeki et al., 2013b; Kim et al., 2017).

301 2.3. Atmospheric transport model and model sampling

302 We use the Parameterized Chemistry and Transport Model (PCTM) (Kawa et al., 2004),
303 with meteorology from the NASA Global Modeling and Assimilation Office (GMAO) MERRA
304 reanalysis (Rienecker et al., 2011). For this analysis, PCTM was run at a resolution of 2° latitude
305 × 2.5° longitude and 56 hybrid terrain-following levels up to 0.4 hPa, and hourly temporal
306 resolution. A "pressure fixer" scheme has been implemented to ensure tracer mass conservation,
307 the lack of which can be a significant problem with assimilated winds (Kawa et al., 2004).
308 Evaluation of PCTM over the years has shown it to a reliable tool for carbon cycle studies. For
309 example, Kawa et al. (2004) showed that the SF_6 distribution from PCTM was consistent with
310 that of observations and of the models in TransCom 2, suggesting that the interhemispheric and
311 vertical transport were reasonable. PCTM performed well in boundary layer turbulent mixing
312 compared to most of the other models in a TransCom investigation of the CO_2 diurnal cycle
313 (Law et al., 2008). The TransCom-CH_4 intercomparison (Patra et al., 2011) showed that a more
314 recent version of PCTM performed very well relative to observations in its interhemispheric
315 gradients of SF_6, CH_3CCl_3, and CH_4 and interhemispheric exchange time, and follow-on studies
316 (Saito et al., 2013; Belikov et al., 2013) demonstrated through evaluation against observed CH_4
317 and ^{222}Rn that the convective vertical mixing in PCTM was satisfactory overall.

318 Offshore prior terrestrial biospheric and fossil fluxes are redistributed to the nearest
319 onshore grid cells in the model grid to counteract diffusion caused by our regridding the original
320 fluxes to the coarser 2° x 2.5° resolution, as recommended in the TC3 protocol (Gurney et al.,
321 2000).

The model is initialized with a concentration field appropriate for March 22, 2009 from a multi-year PCTM run with prior fluxes. The initial conditions are optimized in the inversions, as described in Sect. 2.4.

PCTM is sampled at grid cells containing in situ observation sites or GOSAT soundings, at the hours corresponding to the observations. To mimic the sampling protocol for coastal flask sites, which favors clean, onshore wind conditions, the model is sampled at the neighboring offshore grid cell if the cell containing the site is considered land according to a land/ocean mask. For in situ sites in general, an appropriate vertical level as well as horizontal location is selected. Specifically, the model CO_2 profile is interpolated to a level corresponding on average to the altitude above sea level of the observation site. This procedure is relevant primarily for mountain sites and tall towers as well as aircraft samples; the lowest model layer (with a thickness of ~100 m on average) was used for most other sites.

Model columns are weighted using ACOS column averaging kernels, as in the following (Eq. 15 from Connor et al., 2008):

$$\boldsymbol{X_{CO2}^{m}} = \boldsymbol{X_{CO2}^{a}} + \sum_{\mathrm{j}} \mathbf{h}_{\mathrm{j}} \mathbf{a}_{\mathbf{CO2},\mathrm{j}} (\mathbf{x}_{\boldsymbol{m}} - \mathbf{x}_{\boldsymbol{a}})_{\mathrm{j}}, \quad (1)$$

where $\boldsymbol{X_{CO2}^{m}}$ ($\boldsymbol{X_{CO2}^{a}}$) refers to the model (ACOS a priori) column average mole fraction, **h** is the pressure weighting function, $\mathbf{a_{CO2}}$ is the column averaging kernel, **x** refers to a CO_2 profile, and j is the level index.

Time series of model and observed mole fractions at selected flask and continuous sites spanning a range of latitudes, longitudes, elevations, and proximity to major fluxes are shown for

344 the prior and for the in situ-only inversion in Fig. 2. The prior model as well as the in situ
345 inversion captures much of the observed synoptic-scale variability. This suggests that the PCTM
346 transport is reasonably accurate, consistent with the findings of Parazoo et al. (2008) and Law et
347 al. (2008).
348
349 2.4. Inversion approach
350 The batch, Bayesian synthesis inversion approach optimizes in a single step the
351 agreement between model and observed CO_2 mole fractions and between a priori and a posteriori
352 flux estimates in a least-squares manner (e.g. Enting et al., 1995). As in the paper by Baker et al.
353 (2006), the cost function minimized in this approach can be expressed as
354
355 $$J = (\mathbf{c}_{\text{obs}} - \mathbf{c}_{\text{fwd}} - \mathbf{H}\mathbf{x})^T \mathbf{R}^{-1} (\mathbf{c}_{\text{obs}} - \mathbf{c}_{\text{fwd}} - \mathbf{H}\mathbf{x}) + (\mathbf{x}_0 - \mathbf{x})^T \mathbf{P}_0^{-1} (\mathbf{x}_0 - \mathbf{x}), \quad (2)$$
356
357 where $\mathbf{c}_{\text{obs}} - \mathbf{c}_{\text{fwd}}$ are mismatches between the observations and the mole fractions produced by
358 the prior fluxes, $\mathbf{H}$ is the Jacobian matrix relating model mole fractions at the observation
359 locations to regional flux adjustments $\mathbf{x}$ (note that $\mathbf{x}$ is used differently here than in Eq. 1), $\mathbf{R}$ is
360 the covariance matrix for the errors in $\mathbf{c}_{\text{obs}} - \mathbf{c}_{\text{fwd}}$, $\mathbf{x}_0$ is an a priori estimate of the flux
361 adjustments, and $\mathbf{P}_0$ is the covariance matrix for the errors in $\mathbf{x}_0$. The solution for the a posteriori
362 flux adjustments, $\hat{\mathbf{x}}$, is
363
364 $$\hat{\mathbf{x}} = (\mathbf{H}^T \mathbf{R}^{-1} \mathbf{H} + \mathbf{P}_0^{-1})^{-1} (\mathbf{H}^T \mathbf{R}^{-1} (\mathbf{c}_{\text{obs}} - \mathbf{c}_{\text{fwd}}) + \mathbf{P}_0^{-1} \mathbf{x}_0), \quad (3)$$
365

366 and the a posteriori error covariance matrix is given by

367

368 $$\mathbf{P} = (\mathbf{H}^T\mathbf{R}^{-1}\mathbf{H} + \mathbf{P}_0^{-1})^{-1}. \quad (4)$$

369

370 Importantly, the posterior uncertainties do not account for possible biases, given that the
371 Bayesian inversion framework adopted here, as in other CO_2 studies, assumes Gaussian error
372 distributions with no bias (observation, transport, prior, etc.).

373 This study focuses on the variability of natural fluxes (terrestrial NEP and ocean), and
374 thus considers adjustments to those fluxes only, assuming the prior estimates for the fossil and
375 fire fluxes are correct. This is commonly done in CO_2 inversion studies (e.g. Gurney et al., 2002;
376 Peters et al., 2007; Basu et al., 2013), with the rationale that the anthropogenic emissions are
377 relatively well known, at least at the coarse spatial scales of most global inversions. In our
378 inversion, flux adjustments are solved for at a resolution of 8 days and for each of 108 regions
379 that are modified from the 144 regions of the Feng et al. (2009) inversion (Fig. 1a), which are in
380 turn subdivided from the TC3 regions. (The choice of an 8-day flux interval is based on data
381 considerations, e.g. the quasi-weekly frequency of the flask measurements and reasonable
382 sampling by GOSAT.) This is a significantly higher resolution than the monthly intervals and
383 22/47 regions in the previous batch inversions of TC3/Butler et al. (2010), which allows us to
384 take advantage of the relatively high density of the GOSAT observations. One of our regions
385 consists of low-flux areas (e.g. Greenland, Antarctica) as well as small offshore areas that
386 contain non-zero terrestrial biospheric fluxes but do not fit into any of the TC3-based land
387 regions, similar to what was done by Feng et al. (2009). We also created a region that includes

388 areas with non-zero oceanic fluxes that do not fit into any of the TC3-based ocean regions
389 according to our gridding scheme.

390 Grid-scale spatial patterns are imposed in our flux adjustments based on the natural
391 fluxes, similar to TC3 and Butler et al. (2010), except that we use patterns specific to our prior
392 NEP or air-sea flux averaged over each particular 8-day period, rather than annual mean net
393 primary productivity (NPP) patterns over land and spatially constant patterns over the ocean. To
394 ensure net changes in flux are possible across each region, absolute values are used for the flux
395 patterns. Prior values of 0 are specified for all flux adjustments.

396 The initial conditions (i.c.) are also optimized at the same time as the fluxes via two
397 parameters: a scale factor to the i.c. tracer (described below) that allows for overall adjustment
398 of spatial gradients, and a globally uniform offset. A priori uncertainties of 0.01 for the scale
399 factor and 30 ppm for the offset are prescribed. Inversion results from March 22 through April
400 30, 2009 are discarded to avoid the influence of any inaccuracies in the i.c. (Our tests showed
401 that inferred fluxes after the first two months are insensitive to the treatment of i.c. For example,
402 for an in situ inversion in which we did not allow adjustments in the i.c. and offset parameters, 8-
403 day average flux results are very similar to those of the baseline inversion, especially after the
404 first two months, with a mean correlation coefficient of 0.95 from June 2009 onward across all
405 TC3 regions and a mean difference of 0.03 Pg C/yr.) Although the GOSAT data set begins in
406 June 2009, the observations can provide some constraint on earlier fluxes.

407 For generating the prior mole fractions, $\mathbf{c}_{fwd}$, and constructing the Jacobian matrix, $\mathbf{H}$,
408 transport model runs were performed for each of the prior flux types and an i.c. tracer, as well as
409 a run with a flux pulse (normalized to 1 Pg C y^{-1}) for each of the 108 regions and 71 8-day

periods. (The last period in 2009 is shortened to 5 days to fit cleanly within the year.) The i.c. tracer is initialized as described in Sect. 2.3 and transported without emissions or removals for the duration of the analysis period. Each flux pulse is transported for up to 13 months, after which the atmosphere is well mixed (within a range of 0.01 ppm). This procedure generated a massive amount of 3-D model output, ~30 terabytes (compressed). All of the model output was then sampled at the observation locations and times.

A singular value decomposition (SVD) approach is used instead of direct computation of Eq. 3 and Eq. 4 to obtain a stable inversion solution without any need for truncation of singular values below a certain threshold (Rayner et al., 1999). Use of the SVD technique is especially helpful in the case of the inversions using GOSAT data, since the Jacobian matrix is too large (92762 (102210) × 7674 for GOSAT (in situ + GOSAT)) to be successfully inverted on our system (with a single CPU).

3. Results

3.1. General evaluation of inversions, including short-term flux variability

Posterior model mole fractions are closer to the assimilated observations than are the prior mole fractions for the in situ-only, GOSAT-only, and in situ + GOSAT inversions, as desired, as suggested by Fig. 2 and indicated by the means and standard deviations of the model-observation differences over all observations shown in Fig. 3 (a, d, e, and f). Comparison of posterior mole fractions with the data set not used (Fig. 3b, c), on the other hand, gives mean differences not as close to 0 as in the comparison with the assimilated data (Fig. 3d and 3a,

respectively), and standard deviations that are larger than for the prior; this reflects the fact that the in situ and GOSAT data sets are not necessarily consistent with each other and combine to produce larger standard deviations than with the less variable prior model, which has not assimilated any data. The improved agreement between model and assimilated observations is reflected also in the cost function values before and after the inversions shown in Table 2. The minimized cost function follows a χ^2 distribution, and should thus have a value close to 1 (normalized by the number of observations) for a satisfactory inversion (Tarantola, 1987; Rayner et al., 1999). The posterior cost function values for all of the inversions are closer to 1 than the prior values.

In addition to cross-evaluating the in situ-only and GOSAT-only inversions, we evaluate both inversions against the independent, well-calibrated Amazon aircraft data set, which samples an under-observed region with large, variable fluxes. Vertical profiles of the model and the aircraft data (Fig. S1 in the supplementary material) show that the prior mole fractions often exhibit a bias relative to the aircraft observations, especially in a boundary layer-like structure below ~2 km altitude, with the sign of the average bias varying from season to season. The in situ inversion exhibits worse agreement with the observations than the prior does more often than it is better (e.g. with a root mean square error (RMSE) that is more than 1 ppm larger in 27 of 60 cases above 2 km and in 27 cases below 2 km, and more than 1 ppm smaller in only 12 cases above 2 km and 14 cases below 2 km). The GOSAT inversion exhibits smaller discrepancies with the observations than the in situ inversion does more often than the reverse, in both altitude ranges. Furthermore, the GOSAT inversion is more often better than the prior than worse above 2 km. Overall statistics, computed separately for lower and higher altitudes, are shown in Fig. 4.

454 The model-observation histograms indicate that agreement with the aircraft observations is again
455 better for the GOSAT inversion than the in situ inversion, with smaller or comparable mean
456 differences and standard deviations. There is a near complete lack of in situ sites in the inversion
457 that are sensitive to Amazon fluxes (as suggested by Fig. 1a), contrasting with the availability of
458 some GOSAT data over the region (Fig. 1b), meaning that regional flux adjustments in the in situ
459 inversion are driven, often erroneously, by correlations with fluxes outside of the region (as will
460 be discussed in depth below in Sect. 3.3). The GOSAT inversion agrees with the aircraft
461 observations better than the prior does above 2 km, implying that incorporating GOSAT data in
462 the inversion results in better performance than no data. However, the posterior model-
463 observation differences have greater variance than the prior below 2 km. A possible explanation
464 for this is that the use of GOSAT observations in an inversion introduces more random error in
465 the model mole fractions; given that the GOSAT data are sparse over the Amazon, there is little
466 data averaging over the 8-day intervals and flux regions and random errors can thus have a
467 substantial impact. GOSAT errors presumably affect higher altitudes in the model less, since the
468 mole fractions there are influenced by fluxes across a broader area than at lower altitudes and
469 thus errors are averaged out to a greater extent.

470 Example time series of 8-day mean prior and posterior NEP and ocean fluxes for the in
471 situ-only and GOSAT-only inversions are shown in Fig. 5. Since the posterior fluxes in our
472 inversion regions tend to have large fractional (percentage) uncertainties, especially for the in
473 situ-only inversion, we focus in this paper on results aggregated to larger regions. To facilitate
474 comparison with other studies, results are aggregated to TC3 land and ocean regions, accounting
475 for error correlations. The posterior time series exhibit larger fluctuations than the prior time

476 series, especially for the in situ inversion over land. The fluctuations would presumably be
477 smaller if we excluded flagged, outlier in situ observations or used a smoothed data product such
478 as GLOBALVIEW-CO_2 (2009), which has been used in many inversions including those of TC3
479 and some of those in the Houweling et al. (2015) intercomparison. In addition, some of the
480 fluctuations likely represent actual variability in the fluxes, while other fluctuations are probably
481 noise. In fact, the calculated numbers of degrees of freedom for signal and noise (as defined by
482 Rodgers, 2000) are 3525 and 4186 for the in situ inversion (summing up approximately to the
483 number of inversion parameters, 7674) and 4925 and 2947 for the GOSAT inversion. This
484 indicates that ~45% of the in situ inversion solution is based on actual information from the
485 measurements, given the assumed prior and observation uncertainties, while ~65% of the
486 GOSAT inversion solution is constrained by the measurements. The in situ data set is sparser
487 than GOSAT, especially over land, and thus contains greater spatial sampling bias, so that many
488 of the flux regions are under-determined and may exhibit so-called dipole behavior associated
489 with negative error correlations (discussed further below).
490 Results for the in situ + GOSAT inversion (not shown in Fig. 5) lie mostly in between the
491 in situ-only and GOSAT-only results. The fluxes generally lie closer to those of the GOSAT-
492 only inversion for regions with a relatively low density of in situ measurements, including
493 tropical and southern land regions, while they lie closer to those of the in situ-only inversion for
494 regions with a relatively high density of in situ measurements, including northern land and many
495 ocean regions. As expected, there are a larger number of degrees of freedom for signal, 6553,
496 than for either the in situ-only or the GOSAT-only inversion (and fewer degrees of freedom for

noise, 1632), indicating that the two data sets provide a certain amount of complementary information. Here, ~80% of the inversion solution is constrained by the measurements.

To average out noise in the posterior fluxes and to better observe the major features in the results, we show monthly average fluxes in Fig. 6. There is a similar onset of seasonal CO_2 drawdown in the GOSAT-only inversion and the CASA-GFED prior in Boreal North America, Temperate North America, and Boreal Asia, whereas the in situ-only inversion is noisier, similar to what was noted above. ~~The GOSAT inversion suggests an overall shift in the global CO_2 sink from tropical and southern land to northern land regions relative to the prior and the in situ inversion, similar to what has been found in previous GOSAT inversions (e.g. Houweling et al., 2015; discussed further below).~~ The GOSAT inversion exhibits systematic differences from the prior and the in situ inversion, together with ~~There are~~ some unusual features ~~in the GOSAT inversion~~. For example, there is a negative flux in January in some northern regions, with the 1σ range lying entirely below zero for Boreal Asia and Europe; this CO_2 uptake does not seem plausible in the middle of winter for these regions. Also, there are large positive fluxes during winter through spring in Northern Africa, which deviate from the prior beyond any overlap in the 1σ ranges for two months and whose 1σ ranges stay above zero for six months, summing up to a source of 1.9 Pg C over the period December through May, not including fires. The fluxes are larger than those of any sustained period of positive fluxes in any region in either the prior or the in situ inversion. The anomalous features suggest that the GOSAT inversion is affected by uncorrected retrieval biases that vary by season and region (as has been shown by Lindqvist et al. (2015) and Kulawik et al. (2016)) and/or sampling biases, including a lack of observations at

high latitudes during winter, which limit the ability to accurately resolve inferred fluxes down to the scale of TransCom regions.

~~A comparison of the monthly mean fluxes with those from another inversion system, NOAA's CarbonTracker version 2013B (CT2013B), is displayed in Fig. 7.~~ Results from our in situ-only inversion are shown alongside those of NOAA's CarbonTracker version 2013B inversion system (CT2013B) in Fig. 7 aggregated over large regions. CT2013B is an ensemble Kalman smoother data assimilation system with a window length of five weeks that uses multiple in situ observation networks and prior models to optimize weekly fluxes over 126 land "ecoregions" and 30 ocean regions (Peters et al., 2007; https://www.esrl.noaa.gov/gmd/ccgg/carbontracker/CT2013B/CT2013B_doc.php, accessed 4 October 2016). Similar to the present study, CT2013B uses CASA-GFED3 fluxes from van der Werf et al. (2010) as one of the land NEP priors, though with different FPAR and meteorological driver data. (CASA-GFED2 is the other land prior in its ensemble of priors.) In addition, CT2013B uses the seawater pCO_2 distribution from the Takahashi et al. (2009) climatology to compute fluxes for one of its ocean priors; the other ocean prior is based on results from an atmosphere-ocean inversion. CT2013B uses a similar number of ~~93~~ observation time series to that in the present study, 93 ~~while~~ vs. 87 ~~are used here, although the former include measurements by multiple labs at the same site and flask and continuous measurements at the same site (where duplicate observations are de-weighted by inflating the model-data mismatch error by the square root of N)~~. ~~A notable difference is that CT2013B solves for uniform flux scale factors over entire ecosystem types within each TC3 region, with the ecosystem types not necessarily being contiguous.~~ ~~Results from our in situ-only inversion are shown alongside those~~

~~of CT2013B in Fig. 7 aggregated over large regions.~~ In Fig. 7, ~~The~~ the two sets of posterior flux time series are similar overall, with overlapping 2σ ranges at all times except in the extratropical northern oceans region. One distinctive feature is that the posterior fluxes stay closer to the priors for CT2013B. A likely explanation is the tighter prior uncertainties in CT2013B, the magnitudes of which are on average 40% of ours for land regions and 30% of ours for ocean regions. For its ocean prior based on an atmosphere-ocean inversion, CT2013B assumes uncertainties consistent with the formal *posterior* uncertainties from the inversion, which are relatively small because of the large number of ocean observations used in the inversion; uniform fractional uncertainties are assumed for the other ocean prior and the land priors. Another feature is the larger month-to-month fluctuations in our results. In addition to the tighter prior uncertainties used, another factor that could contribute to smaller fluctuations in the CT2013B results is the use of prior estimates that represent a smoothing over three assimilation time steps, which attenuates variations in the forecast of the flux parameters in time. And another factor is that to dampen spurious noise due to the approximation of the covariance matrix by a limited ensemble, CT2013B applies localization for observation sites outside of the marine boundary layer, in which flux parameters that have a non-significant relationship with a particular observation are excluded. We further evaluate our inversions in the following sections.

3.2. Longer-term budgets and observation biases

Longer-timescale budgets can be assessed in Fig. 8, which displays 12-month mean fluxes (Jun 2009-May 2010) over large, aggregated regions, with fires now included, for our inversions and the CT2013B inversion. Results for individual TC3 regions are shown in Table 1.

The global total flux (including fossil emissions) is substantially more positive for the GOSAT-only inversion relative to the in situ-only inversion, 6.5 ± 0.2 Pg C y^{-1} vs. 4.1 ± 0.5 Pg C y^{-1}, while that for the in situ + GOSAT inversion lies in between at 5.7 ± 0.2 Pg C y^{-1}. Such a large difference in the atmospheric CO_2 growth rate implied by the two distinct data sets is plausible even if there are no trends in uncorrected biases between the data sets, given their sampling of different regions of the atmosphere (e.g. total column vs. surface only) and the relatively short 12-month time frame over which the growth occurs. (In addition, the GOSAT data may be affected by modest trends and interannual variability in biases, as reported by Kulawik et al. (2016).) In fact, for a different 12-month period within our analysis, Sep 2009-Aug 2010, the total fluxes for the GOSAT-only and in situ-only inversions are much closer to each other–5.53 Pg C y^{-1} and 5.47 Pg C y^{-1}. Houweling et al. (2015) also found a larger total flux in the GOSAT-only inversions relative to the in situ during Jun 2009-May 2010 averaged across 8 models, ~4.8 Pg C y^{-1} vs. ~4.6 Pg C y^{-1}, with a substantial amount of inter-model variability within those averages.

~~As was noted in Section 3.1, t~~The GOSAT-only inversion exhibits a shift in the global CO_2 sink from tropical and southern land to northern land relative to the prior and the in situ-only inversion (Fig. 8). The differences are within the 1σ uncertainty ranges. The shift includes ~~an~~ notable increases in the source in N. Africa ~~(0.2/1.5/2.0 Pg C y^{-1} for prior/in situ-only/GOSAT-only)~~, Temperate S. America ~~(0.4/0.4/1.1 Pg C y^{-1})~~, and Australia ~~(0.0/-0.2/0.6 Pg C y^{-1})~~, and ~~an~~ notable increases in the sink in Europe ~~(-0.1/0.6/-1.5 Pg C y^{-1})~~ and Temperate N. America ~~(-0.3/-0.6/-1.5 Pg C y^{-1})~~ (Table 1). As for the ocean, the GOSAT inversion also exhibits a larger source in the tropics relative to the prior and the in situ inversion (outside of the

584 1σ ranges; Fig. 8). However, the GOSAT inversion now exhibits a smaller sink over
585 extratropical northern oceans relative to the in situ inversion, and a larger sink over extratropical
586 southern oceans relative to both the prior and the in situ inversion (at or outside of the 1σ
587 ranges). The TC3 regions contributing the most to these differences include Tropical Indian
588 ~~(0.1/0.0/0.7 Pg C y^{-1} for prior/in situ-only/GOSAT-only)~~, N. Pacific ~~(-0.9/-0.5 Pg C y^{-1} for in~~
589 ~~situ-only/GOSAT-only)~~, N. Atlantic ~~(-0.8/-0.5 Pg C y^{-1} for in situ-only/GOSAT-only)~~, and
590 Southern Ocean ~~(-0.2/-0.4/-0.9 Pg C y^{-1} for prior/in situ-only/GOSAT-only)~~ (Table 1).
591 The GOSAT results appear to contradict global carbon cycle studies that favor a weaker
592 terrestrial net source in the tropics compensated by a weaker northern extratropical sink (e.g.
593 Stephens et al., 2007; Schimel et al., 2015). We show the north-south land carbon flux
594 partitioning of our results in Fig. S2 in the manner of Schimel et al. (2015). The shift in the sink
595 from the south + tropics to the north in the GOSAT inversion relative to the in situ inversion
596 goes in a direction opposite to that consistent with an airborne constraint considered by Stephens
597 et al. (2007) and with the expected effect of CO_2 fertilization according to Schimel et al. (2015).
598 However, the shift may be due at least in part to GOSAT retrieval and sampling biases. An
599 evaluation of posterior mole fractions in the GOSAT-only inversion against surface in situ
600 observations indicates that the GOSAT inversion may be biased low during much of the analysis
601 period over Europe and Temperate N. America, especially in winter (when there is little direct
602 constraint at high latitudes by GOSAT observations), and biased somewhat high over N. Africa,
603 especially in spring. However, the dearth of in situ sites over N. Africa, with only one in the
604 middle of the region (in Algeria) and a few around the edges (e.g. Canary Islands and Kenya),
605 precludes a definitive evaluation over that region. Globally, the GOSAT inversion tends to

underestimate mole fractions at high latitudes of the Northern Hemisphere, often by more than 1σ, as shown by latitudinal profiles averaged over all surface sites by season (Fig. 9), suggesting an overestimated northern sink. The same is true of the high latitudes of the Southern Hemisphere. The GOSAT inversion overestimates mole fractions in parts of the tropics, sometimes by more than 1σ (Fig. 9), suggesting an overestimated tropical source. Uncorrected retrieval biases may be especially prevalent in the tropics, where there are very few TCCON stations available as input to the GOSAT bias correction formulas; only 1 TCCON station, Darwin, Australia, was operating in the tropics during 2009-2010, and only 2 more stations, Reunion Island and Ascension Island, became operational during the rest of the ACOS B3.4 retrieval period. In contrast, the posterior mole fractions for the in situ-only inversion generally agree well with the surface observations (Fig. 9; also seen in the individual site time series in Fig. 2), which is expected given that these are the observations that are used in the optimization. The prior mole fractions are generally too high, which is consistent with the fact that the CASA-GFED biosphere is near neutral while the actual terrestrial biosphere is thought to generally be a net CO_2 sink.

Evaluation of the inversions against latitudinal profiles constructed from HIPPO aircraft measurements, which provide additional sampling over the Pacific (Fig. 10), does not indicate any widespread overestimate by the GOSAT inversion relative to the observations in the tropics ~~(Fig. 10a-f)~~, unlike what was seen in Fig. 9 for~~the~~ comparison with the more globally distributed surface observations. But the GOSAT inversion does exhibit an underestimate relative to HIPPO from ~40°S southward in the lower to middle levels of the troposphere (Fig. 10a, b, d, e), especially for Mission 2 (Oct-Nov 2009). Again, retrieval bias and sampling bias (a lack of

GOSAT ocean observations south of ~40°S and land observations south of ~50°S) are likely the causes of the underestimate. In the northern extratropics, the GOSAT inversion actually exhibits higher mean mixing ratios than HIPPO in general in the lower troposphere, especially for Mission 2, and the in situ inversion gives higher mixing ratios than HIPPO at some latitudes and lower mixing ratios at others for Mission 2. In one particular latitude range, 55-67°N, both inversions give much higher mixing ratios than HIPPO, by up to 67 ppm in the case of the in situ inversion and 30 ppm for the GOSAT inversion. This could reflect inaccuracy in posterior fluxes due to the inversions' being under-constrained over the high-latitude North Pacific and Alaska, with few observations during this season in the case of GOSAT and a tendency for the sparse in situ network to produce noisy inversion results, as was discussed above. However, given that the prior model also gives substantially higher mixing ratios than HIPPO at these latitudes (by up to 11 ppm), the discrepancy could be due in part to some factor common to the prior and posteriors such as model transport or representation error.

In the upper troposphere to lower stratosphere, the GOSAT inversion more often than not exhibits better agreement with the HIPPO observations than the in situ inversion does for both Mission 2 and 3 (Fig. 10c, f). (We think it is reasonable to include data from these altitudes as part of the evaluation of the inversion results, since the tropopause in the GEOS-5/MERRA meteorological data assimilation system underlying PCTM transport is considered to be accurate (Wargan et al., 2015) and PCTM has been shown to simulate upper troposphere-lower stratosphere trace gas gradients well compared to other models (Patra et al., 2011).) ~~A likely explanation is~~This may have to do with the fact that the GOSAT data provide constraints throughout the atmospheric column, whereas the in situ measurements constrain only surface

CO_2. ~~Figure 10 shows that the high-altitude mole fractions from the in situ inversion are consistently close to those of the prior, suggesting that the lack of high-altitude constraints prevents major adjustments in mole fractions at these levels, unlike in the GOSAT inversion.~~Given the lack of high-altitude constraints, the in situ inversion should not be expected to improve agreement with high-altitude aircraft observations relative to the prior, and, indeed, the inversion is no better than the prior (Fig. 10c, f). Note that the GOSAT data may not be driving the mole fraction adjustments locally in the region evaluated here, given the relative sparseness of GOSAT retrievals over the ocean, especially at high latitudes during the times of year of the HIPPO missions. Rather, the GOSAT data set provides large-scale atmospheric constraints that are transmitted to this region by transport. A possible explanation for the better agreement of the GOSAT inversion with HIPPO observations at these higher altitudes than at lower altitudes is that air parcels at higher altitudes generally consist of mixtures of air originating from broader areas near the surface (e.g. Orbe et al., 2013), so that regional posterior flux errors are more likely to cancel out (e.g. due to combining of negatively correlated errors from different regions), especially in the upper troposphere or above. ~~Regarding potential impacts of GOSAT biases, an air parcel at higher altitudes, especially in the upper troposphere or above, generally consists of a mixture of air originating from a broad area near the surface (e.g. Orbe et al., 2013), and thus the effects of different regional biases in posterior fluxes may cancel out at those altitudes.~~

The conclusion that GOSAT biases may contribute to the shift in the land sink is also supported by Houweling et al. (2015). That study reported a shift in the GOSAT-only inversions relative to the in situ inversions consisting of an increase in the sink in northern extratropical

672 land of 1.0 Pg C y^{-1} averaged across models and an increase in the source in tropical land of 1.2
673 Pg C y^{-1} during June 2009-May 2010; in comparison, our inversions produce an increase in the
674 northern land sink of 0.4 Pg C y^{-1} and an increase in the tropical land source of 1.2 Pg C y^{-1} (Fig.
675 8). Houweling et al. (2015) found an especially large and systematic shift in flux of ~0.8 Pg C y^{-1}
676 between N. Africa and Europe, but then provided evidence that the associated latitudinal
677 gradient in CO_2 mole fractions may be inconsistent with that based on surface and HIPPO
678 aircraft in situ observations. They also suggested that the shift in annual flux between the two
679 regions may be a consequence of sampling bias, with a lack of GOSAT observations at high
680 latitudes during winter. Chevallier et al. (2014) also found a large source in N. Africa of ~1 Pg C
681 y^{-1} in their ensemble of GOSAT inversions and considered the magnitude of that unrealistic,
682 given that emissions from fires in that region likely amount to < 0.7 Pg C y^{-1}. (Note that our N.
683 Africa source is even larger than that of Chevallier et al. (2014).) Inversion experiments by Feng
684 et al. (2016) provide evidence that the large European sink inferred from GOSAT observations
685 may be an artifact of high XCO_2 biases outside of the region that necessitate extra removal of
686 CO_2 from incoming air for mass balance, in concert with sub-ppm low XCO_2 biases inside the
687 region. An observing system simulation experiment by Liu et al. (2014) found that GOSAT
688 seasonal and diurnal sampling biases alone could result in an overestimated annual sink in
689 northern high-latitude land regions. And a review paper by Reuter et al. (2017) further
690 highlighted the discrepancy between satellite-based and ground-based estimates of European
691 CO_2 uptake and cited retrieval and sampling biases as possible sources of error in the former
692 (while also noting sampling issues with in situ networks for the region).

Again, the results for the in situ + GOSAT inversion lie mostly in between those for the in situ-only and GOSAT-only inversions, with the in situ + GOSAT fluxes lying closer to the GOSAT-only ones for the tropical/southern land regions and land as a whole (Table 1 and Fig. 8), suggesting the dominance of the GOSAT constraint in these regions. The posterior uncertainties for the GOSAT inversion (Table 1) are as small as or smaller than those for the in situ inversion, except in Boreal and Temperate N. America, N. Pacific, Northern Ocean, and Southern Ocean. This reflects the fact that GOSAT generally provides better spatial coverage, except over N. America, where the in situ network provides good coverage, and over and near high-latitude ocean areas, where there is decent in situ coverage and poor GOSAT coverage. Uncertainty reductions in the in situ inversion range from 15% to 93% for land regions and 15% to 56% for ocean regions (Table 1). In the GOSAT inversion, the uncertainty reductions range from 43% to 89% for land and 19% to 56% for ocean. And in the inversion with combined in situ and GOSAT data, the uncertainty reductions are larger than or equal to those in either the in situ-only or the GOSAT-only inversion, ranging from 61% to 96% for land and 40% to 67% for ocean.

3.3. Flux error correlations and land-ocean partitioning

Here we elaborate on posterior error correlations, which indicate the degree to which fluxes are estimated independently of one another. Negative correlations can be manifested in dipole behavior, in which unusually large flux adjustments of opposite signs occur in neighboring regions/time intervals. ~~These~~ Spatial error correlations are shown in Fig. 11 aggregated to TC3 regions and the 12-month period from June 2009 to May 2010. The full-rank

715 error covariance matrix generated by the exact Bayesian inversion method (from which the
716 correlation coefficients are derived) is a unique product of this study, particularly as applied to
717 satellite data. There are a larger number of sizable correlations between land regions in the in
718 situ inversion than in the GOSAT inversion (in the top left quadrant~~s~~ of the plot~~s~~). One specific
719 feature is negative correlations among the four TC3 regions in South America and Africa ("Trop
720 Am", "Temp S Am", "N Africa", and "S Africa") in the in situ inversion, whereas in the GOSAT
721 inversion there are negative correlations within South America and within Africa but not
722 between the two continents. Although there are less extensive correlations over land in the
723 GOSAT inversion, they are often of larger magnitude than in the in situ inversion; this could
724 reflect the fact that GOSAT observations, though of higher density than the in situ observations
725 over many regions, are column averages representing mixtures of air from a broader source
726 region than for surface observations, and may thus result in larger error correlations for
727 immediately adjacent regions, e.g. within a continent. Over the ocean regions, in contrast, the
728 GOSAT inversion exhibits anti-correlations that are as extensive as those for the in situ inversion
729 and often of larger magnitude. For example, there are substantial negative correlations between
730 Southern Ocean and each of the other southern regions—S. Pacific, S. Atlantic, and S. Indian.
731 This is consistent with the almost complete lack of GOSAT observations at the latitudes of the
732 Southern Ocean region and the southern edges of the neighboring ocean regions (Fig. 1b).
733 Interestingly, there is not a sizable correlation between N. Africa and Europe in the GOSAT
734 inversion (in either seasonal or 12-month means), which runs counter to what might be expected
735 from the shift in flux discussed above; rather, each of these regions is correlated with a number
736 of other regions. We do find a fairly large correlation of -0.62 between the northern extratropics

737 in aggregate (land + ocean) and the tropics for the 12-month period though. Correlations for the
738 in situ + GOSAT inversion (not shown) generally lie in between those of the in situ-only and
739 GOSAT-only inversions. Even with the incorporation of both sets of observations, there are
740 substantial correlations of as much as -0.6 between regions within a continent, reinforcing our
741 earlier conclusion that sampling gaps limit the ability of the observations to constrain fluxes
742 down to the scale of most TC3 regions.

743 The in situ-only and CT2013B posterior global totals are nearly the same, but the land-
744 ocean split is different, with our inversion exhibiting a larger sink over ocean than over land
745 (with non-overlapping 2σ ranges) while in CT2013B the land and ocean fluxes are similar, with
746 the ocean flux changing little from the prior (Fig. 8). A likely explanation for the difference is
747 the very tight prior constraints on ocean fluxes of CT2013B that were discussed above, which
748 force the flux adjustments to take place mostly on land. The GOSAT inversion also exhibits a
749 relatively large ocean sink of -3.1 ± 0.5 Pg C y^{-1}; for comparison, the CT2013B estimate is -2.4 ±
750 0.4 Pg C y^{-1}, our in situ-only estimate is -4.0 ± 0.8 Pg C y^{-1}, and the estimate of the Global
751 Carbon Project (GCP) is -2.5 ± 0.5 Pg C y^{-1} for 2009-2010 (Le Quéré et al., 2013; Le Quéré et
752 al., 2015). The GCP estimate is a synthesis that combines indirect observation-based estimates
753 for the mean over the 1990s with interannual variability from a set of ocean models and accounts
754 for additional observation-based estimates in the uncertainty. The difference between our
755 inversion estimates and the GCP estimate is actually even larger than suggested by those
756 numbers, given that a background river to ocean flux of ~0.5 Pg C y^{-1} should be subtracted from
757 our ocean flux to make it comparable to the GCP ocean sink, which refers to net uptake of
758 *anthropogenic* CO_2 (Le Quéré et al., 2015). Our relatively small land sink is reflected in our

759 inversion results' lying mostly outside of the GCP global land flux range in the north-south
760 partitioning plot in Fig. S2. Similarly, in comparing our results with those of Houweling et al.
761 (2015), we find that the global budgets are comparable for all three inversions—in situ-only,
762 GOSAT-only, and in situ + GOSAT—as was mentioned above, but the land-ocean split is
763 different. Our posterior ocean flux is -4.0 ± 0.8 Pg C y^{-1}, -3.1 ± 0.5 Pg C y^{-1}, and -3.9 ± 0.3 Pg C
764 y^{-1} for the three inversions, while it is -1.6 ± 0.5 Pg C y^{-1}, -1.2 ± 0.6 Pg C y^{-1}, and -1.5 ± 0.8 Pg C
765 y^{-1} in the results of Houweling et al. (2015; pers. comm., 2016) (averaged over different
766 weighted averages of the models).

767 There is a strong negative correlation globally between posterior flux errors for land and
768 ocean of -0.84 and -0.89 in the in situ-only and the GOSAT-only inversion, respectively. Basu et
769 al. (2013) also reported a large negative correlation between land and ocean fluxes of -0.97 in
770 their in situ + GOSAT inversion during September 2009-August 2010. The anti-correlations
771 imply that the observations cannot adequately distinguish between adjustments in the global land
772 and ocean sinks. Thus, land-ocean error correlation may be a fundamental challenge that global
773 CO_2 flux inversions are faced with, at least given the sampling characteristics of the in situ and
774 GOSAT data sets used here. Without tight prior constraints on ocean fluxes, those fluxes are
775 subject to large, and potentially unrealistic, adjustments (i.e. dipole behavior).

776 To assess the effect of prior constraints on the inversion, we conducted a test with
777 reduced prior uncertainties, for both land and ocean fluxes, so that they are similar on average to
778 those of CT2013B. Results for an in situ-only inversion and a GOSAT-only inversion are shown
779 in Table 1 and Fig. 12. For the in situ-only inversion, the posterior ocean flux is now much
780 smaller in magnitude, -2.8 ± 0.3 Pg C y^{-1}. The posterior ocean flux for the GOSAT inversion

781 does not change as much, decreasing in magnitude from the original -3.1 ± 0.5 Pg C y^{-1} to -2.9 ±
782 0.2 Pg C y^{-1}. The ocean flux 1σ ranges for both inversions now overlap with the 1σ range of
783 CT2013B; accounting for the riverine flux, the 1σ range for the in situ inversion overlaps with
784 the 1σ range of GCP, while the 1σ range for the GOSAT inversion is still just outside of that of
785 GCP. The better agreement with the GCP budget (land component) can also be seen in Fig. S2
786 for both inversions. The inversions with tighter priors have slightly larger cost function values
787 than the baseline inversions (Table 2; the difference for the GOSAT cases is concealed by
788 rounding). The inversions with tighter priors generally exhibit slightly better agreement with
789 independent observations, e.g. lower-altitude HIPPO observations (Fig. S3), and surface
790 observations in the case of the GOSAT inversion (Fig. S4), indicating that the effects of
791 sampling and retrieval biases are reduced with tighter prior uncertainties. The better agreement
792 also lends support to the smaller ocean sink estimates. (At high altitudes, keeping posterior mole
793 fractions closer to the prior mole fractions results in worse agreement with HIPPO in many
794 places, especially for the GOSAT inversion.) However, the tighter priors do not completely
795 eliminate the discrepancies between the inversions and the independent observations, suggesting
796 that tight priors may not completely counteract the effects of observational biases.
797 Basu et al. (2013) saw a similar underestimate of mole fractions during parts of the year
798 in the southern extratropics in their GOSAT inversion relative to surface observations and
799 overestimate of the seasonal cycle, though with some differences in the shape of the seasonal
800 cycle from our study (including a later descent toward and recovery from the annual minimum in
801 austral summer and a larger peak in late winter-early spring). They, however, used the SRON-
802 KIT RemoTeC GOSAT retrieval with a known issue over the ocean, and concluded that adding

803 global land and ocean observation bias correction terms to their inversion was needed to make
804 the land-ocean flux split more realistic and to improve the seasonal cycle of CO_2 in the southern
805 extratropics. In contrast, studies have found no noticeable bias in the ACOS B3.5 ocean glint
806 XCO_2 retrievals relative to TCCON (Kulawik et al., 2016) and a mean bias of only -0.06 ppm
807 relative to HIPPO (Frankenberg et al., 2016); the B3.4 version we use is on average ~0.2 ppm
808 lower than B3.5 in 2010 (Deng et al., 2016). So although a small overall negative bias in the
809 bias-corrected ACOS B3.4 ocean data cannot be ruled out (and there could of course be larger
810 negative biases on a regional scale, such as in the southern extratropics), we conclude that the
811 land-ocean flux split in inversions using either in situ or GOSAT data is strongly influenced by
812 error correlations and dependent on the prior uncertainties assumed.

813 The shift in the global terrestrial sink from the tropics/south to the north when comparing
814 the GOSAT-only inversion with the in situ-only inversion and the prior is still seen when prior
815 uncertainties are decreased (Fig. 12; Fig. S2), as is a substantially more positive global total
816 budget in the GOSAT inversion relative to the in situ (Fig. 12). The uncertainty reductions in the
817 test inversions are smaller than those in the baseline inversions (Table 1), as is expected from the
818 smaller starting values of the uncertainties. In summary, the magnitude of the ocean sink and the
819 partitioning of the global sink between land and ocean are sensitive to the prior uncertainties, but
820 other inferred features of the carbon budget are robust with respect to prior uncertainties.

821 Given that there is uncertainty in the land-ocean flux partitioning at sub-global scales as
822 well (e.g. as indicated by moderate negative correlations between northern land and northern
823 oceans, tropical land and tropical oceans, etc.), we consider results for combined land and ocean
824 regions in Figs. 8 and 12. They indicate that there is a shift in the global sink from the tropics to

825 the north and the south in the GOSAT inversion relative to the prior, and an increased source in
826 the tropics of ~2 Pg C y^{-1} in the GOSAT inversion relative to the in situ inversion. These
827 features are seen in the inversions with tighter priors as well as in the baseline inversions. Note
828 that the increased source over southern land and increased sink over southern oceans in the
829 GOSAT inversion relative to the in situ inversion that were discussed earlier cancel each other
830 out approximately, suggesting a compensation of errors. Also note that the inversion using the in
831 situ + GOSAT data sets, which provide more constraint than either of the data sets alone,
832 produces a global flux close to mid-way between the in situ-only and GOSAT-only inversions,
833 while it produces a Tropic Land + Oceans flux much closer to that of the GOSAT inversion than
834 to the in situ inversion. This suggests some degree of independence of the GOSAT-inferred
835 regional result from the global result.
836
837 3.4. Impacts of climatic conditions on 2009-2010 fluxes
838 We now analyze the impacts of several climatic events during the analysis period on CO_2
839 fluxes as indicated by the inversion results. We focus on 1) unusually hot and dry conditions at
840 Northern Hemisphere higher latitudes in summer of 2010, 2) wetter conditions over parts of
841 North America in spring and early summer of 2010 relative to 2009, and 3) record drought in the
842 Amazon in 2010.
843 Guerlet et al. (2013), who examined GOSAT data and performed a flux inversion using a
844 variational assimilation system, found that there was less net terrestrial CO_2 uptake in summer of
845 2010 than in 2009 at northern high latitudes, consistent with known severe heat waves, drought,

and high fire emissions, especially across Eurasia, centered around western Russia, and to a lesser extent in North America.

Motivated by that study, we examined our inversion results for 2009 and 2010, focusing on the GOSAT inversion. As can be seen in the global maps of natural plus biomass burning fluxes in June-July-August (JJA) in Fig. 13, the GOSAT inversion does appear to exhibit a decreased CO_2 uptake over Eurasia, including the area around western Russia (enclosed in a box in the figure), in 2010. A decreased sink can also be seen in parts of North America. A decreased sink over western Russia can also be seen in the CASA-GFED prior, though of a smaller magnitude. In contrast, there is actually an increased sink in that region in the in situ inversion. In fact, none of the sites used are in or immediately downwind of that region (Fig. 1a). Total NEP and fire fluxes over northern TC3 regions are shown in Fig. 14. There is less CO_2 uptake in JJA 2010 than in 2009 in all the regions except Temperate Asia in the GOSAT-only inversion. The differences exceed the 1σ ranges for 3 of the 5 regions, even exceeding the 3σ ranges for Europe, which includes western Russia. Also shown is the in situ + GOSAT inversion, which exhibits a similar pattern of 2010-2009 differences. These inversion results are thus consistent with the earlier GOSAT study. In contrast, the 2010-2009 differences in the prior are small and, for some regions, of the opposite sign as that in the inversions (Fig. 14).

Measurements from the JR-STATION tower network are suitably located for evaluating the inferred flux interannual variability over Eurasia. Time series are shown in Fig. 15 for observations, the prior model, and the GOSAT-only inversion at 6 sites with complete summertime data in 2009-2010. (As with the continuous measurements used in the in situ inversion, afternoon data are selected to avoid difficulties associated with nighttime boundary

868 layers.) Posterior mole fractions are noisier in the wintertime, likely a result of the lack of
869 GOSAT observations during that season at these high latitudes. Focusing on 2010-2009
870 differences, the observations suggest a shallower drawdown in 2010 than in 2009 at most of the
871 sites, which is generally captured by both the prior and the GOSAT posterior. It appears though
872 that the GOSAT inversion exaggerates the 2010-2009 difference at some of the sites,
873 overestimating especially the drawdown in 2009. For a more quantitative analysis, we calculate
874 the average 2010-2009 difference in mole fractions over June-July-August for each site (Table
875 3). The GOSAT-only inversion overestimates the 2010-2009 difference at 5 of the 6 sites. The
876 in situ + GOSAT inversion exhibits less of an overestimate overall than the GOSAT-only
877 inversion, with 3 of the 6 sites being substantially overestimated. The prior exhibits the best
878 agreement with the observations overall.

879 The earlier study by Guerlet et al. (2013) assumed that the differences between 2010 and
880 2009 posterior biospheric fluxes are relatively insensitive to biases in the GOSAT data, since at
881 least some of those errors may be similar between the two years. However, our evaluation of the
882 inversions using JR-STATION data suggests that retrieval biases can vary significantly from
883 year to year. Kulawik et al. (2016) estimated a year-to-year variability in GOSAT biases relative
884 to TCCON of 0.3 ppm averaged over the stations. Another study has raised a separate but
885 related issue of inversion results potentially being sensitive to the spatiotemporal distribution of
886 observations in different data sets (e.g. different GOSAT retrievals) (H. Takagi, pers. comm.,
887 2015); by extension, comparison of fluxes from two time periods can be affected by changes in
888 the distribution of observations over time within a particular data set. But in JJA 2009 and 2010,

889 there are similar numbers of ACOS GOSAT observations overall in the northern land region, so
890 differences in data coverage are probably not a factor in this particular case study.

891 Our evaluation using JR-STATION data also indicates that the prior may be a reasonable
892 estimate of the 2010-2009 difference in growing season fluxes, at least over Siberia, despite
893 possible shortcomings in the simulation of drought impacts on NEP and of the overall magnitude
894 of fire emissions by CASA-GFED3. The latest version of GFED (version 4s), which includes
895 small fires, tends to generate higher emissions than GFED3 (van der Werf et al., 2017).

896 Over large parts of North America, conditions were wetter in spring and early summer of
897 2010 than in 2009, especially in the western half of the U.S. and adjacent parts of Mexico and
898 Canada, as suggested by North American drought maps for June 2010 vs. June 2009 (e.g.
899 https://www.drought.gov/nadm/content/map/2010/06) and shallow groundwater status maps for
900 the U.S. based on GRACE (Gravity Recovery and Climate Experiment) satellite data for May-
901 June (Houborg et al., 2012; http://droughtcenter.unl.edu/NASA/GRACE/). Consistent with the
902 wetter conditions in 2010 are a larger CO_2 sink over North America (Boreal + Temperate) in
903 May-June 2010 relative to 2009 in our priors (-5.0 ± 3.9 Pg C y^{-1} vs. -3.4 ± 3.9 Pg C y^{-1}), in situ-
904 only posteriors (-5.0 ± 0.4 Pg C y^{-1} vs. -3.8 ± 0.5 Pg C y^{-1}), and GOSAT-only posteriors (-5.8 ±
905 0.4 Pg C y^{-1} vs. -3.3 ± 1.8 Pg C y^{-1}). We consider the in situ inversion result to be reliable here,
906 given the large uncertainty reduction for North America and small error correlations with other
907 regions (not shown). The 2010 and 2009 fluxes differ such that their 1σ ranges do not overlap
908 for the in situ and the GOSAT posteriors. Much warmer conditions in eastern North America in
909 May-June 2010 compared to 2009 (e.g. https://www.ncdc.noaa.gov/sotc/global/201005 and
910 https://www.ncdc.noaa.gov/sotc/global/200905) may have also contributed to increased uptake,

911 especially at higher latitudes, where insufficient warmth can be more of a limiting factor for NEP
912 than insufficient moisture during late spring-early summer. Despite the increased sink in June
913 2010 over North America, the 2010 summer exhibits a decreased sink relative to 2009 when
914 integrated through JJA (Fig. 14).

915 The Amazon basin experienced a record drought in 2010, which led to decreased
916 vegetation greenness and a net carbon loss to the atmosphere (Xu et al., 2011; Gatti et al., 2014).
917 Dry conditions in the north and center of the basin in the first three months were caused by the El
918 Niño of late 2009-early 2010, and an enhanced and prolonged dry season in the southern areas of
919 the basin was connected to an Atlantic sea surface temperature anomaly during the second half
920 of the year (Gatti et al., 2014). According to our prior estimate, fire emissions minus NEP
921 represented a near-zero net flux of -0.1 ± 2.1 Pg C y^{-1} in Jul-Sep 2010 (a period that includes
922 peak drought conditions and fire counts of that year) and a sink of -1.9 ± 2.1 Pg C y^{-1} in Jul-Sep
923 2009 in the TC3 Tropical America region. (The fire emissions amounted to 2.0 Pg C y^{-1} and 0.2
924 Pg C y^{-1} in Jul-Sep 2010 and 2009, respectively, while NEP was 2.1 Pg C y^{-1} in both periods.)
925 However, our GOSAT inversion suggests the reverse, -0.9 ± 0.6 Pg C y^{-1} vs. -0.4 ± 0.3 Pg C y^{-1}
926 for Jul-Sep 2010 and 2009, respectively. (We do not report the analogous results for the in situ
927 inversion, since the uncertainties are large in this undersampled region.) The prior estimate
928 seems more consistent with the expected impact of drought on fluxes than the inversion estimate
929 does. The inversion is hampered in the region by the relatively small number of GOSAT
930 soundings that are retrieved and pass the quality filters, especially during the burning season
931 (with substantial light scattering by aerosols) and the rainy season (with extensive cloud cover).
932 The dearth of observations results in relatively large posterior uncertainties and/or sizable flux

933 error correlations. Furthermore, there is differing data coverage, with 2010 having fewer
934 observations than 2009 in the TC3 Tropical America region during the height of the fire season
935 (85 and 20 in Aug and Sep 2010 vs. 101 and 33 in 2009) and more observations than 2009 in
936 July (150 vs. 85). The differing data coverage itself could affect the flux estimates differently in
937 2009 and 2010. The Amazonica data set does not enable an evaluation of the flux estimates for
938 both 2009 and 2010, since the data set begins in 2010. However, comparison of the prior and
939 GOSAT model mole fractions in 2010 with the Amazonica data shows that biases for both can
940 vary substantially over time, e.g. in July vs. Aug-Sep (Fig. S1). This raises the possibility that
941 neither the prior nor the GOSAT inversion correctly estimates the interannual flux difference in
942 this region and also supports the idea that inversion bias can vary with data coverage.
943
944
945 **4. Discussion and conclusions**
946 We have successfully applied a global, high-resolution, batch Bayesian CO_2 inversion
947 method to surface in situ observations and passive satellite column measurements from GOSAT
948 and compared the flux estimates with ones using Kalman filter and variational approaches that
949 involve various approximations. The exact inversion method provides full posterior error
950 covariances, which allows us to quantitatively evaluate the degree to which regional fluxes are
951 constrained independently of one another. However, for inversions over longer periods, using
952 larger volumes of data such as from OCO-2, or at higher flux resolution, more computationally
953 efficient methods are essential.

954 The GOSAT inversion is generally better constrained than the in situ inversion, with
955 smaller posterior regional flux uncertainties and correlations, except in places like North
956 America and northern and southern high-latitude ocean where the in situ observation networks
957 used provide relatively good coverage. Note that our in situ inversion did not make use of all the
958 surface monitoring sites that operated during the analysis period, omitting for example a number
959 of sites operated exclusively by agencies in Canada, Australia, and Europe
960 (http://ds.data.jma.go.jp/gmd/wdcgg/cgi-bin/wdcgg/catalogue.cgi), and that the surface networks
961 have been enhanced with additional sites since then. Furthermore, the in situ data sets that we
962 used for evaluation of the inversions, including JR-STATION and Amazonica, could also be
963 used as input in the inversions. And yet other aircraft data sets such as CONTRAIL, which
964 samples large parts of the Pacific and some other areas (Niwa et al., 2012), and NOAA's regular
965 aircraft profiles over mostly North America
966 (https://www.esrl.noaa.gov/gmd/ccgg/aircraft/index.html) and column measurements such as
967 from TCCON could be added. The use of GOSAT data in combination with in situ data provides
968 even greater flux uncertainty reductions than the use of either data set alone, indicative of
969 complementary constraints in the two datasets. Nevertheless, remaining coverage gaps,
970 including a lack of GOSAT observations at high latitudes during winter over land and year-round
971 over the ocean, and spatially, seasonally, and interannually varying coverage over tropical land,
972 limit the ability to accurately resolve fluxes down to the scale of TransCom sub-continental/sub-
973 ocean basin regions.

974 Our GOSAT inversion suggests ~~a shift in the global terrestrial CO_2 sink from the tropics~~
975 ~~and south to the north, relative to the prior and the in situ inversion;~~, for combined land and

ocean fluxes, ~~the GOSAT inversion produces~~ a shift in the global sink from the tropics to the north and the south relative to the prior, and an increased source in the tropics of ~2 Pg C y^{-1} relative to the in situ inversion. Similar shifts are seen in studies using other inversion approaches, such as the inversion intercomparison of Houweling et al. (2015). This result may be driven at least in part by sampling and uncorrected retrieval biases in the ACOS GOSAT data set, as suggested by sizable discrepancies between posterior mole fractions in the GOSAT-only inversion and surface in situ and lower-tropospheric HIPPO aircraft observations. While the shift in the global sink appears to be a robust feature of the inversions, the partitioning of the sink between land and ocean in the inversions using either in situ or GOSAT data is found to be sensitive to prior uncertainties because of negative correlations in the flux errors for the two domains. The loose prior uncertainties assumed in our baseline inversions may explain the larger ocean sink estimates compared to other studies, including CT2013B and the Houweling et al. (2015) intercomparison. A rationale for specifying loose prior uncertainties is that this allows the results to be driven more by the observations than by the prior estimates. However, in light of increasing confidence in estimates of the global ocean sink (e.g. from GCP), it may be more appropriate to start with a reliable set of ocean fluxes and apply tighter prior uncertainties similar to those from our sensitivity test. In any case, more weight should be given to combined land and ocean fluxes across latitudinal bands than to separate land and ocean flux estimates for the current observational configurations.

The GOSAT inversion indicates significantly less CO_2 uptake in summer of 2010 than in 2009 in the north, consistent with a previous GOSAT analysis and likely reflecting severe heat waves and drought especially across Eurasia. However, observations from the JR-STATION in

998 situ network suggest that the GOSAT inversion (and to a lesser extent, the in situ + GOSAT
999 inversion) exaggerates the 2010-2009 difference in uptake in Siberia, while the CASA-GFED
1000 prior reasonably estimates that quantity. Thus, it may not be accurate to assume that year-to-year
1001 posterior flux differences are insensitive to satellite retrieval biases, as was done in the other
1002 study. The prior, in situ posterior, and GOSAT posterior all indicate greater CO_2 uptake over
1003 North America in spring to early summer of 2010 than in 2009, consistent with wetter conditions
1004 over large parts of the continent. Decreased net uptake in July-September of 2010 relative to
1005 2009 in our prior appears to be consistent with record drought in the Amazon in 2010, while the
1006 GOSAT inversion shows the reverse. However, time-varying biases in both the prior model and
1007 the GOSAT inversion relative to Amazon aircraft profiles raise the possibility that neither one
1008 correctly estimates the interannual flux difference in this region and also support the idea that
1009 inversion bias can vary with data coverage. Overall, the results do demonstrate that climatic
1010 conditions can drive significant year-to-year variability in natural carbon fluxes on regional
1011 scales.

1012 Gaps in coverage at higher latitudes, especially in winter, as well as limited sampling
1013 over tropical land are a fundamental limitation of passive satellite measurements (including
1014 OCO-2) and imply an important future role for active satellites such as NASA's proposed Active
1015 Sensing of CO_2 Emissions over Nights, Days, and Seasons (ASCENDS) mission (Kawa et al.,
1016 2010; ASCENDS Ad Hoc Science Definition Team, 2015). Ongoing development of thermal IR
1017 (TIR) CO_2 retrievals for GOSAT and the future GOSAT-2 with sensitivity to several layers from
1018 the lower troposphere to the lower stratosphere shows promise for producing sufficiently
1019 accurate data that could also help to fill NIR retrieval coverage gaps (Saitoh et al., 2017a; b).

Additional in situ and TCCON measurements in regions that are under-observed and challenging for forward model simulations, especially Africa, would also be valuable for improving bias corrections for satellite retrievals and evaluating flux inversions using satellite data.

Competing interests

The authors declare that they have no conflict of interest.

Acknowledgments

This work has been supported by the NASA Atmospheric CO_2 Observations from Space program element and the NASA Carbon Monitoring System Program. The NASA Goddard High-End Computing Program has provided access to and assistance with supercomputing resources at the NASA Center for Climate Simulation. The ACOS GOSAT data were produced by the ACOS/OCO-2 project at the Jet Propulsion Laboratory, California Institute of Technology using spectra acquired by the GOSAT Project. We thank Chris O'Dell for providing the ACOS data to us, John Miller and Manuel Gloor for their partnership in producing the Amazonica data (with support from NERC, FAPESP, ERC, NASA, CNPQ, NOAA, IPEN, and U. of Leeds for the Amazon Greenhouse measurement program led by L. Gatti), NOAA ESRL GMD CCGG for making their flask and continuous tower data publicly available, JMA (including Yukio Fukuyama and Atsushi Takizawa) for making their in situ data publicly available on the WDCGG website and providing assistance, and Steven Wofsy for making HIPPO data available. CT2013B results are provided by NOAA ESRL, Boulder, Colorado, USA from the website at

1042 http://carbontracker.noaa.gov. Many thanks go to Martha Butler for providing inversion code
1043 and documentation. We also thank Zhengxin Zhu for contributing to data processing, Liang
1044 Feng and Paul Palmer for their inversion region map, David Baker for advice on inversions,
1045 Sander Houweling for providing results from his intercomparison paper and for helpful
1046 discussion, Lesley Ott for help with using ACOS data files and for discussions, Chris O'Dell, Ed
1047 Dlugokencky, and especially Arlyn Andrews for comments on the manuscript, and Sourish Basu
1048 for discussions.
1049

References

Andres, R. J., Boden, T. A., and Marland, G.: Monthly Fossil-Fuel CO_2 Emissions: Mass of Emissions Gridded by One Degree Latitude by One Degree Longitude, Carbon Dioxide Information Analysis Center, Oak Ridge National Laboratory, U.S. Department of Energy, Oak Ridge, Tenn., U.S.A., doi:10.3334/CDIAC/ffe.MonthlyMass.2012, 2012.

Andrews, A. E., Kofler, J., Bakwin, P. S., Zhao, C., and Tans, P.: Carbon Dioxide and Carbon Monoxide Dry Air Mole Fractions from the NOAA ESRL Tall Tower Network, 1992-2009, Version: 2011-08-31, Path: ftp://aftp.cmdl.noaa.gov/data/trace_gases/co2/in-situ/tower/, 2009.

ASCENDS Ad Hoc Science Definition Team: Active Sensing of CO_2 Emissions over Nights, Days, and Seasons (ASCENDS) Mission Science Mission Definition Study (draft), https://cce.nasa.gov/ascends_2015/ASCENDS_FinalDraft_4_27_15.pdf, 2015.

Baker, D. F., Law, R. M., Gurney, K. R., Rayner, P., Peylin, P. and co-authors: TransCom 3 inversion intercomparison: Impact of transport model errors on the interannual variability of regional CO_2 fluxes, 1988–2003, Global Biogeochem. Cycles, 20, GB1002, doi:10.1029/2004GB002439, 2006.

Baldocchi, D., et al.: FLUXNET: A new tool to study the temporal and spatial variability of ecosystem–scale carbon dioxide, water vapor, and energy flux densities, Bull. Am. Meteorol. Soc., 82, 2415–2434, 2001.

Basu, S., Guerlet, S., Butz, A., Houweling, S., Hasekamp, O., Aben, I., Krummel, P., Steele, P., Langenfelds, R., Torn, M., Biraud, S., Stephens, B., Andrews, A., and Worthy, D.: Global

1071 CO_2 fluxes estimated from GOSAT retrievals of total column CO_2, Atmos. Chem. Phys., 13,
1072 8695–8717, doi:10.5194/acp-13-8695-2013, 2013.
1073 Belikov, D. A., Maksyutov, S., Krol, M., Fraser, A., Rigby, M., Bian, H. S., Agusti-Panareda, A.,
1074 Bergmann, D., Bousquet, P., Cameron-Smith, P., Chipperfield, M. P., Fortems-Cheiney, A.,
1075 Gloor, E., Haynes, K., Hess, P., Houweling, S., Kawa, S. R., Law, R. M., Loh, Z., Meng, L.,
1076 Palmer, P. I., Patra, P. K., Prinn, R. G., Saito, R., and Wilson, C.: Off-line algorithm for
1077 calculation of vertical tracer transport in the troposphere due to deep convection, Atmos.
1078 Chem. Phys., 13, 1093-1114, doi:10.5194/acp-13-1093-2013, 2013.
1079 Butler, M. P., Davis, K. J., Denning, A. S., and Kawa, S. R.: Using continental observations in
1080 global atmospheric inversions of CO_2: North American carbon sources and sinks, Tellus,
1081 62B, 550–572, doi:10.1111/j.1600-0889.2010.00501.x, 2010.
1082 Chatterjee, A. and Michalak, A. M.: Technical Note: Comparison of ensemble Kalman filter and
1083 variational approaches for CO_2 data assimilation, Atmos. Chem. Phys., 13, 11643–11660,
1084 doi:10.5194/acp-13-11643-2013, 2013.
1085 Chevallier, F., et al.: What eddy-covariance measurements tell us about prior land flux errors in
1086 CO_2-flux inversion schemes, Global Biogeochem. Cycles, 26, GB1021,
1087 doi:10.1029/2010GB003974, 2012.
1088 Chevallier, F., Palmer, P. I., Feng, L., Boesch, H., O'Dell, C. W., and Bousquet, P.: Toward
1089 robust and consistent regional CO_2 flux estimates from in situ and spaceborne measurements
1090 of atmospheric CO_2, Geophys. Res. Lett., 41, 1065–1070, doi:10.1002/2013GL058772,
1091 2014.

1092 Ciais, P., Rayner, P., Chevallier, F., Bousquet, P., Logan, M., Peylin, P., and Ramonet, M.:
1093 Atmospheric inversions for estimating CO_2 fluxes: methods and perspectives, Climatic
1094 Change, 103:69–92, DOI 10.1007/s10584-010-9909-3, 2010.
1095 Connor, B. J., Bösch, H., Toon, G., Sen, B., Miller, C., and Crisp, D.: Orbiting Carbon
1096 Observatory: Inverse method and prospective error analysis, J. Geophys. Res., 113, A05305,
1097 doi:10.1029/2006JD008336, 2008.
1098 Crisp, D.: Measuring atmospheric carbon dioxide from space with the Orbiting Carbon
1099 Observatory-2 (OCO-2), Proc. SPIE 9607, Earth Observing Systems XX, 960702,
1100 doi:10.1117/12.2187291, 2015.
1101 Deng, F., Jones, D. B. A., Henze, D. K., Bousserez, N., Bowman, K. W., Fisher, J. B., Nassar,
1102 R., O'Dell, C., Wunch, D., Wennberg, P. O., Kort, E. A., Wofsy, S. C., Blumenstock, T.,
1103 Deutscher, N. M., Griffith, D. W. T., Hase, F., Heikkinen, P., Sherlock, V., Strong, K.,
1104 Sussmann, R., and Warneke, T.: Inferring regional sources and sinks of atmospheric CO_2
1105 from GOSAT XCO_2 data, Atmos. Chem. Phys., 14, 3703–3727, doi:10.5194/acp-14-3703-
1106 2014, 2014.
1107 Deng, F., Jones, D. B. A., O'Dell, C. W., Nassar, R., and Parazoo, N. C.: Combining GOSAT
1108 XCO_2 observations over land and ocean to improve regional CO_2 flux estimates, J. Geophys.
1109 Res. Atmos., 121, 1896–1913, doi:10.1002/2015JD024157, 2016.
1110 Dlugokencky, E. J., Lang, P. M., Masarie, K. A., Crotwell, A. M., and Crotwell, M. J.:
1111 Atmospheric Carbon Dioxide Dry Air Mole Fractions from the NOAA ESRL Carbon Cycle
1112 Cooperative Global Air Sampling Network, 1968-2012, Version: 2013-08-28, available at:

1113 ftp://aftp.cmdl.noaa.gov/data/trace_gases/co2/flask/surface/ (last access: 18 February 2014),
1114 2013.
1115 Eldering, A., Wennberg, P. O., Crisp, D., Schimel, D. S., Gunson, M. R., Chatterjee, A., Liu, J.,
1116 Schwandner, F. M., Sun, Y., O'Dell, C. W., Frankenberg, C., Taylor, T., Fisher, B.,
1117 Osterman, G. B., Wunch, D., Hakkarainen, J., Tamminen, J., and Weir, B.: The Orbiting
1118 Carbon Observatory-2 early science investigations of regional carbon dioxide fluxes,
1119 Science, 358, eaam5745, doi:10.1126/science.aam5745, 2017.
1120 Engelen, R. J., Denning, A. S., and Gurney, K. R.: On error estimation in atmospheric CO_2
1121 inversions, J. Geophys. Res., 107, 4635, doi:10.1029/2002JD002195, 2002.
1122 Enting, I. G. and Mansbridge, J. V.: Seasonal sources and sinks of atmospheric CO_2: Direct
1123 inversion of filtered data, Tellus, 41B, 111-126, 1989.
1124 Enting, I. G., Trudinger, C. M., and Francey, R. J.: A synthesis inversion of the concentration
1125 and $\delta^{13}C$ of atmospheric CO_2, Tellus, 47B, 35–52, 1995.
1126 Feng, L., Palmer, P. I., Boesch, H., and Dance, S.: Estimating surface CO_2 fluxes from space-
1127 borne CO_2 dry air mole fraction observations using an ensemble Kalman Filter, Atmos.
1128 Chem. Phys., 9, 2619–2633, doi:10.5194/acp-9-2619-2009, 2009.
1129 Feng, L., Palmer, P. I., Parker, R. J., Deutscher, N. M., Feist, D. G., Kivi, R., Morino, I., and
1130 Sussmann, R.: Estimates of European uptake of CO_2 inferred from GOSAT X_{CO2} retrievals:
1131 sensitivity to measurement bias inside and outside Europe, Atmos. Chem. Phys., 16, 1289–
1132 1302, doi:10.5194/acp-16-1289-2016, 2016.
1133 Frankenberg, C., Kulawik, S. S., Wofsy, S., Chevallier, F., Daube, B., Kort, E. A., O'Dell, C.,
1134 Olsen, E. T., and Osterman, G.: Using airborne HIAPER Pole-to-Pole Observations (HIPPO)

to evaluate model and remote sensing estimates of atmospheric carbon dioxide, Atmos. Chem. Phys., 16, doi:10.5194/acp-2015-961, 2016.

Gatti, L. V., Gloor, M., Miller, J. B., Doughty, C. E., Malhi, Y., Domingues, L. G., Basso, L. S., Martinewski, A., Correia, C. S. C., Borges, V. F., Freitas, S., Braz, R., Anderson, L. O., Rocha, H., Grace, J., Phillips, O., and Lloyd, J.: Drought sensitivity of Amazonian carbon balance revealed by atmospheric measurements, Nature, 506, 76-80, doi:10.1038/nature12957, 2014.

Gatti , L., Gloor, E., and Miller, J.: Greenhouse gas profile measurements (CO, CO_2, CH_4) above the forest canopy at four sites for the Amazonica project. NCAS British Atmospheric Data Centre, accessed 5 Dec 2016. http://catalogue.ceda.ac.uk/uuid/7201536a8b7a1a96de584e9b746acee3, 2016.

Giglio, L., Csiszar, I., and Justice, C. O.: Global distribution and seasonality of active fires as observed with the Terra and Aqua Moderate Resolution Imaging Spectroradiometer (MODIS) sensors, J. Geophys. Res., 111, G02016, doi:10.1029/2005JG000142, 2006.

Giglio, L., Randerson, J. T., van der Werf, G. R., Kasibhatla, P. S., Collatz, G. J., Morton, D. C., and DeFries, R. S.: Assessing variability and long-term trends in burned area by merging multiple satellite fire products, Biogeosciences, 7, 1171–1186, doi:10.5194/bg-7-1171-2010, 2010.

GLOBALVIEW-CO_2: Cooperative Atmospheric Data Integration Project-Carbon Dioxide, CD-ROM, NOAA-ESRL, Boulder, Colo. [Also available on Internet via anonymous FTP to ftp.cmdl.noaa.gov,Path:ccg/co2/ GLOBALVIEW], 2009.

1156 Gourdji, S. M., Mueller, K. L., Yadav, V., Huntzinger, D. N., Andrews, A. E., Trudeau, M.,
1157 Petron, G., Nehrkorn, T., Eluszkiewicz, J., Henderson, J., Wen, D., Lin, J., Fischer, M.,
1158 Sweeney, C., and Michalak, A. M.: North American CO_2 exchange: intercomparison of
1159 modeled estimates with results from a fine-scale atmospheric inversion, Biogeosciences, 9,
1160 457–475, 2012.
1161 Guerlet, S., Basu, S., Butz, A., Krol, M., Hahne, P., Houweling, S., Hasekamp, O. P., and Aben,
1162 I.: Reduced carbon uptake during the 2010 Northern Hemisphere summer from GOSAT,
1163 Geophys. Res. Lett., 40, 2378–2383, doi:10.1002/grl.50402, 2013.
1164 Gurney, K., Law, R., Rayner, P., and Denning, A. S.: TransCom 3 Experimental Protocol,
1165 Department of Atmospheric Science, Colorado State University, USA, Paper 707 (Available
1166 at http://transcom.colostate.edu/TransCom_3/transcom_3.html), 2000.
1167 Gurney, K. R., et al.: Towards robust regional estimates of CO_2 sources and sinks using
1168 atmospheric transport models, Nature, 415, 626–630, 2002.
1169 Hayes, D. J., Turner, D. P., Stinson, G., McGuire, A. D., Wei, Y., West, T. O., Heath, L. S.,
1170 deJong, B., McConkey, B. G., Birdsey, R. A., Kurz, W. A., Jacobson, A. R., Huntzinger, D.
1171 N., Pan, Y., Post, W. M., and Cook, R. B.: Reconciling estimates of the contemporary North
1172 American carbon balance among terrestrial biosphere models, atmospheric inversions, and a
1173 new approach for estimating net ecosystem exchange from inventory-based data, Global
1174 Change Biology, doi: 10.1111/j.1365-2486.2011.02627.x, 2012.
1175 Houborg, R., Rodell, M., Li, B., Reichle, R., and Zaitchik, B.: Drought indicators based on
1176 model assimilated GRACE terrestrial water storage observations, Wat. Resour. Res, 48,
1177 W07525, doi:10.1029/2011WR011291, 2012.

1178 Houweling, S., Baker, D., Basu, S., Boesch, H., Butz, A., Chevallier, F., Deng, F., Dlugokencky,
1179 E. J., Feng, L., Ganshin, A., Hasekamp, O., Jones, D., Maksyutov, S., Marshall, J., Oda, T.,
1180 O'Dell, C. W., Oshchepkov, S., Palmer, P. I., Peylin, P., Poussi, Z., Reum, F., Takagi, H.,
1181 Yoshida, Y., and Zhuravlev, R.: An intercomparison of inverse models for estimating sources
1182 and sinks of CO_2 using GOSAT measurements, J. Geophys. Res. Atmos., 120, 5253–5266,
1183 doi:10.1002/2014JD022962, 2015.
1184 Kaminski, T., Rayner, P. J., Heimann, M., and Enting, I. G.: On aggregation errors in
1185 atmospheric transport inversions, J. Geophys. Res., 106, 4703–4715, 2001.
1186 Kawa, S. R., Erickson III, D. J., Pawson, S., and Zhu, Z.: Global CO_2 transport simulations using
1187 meteorological data from the NASA data assimilation system, J. Geophys. Res., 109,
1188 D18312, doi:10.1029/2004JD004554, 2004.
1189 Kawa, S. R., Mao, J., Abshire, J. B., Collatz, G. J., Sun, X., and Weaver, C. J.: Simulation
1190 studies for a space-based CO_2 lidar mission, Tellus B, 62, 759-769, doi:10.1111/j.1600-
1191 0889.2010.00486.x, 2010.
1192 Kim, J., Kim, H. M., Cho, C.-H., Boo, K.-O., Jacobson, A. R., Sasakawa, M., Machida, T.,
1193 Arshinov, M., and Fedoseev, N.: Impact of Siberian observations on the optimization of
1194 surface CO_2 flux, Atmos. Chem. Phys., 17, doi:10.5194/acp-17-2881-2017, 2017.
1195 Kulawik, S., Wunch, D., O'Dell, C., Frankenberg, C., Reuter, M., Oda, T., Chevallier, F.,
1196 Sherlock, V., Buchwitz, M., Osterman, G., Miller, C. E., Wennberg, P. O., Griffith, D.,
1197 Morino, I., Dubey, M. K., Deutscher, N. M., Notholt, J., Hase, F., Warneke, T., Sussmann,
1198 R., Robinson, J., Strong, K., Schneider, M., De Mazière, M., Shiomi, K., Feist, D. G., Iraci,
1199 L. T., and Wolf, J.: Consistent evaluation of ACOS-GOSAT, BESD-SCIAMACHY,

CarbonTracker, and MACC through comparisons to TCCON, Atmos. Meas. Tech., 9, 683–709, doi:10.5194/amt-9-683-2016, 2016.

Law, R. M., et al.: TransCom model simulations of hourly atmospheric CO_2: Experimental overview and diurnal cycle results for 2002, Global Biogeochem. Cycles, 22, GB3009, doi:10.1029/2007GB003050, 2008.

Le Quéré, C., Andres, R. J., Boden, T., Conway, T., Houghton, R. A., House, J. I., Marland, G., Peters, G. P., van der Werf, G. R., Ahlström, A., Andrew, R. M., Bopp, L., Canadell, J. G., Ciais, P., Doney, S. C., Enright, C., Friedlingstein, P., Huntingford, C., Jain, A. K., Jourdain, C., Kato, E., Keeling, R. F., Klein Goldewijk, K., Levis, S., Levy, P., Lomas, M., Poulter, B., Raupach, M. R., Schwinger, J., Sitch, S., Stocker, B. D., Viovy, N., Zaehle, S., and Zeng, N.: The global carbon budget 1959–2011, Earth Syst. Sci. Data, 5, 165–185, doi:10.5194/essd-5-165-2013, 2013.

Le Quéré, C., Moriarty, R., Andrew, R. M., Canadell, J. G., Sitch, S., Korsbakken, J. I., Friedlingstein, P., Peters, G. P., Andres, R. J., Boden, T. A., Houghton, R. A., House, J. I., Keeling, R. F., Tans, P., Arneth, A., Bakker, D. C. E., Barbero, L., Bopp, L., Chang, J., Chevallier, F., Chini, L. P., Ciais, P., Fader, M., Feely, R. A., Gkritzalis, T., Harris, I., Hauck, J., Ilyina, T., Jain, A. K., Kato, E., Kitidis, V., Klein Goldewijk, K., Koven, C., Landschützer, P., Lauvset, S. K., Lefévre, N., Lenton, A., Lima, I. D., Metzl, N., Millero, F., Munro, D. R., Murata, A., Nabel, J., Nakaoka, S., Nojiri, Y., O'Brien, K., Olsen, A., Ono, T., Pérez, F. F., Pfeil, B., Pierrot, D., Poulter, B., Rehder, G., Rödenbeck, C., Saito, S., Schuster, U., Schwinger, J., Séférian, R., Steinhoff, T., Stocker, B. D., Sutton, A. J., Takahashi, T., Tilbrook, B., van der Laan-Luijkx, I. T., van der Werf, G. R., van Heuven, S., Vandemark,

D., Viovy, N., Wiltshire, A., Zaehle, S., and Zeng, N.: Global Carbon Budget 2015. Earth System Science Data, 7:349-396. doi:10.5194/essd-7-349-2015, 2015.

Lindqvist, H., et al.: Does GOSAT capture the true seasonal cycle of carbon dioxide?, Atmos. Chem. Phys., 15, 13023–13040, doi:10.5194/acp-15-13023-2015, 2015.

Liu, J., Bowman, K. W., Lee, M., Henze, D. K., Bousserez, N., Brix, H., Collatz, G. J., Menemenlis, D., Ott, L., Pawson, S., Jones, D., and Nassar, R.: Carbon monitoring system flux estimation and attribution: Impact of ACOS-GOSAT XCO_2 sampling on the inference of terrestrial biospheric sources and sinks, Tellus B, 66, 22,486, doi:10.3402/tellusb.v66.22486, 2014.

Los, S. O., Collatz, G. J., Sellers, P. J., Malmström, C. M., Pollack, N. H., DeFries, R. S., Bounoua, L., Parris, M. T., Tucker, C. J., and Dazlich, D. A.: A global 9-yr biophysical land surface dataset from NOAA AVHRR data. J. Hydrometeorol., 1, 183–199, 2000.

Maksyutov, S., et al.: Regional CO_2 flux estimates for 2009–2010 based on GOSAT and ground-based CO_2 observations, Atmos. Chem. Phys., 13, 9351–9373, 2013.

Nassar, R., Jones, D. B. A., Suntharalingam, P., Chen, J. M., Andres, R. J., Wecht, K. J., Yantosca, R. M., Kulawik, S. S., Bowman, K. W., Worden, J. R., Machida, T., and Matsueda, H.: Modeling global atmospheric CO_2 with improved emission inventories and CO_2 production from the oxidation of other carbon species, Geosci. Model Dev., 3, 689–716, doi:10.5194/gmd-3-689-2010, 2010.

Niwa, Y., Machida, T., Sawa, Y., Matsueda, H., Schuck, T. J., Brenninkmeijer, C. A. M., Imasu, R., and Satoh, M.: Imposing strong constraints on tropical terrestrial CO_2 fluxes using

passenger aircraft based measurements, J. Geophys. Res., 117, D11303, doi:10.1029/2012JD017474, 2012.

O'Dell, C. W., et al.: The ACOS CO_2 retrieval algorithm Part 1: Description and validation against synthetic observations, Atmos. Meas. Tech., 5, 99–121, 2012.

Olsen, S. C. and Randerson, J. T.: Differences between surface and column atmospheric CO_2 and implications for carbon cycle research, Journal of Geophysical Research, 109, D02301, doi:10.1029/2003JD003968, 2004.

Orbe, C., Holzer, M., Polvani, L. M., and Waugh, D.: Air-mass origin as a diagnostic of tropospheric transport, J. Geophys. Res. Atmos., 118, 1459–1470, doi:10.1002/jgrd.50133, 2013.

Osterman, G., Eldering, A., Avis, C., O'Dell, C., Martinez, E., Crisp, D., Frankenberg, C., and Frankenberg, B.: ACOS Level 2 Standard Product Data User's Guide, v3.4, Jet Propulsion Laboratory, Pasadena, California, 2013.

Pan, Y., Birdsey, R. A., Fang, J., Houghton, R., Kauppi, P. E., Kurz, W. A., Phillips, O. L., Shvidenko, A., Lewis, S. L., Canadell, J. G., Ciais, P., Jackson, R. B., Pacala, S., McGuire, A. D., Piao, S., Rautiainen, A., Sitch, S., and Hayes, D.: A Large and Persistent Carbon Sink in the World's Forests, Science, 333, 988-993, doi: 10.1126/science.1201609, 2011.

Parazoo, N. C., Denning, A. S., Kawa, S. R., Corbin, K. D., Lokupitiya, R. S., and Baker, I. T.: Mechanisms for synoptic variations of atmospheric CO_2 in North America, South America and Europe, Atmos. Chem. Phys., 8, 7239-7254, https://doi.org/10.5194/acp-8-7239-2008, 2008.

Patra, P. K., Houweling, S., Krol, M., Bousquet, P., Belikov, D., Bergmann, D., Bian, H., Cameron-Smith, P., Chipperfield, M. P., Corbin, K., Fortems-Cheiney, A., Fraser, A., Gloor, E., Hess, P., Ito, A., Kawa, S. R., Law, R. M., Loh, Z., Maksyutov, S., Meng, L., Palmer, P. I., Prinn, R. G., Rigby, M., Saito, R., and Wilson, C.: TransCom model simulations of CH_4 and related species: linking transport, surface flux and chemical loss with CH_4 variability in the troposphere and lower stratosphere, Atmos. Chem. Phys., 11, 12813–12837, doi:10.5194/acp-11-12813-2011, 2011.

Peters, W., Jacobson, A. R., Sweeney, C., Andrews, A. E., Conway, T. J., Masarie, K., Miller, J. B., Bruhwiler, L. M. P., Pétron, G., Hirsch, A. I., Worthy, D. E. J., van der Werf, G. R., Randerson, J. T., Wennberg, P. O., Krol, M. C., and Tans, P. P.: An atmospheric perspective on North American carbon dioxide exchange: CarbonTracker, PNAS, 104, 18925-18930, 2007.

Pinzon, J. E. and Tucker, C. J.: A non-stationary 1981-2012 AVHRR $NDVI_{3g}$ time series, Remote Sensing 6, 6929-6960; doi:10.3390/rs6086929, 2014.

Randerson, J. T., Thompson, M. V., and Malmstrom, C. M.: Substrate limitations for heterotrophs: Implications for models that estimate the seasonal cycle of atmospheric CO_2, Global Biogeochem. Cycles, 10(4), 585–602, doi:10.1029/96GB01981, 1996.

Rayner, P. J., Enting, I. G., Francey, R. J., and Langenfelds, R.: Reconstructing the recent carbon cycle from atmospheric CO_2, $\delta^{13}C$ and O_2/N_2 observations, Tellus B, 51, 213–232, 1999.

Reuter, M., et al.: Satellite-inferred European carbon sink larger than expected, Atmos. Chem. Phys. Discuss., 14, 21,829–21,863, doi:10.5194/acpd-14-21829-2014, 2014.

1285 Reuter, M., Buchwitz, M., Hilker, M., Heymann, J., Bovensmann, H., Burrows, J. P.,
1286 Houweling, S., Liu, Y. Y., Nassar, R., Chevallier, F., Ciais, P., Marshall, J., and Reichstein,
1287 M.: How much CO_2 is taken up by the European terrestrial biosphere?, BAMS, 665-671,
1288 doi:10.1175/bams-d-15-00310.1, 2017.
1289 Rienecker, M. M., Suarez, M. J., Gelaro, R., Todling, R., Bacmeister, J., Liu, E., Bosilovich, M.
1290 G., Schubert, S. D., Takacs, L., Kim, G.-K., Bloom, S., Chen, J., Collins, D., Conaty, A., Da
1291 Silva, A., Gu, W., Joiner, J., Koster, R. D., Lucchesi, R., Molod, A., Owens, T., Pawson, S.,
1292 Pegion, P., Redder, C. R., Reichle, R., Robertson, F. R., Ruddick, A. G., Sienkiewicz, M.,
1293 and Woollen, J.: MERRA: NASA's Modern-Era Retrospective Analysis for Research and
1294 Applications, J. Climate, 24, 3624–3648, 2011.
1295 Rodgers, C. D.: Inverse Methods for Atmospheric Sounding: Theory and Practice, World
1296 Scientific, Singapore, 2000.
1297 Saeki, T., Maksyutov, S., Saito, M., Valsala, V., Oda, T., Andres, R. J., Belikov, D., Tans, P.,
1298 Dlugokencky, E., Yoshida, Y., Morino, I., Uchino, O., and Yokota, T.: Inverse modeling of
1299 CO_2 fluxes using GOSAT data and multi-year ground-based observations, Sci. Online Lett.
1300 Atmos., 9, 45–50, doi:10.2151/sola.2013-011, 2013a.
1301 Saeki, T., Maksyutov, S., Sasakawa, M., Machida, T., Arshinov, M., Tans, P., Conway, T. J.,
1302 Saito, M., Valsala, V., Oda, T., Andres, R. J., and Belikov, D.: Carbon flux estimation for
1303 Siberia by inverse modeling constrained by aircraft and tower CO_2 measurements, J.
1304 Geophys. Res., 118, doi:10.1002/jgrd.50127, 2013b.
1305 Saito, R., Patra, P. K., Sweeney, C., Machida, T., Krol, M., Houweling, S., Bousquet, P., Agusti-
1306 Panareda, A., Belikov, D., Bergmann, D., Bian, H. S., Cameron-Smith, P., Chipperfield, M.

P., Fortems-Cheiney, A., Fraser, A., Gatti, L. V., Gloor, E., Hess, P., Kawa, S. R., Law, R. M., Locatelli, R., Loh, Z., Maksyutov, S., Meng, L., Miller, J. B., Palmer, P. I., Prinn, R. G., Rigby, M. and Wilson, C.: TransCom model simulations of methane: Comparison of vertical profiles with aircraft measurements, J. Geophys. Res., 118, 3891-3904, doi:10.1002/jgrd.50380, 2013.

Saitoh, N., Kimoto, S., Sugimura, R., Imasu, R., Shiomi, K., Kuze, A., Niwa, Y., Machida, T., Sawa, Y., and Matsueda, H.: Bias assessment of lower and middle tropospheric CO_2 concentrations of GOSAT/TANSO-FTS TIR version 1 product, Atmos. Meas. Tech., 10, 3877–3892, doi:10.5194/amt-10-3877-2017, 2017a.

Saitoh, N., Yamada, A., Itatsu, T., Imasu, R., Shiomi, K., and Niwa, Y.: Algorithm development for the TIR bands of GOSAT-2/TANSO-FTS-2: lessons from GOSAT/TANSO-FTS TIR CO_2 and CH_4 measurement, AGU Fall Meeting, New Orleans, US, 11-15 Dec. 2017, A33G-2472, 2017b.

Sasakawa, M., Shimoyama, K., Machida, T., Tsuda, N., Suto, H., Arshinov, M., Davydov, D., Fofonov, A., Krasnov, O., Saeki, T., Koyama, Y., and Maksyutov, S.: Continuous measurements of methane from a tower network over Siberia, Tellus B: Chemical and Physical Meteorology, 62:5, 403-416, doi:10.1111/j.1600-0889.2010.00494.x, 2010.

Sasakawa, M., Machida, T., Tsuda, N., Arshinov, M., Davydov, D., Fofonov, A., and Krasnov, O.: Aircraft and tower measurements of CO_2 concentration in the planetary boundary layer and the lower free troposphere over southern taiga in West Siberia: Long-term records from 2002 to 2011, J. Geophys. Res., doi:10.1002/jgrd.50755, 2013.

Schimel, D., Stephens, B. B., and Fisher, J. B.: Effect of increasing CO_2 on the terrestrial carbon cycle, PNAS, 112, doi/10.1073/pnas.1407302112, 2015.

Stephens, B. B., et al.: Weak northern and strong tropical land carbon uptake from vertical profiles of atmospheric CO_2, Science, 316, 1732–1735, 2007.

Takagi, H., et al.: On the benefit of GOSAT observations to the estimation of regional CO_2 fluxes, Sci. Online Lett. Atmos., 7, 161–164, 2011.

Takagi, H., et al.: Influence of differences in current GOSAT XCO_2 retrievals on surface flux estimation, Geophys. Res. Lett., 41, 2598–2605, doi:10.1002/2013GL059174, 2014.

Takahashi, T., et al.: Climatological mean and decadal change in surface ocean pCO_2, and net sea-air CO_2 flux over the global oceans, Deep Sea Res., Part II, 56(8–10), 554–577, 2009.

Tarantola, A.: Inverse problem theory: methods for data fitting and model parameter estimation, Elsevier, Amsterdam, The Netherlands, 1987.

Tsutsumi, Y., Mori, K., Ikegami, M., Tashiro, T., and Tsuboi, K.: Long-term trends of greenhouse gases in regional and background events observed during 1998-2004 at Yonagunijima located to the east of the Asian continent, Atmospheric. Environment., 40, 5868-5879, 2006.

van der Werf, G. R., Randerson, J. T., Giglio, L., Collatz, G. J., Kasibhatla, P. S., and Arellano Jr., A. F.: Interannual variability in global biomass burning emissions from 1997 to 2004, Atmos. Chem. Phys., 6, 3423–3441, doi:10.5194/acp-6-3423-2006, 2006.

van der Werf, G. R., Randerson, J. T., Giglio, L., Collatz, G. J., Mu, M., Kasibhatla, P. S., Morton, D. C., DeFries, R. S., Jin, Y., and van Leeuwen, T. T.: Global fire emissions and the

contribution of deforestation, savanna, forest, agricultural, and peat fires (1997–2009), Atmos. Chem. Phys., 10, 11707–11735, doi:10.5194/acp-10-11707-2010, 2010.

van der Werf, G. R., Randerson, J. T., Giglio, L., van Leeuwen, T. T., Chen, Y., Rogers, B. M., Mu, M., van Marle, M. J. E., Morton, D. C., Collatz, G. J., Yokelson, R. J., and Kasibhatla, P. S.: Global fire emissions estimates during 1997–2016, Earth Syst. Sci. Data, 9, 697-720, doi:10.5194/essd-9-697-2017, 2017.

Wargan, K., Pawson, S., Olsen, M. A., Witte, J. C., Douglass, A. R., Ziemke, J. R., Strahan, S. E., and Nielsen, J. E.: The global structure of upper troposphere-lower stratosphere ozone in GEOS-5: A multiyear assimilation of EOS Aura data, J. Geophys. Res. Atmos., 120, 2013–2036, doi:10.1002/2014JD022493, 2015.

Wofsy, S. C., et al.: HIAPER Pole-to-Pole Observations (HIPPO): fine-grained, global-scale measurements of climatically important atmospheric gases and aerosols, Philos. T. R. Soc. A, 369, 2073–2086, doi:10.1098/rsta.2010.0313, 2011.

Wofsy, S. C., et al.: HIPPO Merged 10-second Meteorology, Atmospheric Chemistry, Aerosol Data (R_20121129), Carbon Dioxide Information Analysis Center, Oak Ridge National Laboratory, Oak Ridge, Tennessee, U.S.A. http://dx.doi.org/10.3334/CDIAC/hippo_010 (Release 20121129), 2012.

Wunch, D., Wennberg, P. O., Toon, G. C., Connor, B. J., Fisher, B., Osterman, G. B., Frankenberg, C., Mandrake, L., O'Dell, C., Ahonen, P., Biraud, S. C., Castano, R., Cressie, N., Crisp, D., Deutscher, N. M., Eldering, A., Fisher, M. L., Griffith, D. W. T., Gunson, M., Heikkinen, P., Keppel-Aleks, G., Kyrö, E., Lindenmaier, R., Macatangay, R., Mendonca, J., Messerschmidt, J., Miller, C. E., Morino, I., Notholt, J., Oyafuso, F. A., Rettinger, M.,

Robinson, J., Roehl, C. M., Salawitch, R. J., Sherlock, V., Strong, K., Sussmann, R., Tanaka, T., Thompson, D. R., Uchino, O., Warneke, T., and Wofsy, S. C.: A method for evaluating bias in global measurements of CO_2 total columns from space, Atmos. Chem. Phys., 11, 12317–12337, doi:10.5194/acp-11-12317-2011, 2011.

Xu, L., Samanta, A., Costa, M. H., Ganguly, S., Nemani, R. R., and Myneni, R. B.: Widespread decline in greenness of Amazonian vegetation due to the 2010 drought, Geophys. Res. Lett., 38, L07402, doi:10.1029/2011GL046824, 2011.

Yokota, T., Yoshida, Y., Eguchi, N., Ota, Y., Tanaka, T., Watanabe, H., and Maksyutov, S.: Global concentrations of CO_2 and CH_4 retrieved from GOSAT: first preliminary results, SOLA, 5, 160–163, doi:10.2151/sola.2009-041, 2009.

1382 **Table 1.** Inversion Prior and Posterior Fluxes and Uncertainties Aggregated to TransCom 3 Regions, June 2009-May 2010.

TransCom Region	Prior		Fires	In Situ-Only			GOSAT-Only			In Situ + GOSAT			In Situ-Only, Tighter Prior			GOSAT-Only, Tighter Prior		
	Flux[a]	Unc	Flux	Flux	Unc	U.R. (%)[b]	Flux	Unc	U.R. (%)	Flux	Unc	U.R. (%)	Flux	Unc	U.R. (%)	Flux	Unc	U.R. (%)
Boreal North America	-0.1	0.6	0.1	0.1	0.1	81	0.2	0.3	43	0.1	0.1	87	-0.1	0.1	71	0.0	0.2	27
Temperate North America	-0.3	1.5	0.0	-0.6	0.1	93	-1.5	0.3	82	-0.7	0.1	96	-0.6	0.1	87	-1.2	0.2	71
Tropical America	0.4	1.0	0.1	-0.4	0.7	33	-0.2	0.2	79	-0.3	0.2	82	-0.2	0.3	26	-0.1	0.1	67
Temperate South America	0.4	1.2	0.1	0.4	0.8	31	1.1	0.2	85	1.0	0.2	85	0.3	0.3	27	0.9	0.1	73
Northern Africa	0.2	1.1	0.4	1.5	0.7	38	2.0	0.2	83	1.8	0.2	84	1.1	0.3	28	2.0	0.1	70
Southern Africa	0.0	1.2	0.8	-0.1	0.7	44	-0.6	0.1	89	-0.5	0.1	89	-0.1	0.3	38	-0.6	0.1	80
Boreal Asia	-0.1	1.2	0.1	-1.2	0.4	70	-0.5	0.4	65	-1.2	0.2	87	-1.0	0.2	60	-0.5	0.2	51
Temperate Asia	0.0	1.8	0.1	-0.1	0.7	61	1.4	0.4	79	0.9	0.3	85	-0.5	0.3	53	1.0	0.2	67
Tropical Asia	0.3	0.6	0.4	0.0	0.4	33	0.5	0.3	54	0.7	0.2	61	0.4	0.2	25	0.8	0.1	39
Australia	0.0	0.5	0.1	-0.2	0.4	15	0.6	0.2	71	0.3	0.1	73	-0.2	0.2	12	0.3	0.1	56
Europe	-0.1	1.3	0.0	0.6	0.4	70	-1.5	0.3	75	-0.6	0.2	87	0.3	0.2	61	-1.6	0.2	64
North Pacific Ocean	-0.5	0.3	0.0	-0.9	0.1	51	-0.5	0.2	29	-1.1	0.1	67	-0.8	0.1	29	-0.5	0.1	11
Tropical West Pacific Ocean	0.1	0.3	0.0	0.1	0.2	26	0.3	0.1	51	0.5	0.1	59	0.1	0.1	15	0.3	0.1	24
Tropical East Pacific Ocean	0.4	0.3	0.0	0.4	0.2	25	0.4	0.1	54	0.3	0.1	62	0.4	0.1	13	0.4	0.1	25
South Pacific Ocean	-0.3	0.6	0.0	-1.0	0.4	32	-1.1	0.3	51	-1.8	0.2	60	-0.6	0.2	18	-0.9	0.1	30
Arctic/Northern Ocean	-0.3	0.3	0.0	-0.4	0.1	56	-0.5	0.2	19	-0.1	0.1	62	-0.3	0.1	31	-0.4	0.1	5
North Atlantic Ocean	-0.2	0.2	0.0	-0.8	0.1	35	-0.5	0.1	23	-1.0	0.1	50	-0.5	0.1	12	-0.3	0.1	6
Tropical Atlantic Ocean	0.1	0.3	0.0	0.1	0.2	23	0.3	0.2	42	0.4	0.1	56	0.1	0.1	9	0.2	0.1	14
South Atlantic Ocean	-0.2	0.4	0.0	-0.5	0.3	19	-0.7	0.2	38	-1.0	0.2	49	-0.3	0.1	8	-0.5	0.1	18
Southern Ocean	-0.2	0.6	0.0	-0.4	0.3	48	-0.9	0.4	41	0.2	0.2	62	-0.5	0.1	34	-1.1	0.1	22
Tropical Indian Ocean	0.1	0.4	0.0	0.0	0.3	27	0.7	0.2	56	0.5	0.2	62	0.1	0.1	16	0.4	0.1	32
Southern Indian Ocean	-0.4	0.3	0.0	-0.5	0.2	15	-0.6	0.2	29	-0.6	0.2	40	-0.5	0.1	7	-0.4	0.1	11

[a]Fluxes in table, in Pg C, include fires but not fossil emissions

[b]Uncertainty reduction

1383 **Table 2.** Normalized Cost Function Values for the Inversions.

Inversion	**A Priori**	**A Posteriori**
In situ only	112.4	4.0
GOSAT only	2.2	0.8
In situ + GOSAT	12.2	1.1
In situ only, decreased prior uncertainties	112.4	5.0
GOSAT only, decreased prior uncertainties	2.2	0.8

1384

1385

Table 3. Mean 2010-2009 difference in mole fractions over June-July-August at Siberian sites (in ppm).

Site	Observations	Prior	GOSAT-Only Post	In Situ + GOSAT Post	Prior - Obs	(GOSAT-Only) - Obs	(In Situ + GOSAT) - Obs
VGN	5.2	5.3	7.4	6.6	0.1	2.2	1.4
AZV	7.0	6.3	8.1	7.1	-0.7	1.1	0.1
SVV	2.6	4.0	3.4	4.6	1.4	0.8	2.0
IGR	4.9	5.7	5.1	4.6	0.8	0.2	-0.3
KRS	6.6	5.4	3.8	3.2	-1.2	-2.8	-3.4
YAK	2.1	2.5	4.2	2.5	0.4	2.1	0.4

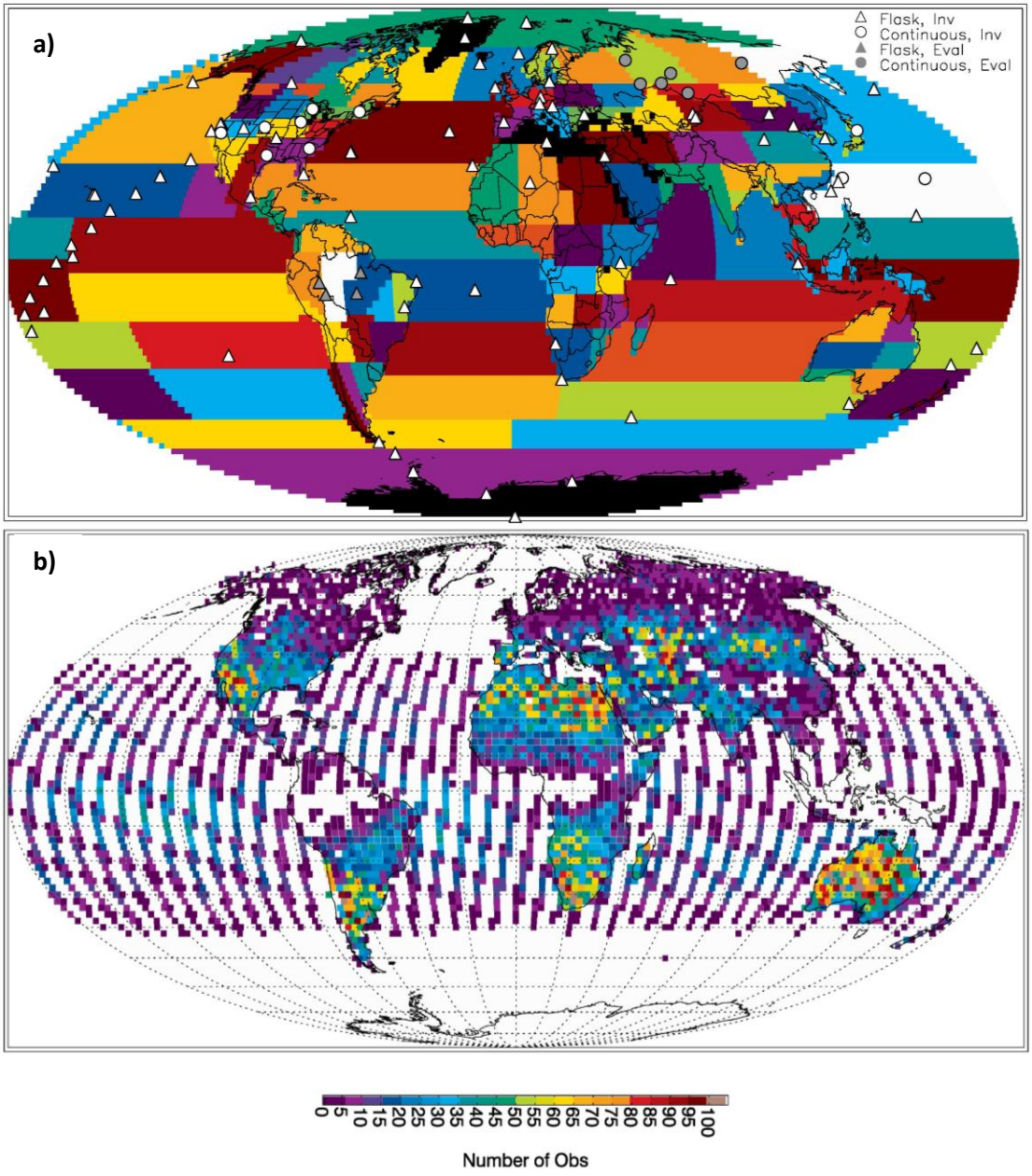

1389

1390 **Figure 1.** Locations of a) in situ observation sites and b) GOSAT XCO_2 observations used in the

1391 inversions. Also shown in a) are the 108 flux regions. Flask and continuous measurement sites

1392 in a) are represented by different symbols, and sites used in inversions and in their evaluation are

1393 represented by different colors. Observations in b) correspond to the ACOS B3.4 retrieval, are

filtered and averaged over each hour and 2° x 2.5° PCTM model grid column, and are shown for June 2009-May 2010.

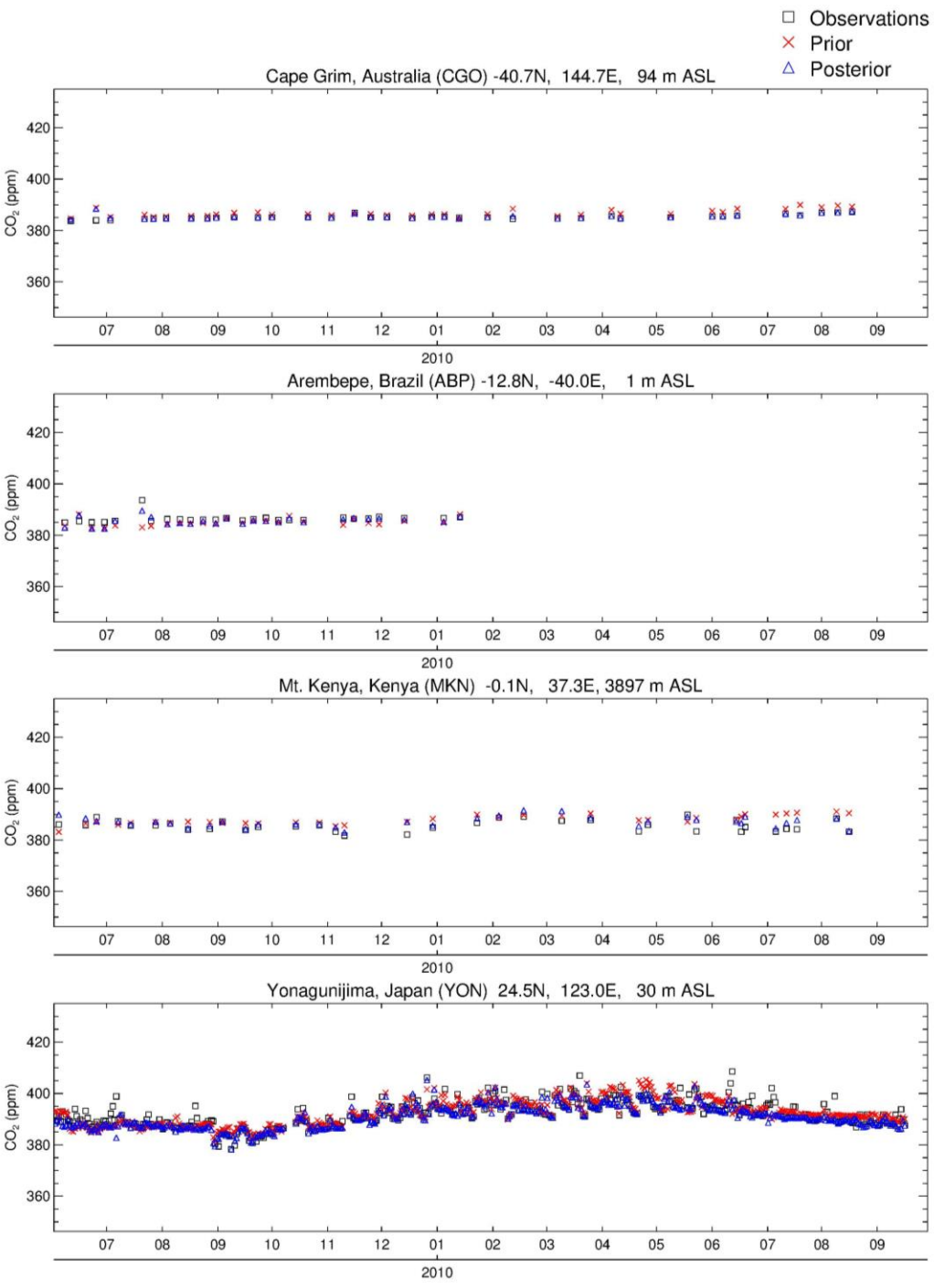
Observations
Prior
Posterior
Cape Grim, Australia (CGO) -40.7N, 144.7E, 94 m ASL
Arembepe, Brazil (ABP) -12.8N, -40.0E, 1 m ASL
Mt. Kenya, Kenya (MKN) -0.1N, 37.3E, 3897 m ASL
Yonagunijima, Japan (YON) 24.5N, 123.0E, 30 m ASL
CO2 (ppm)
360
380
400
420
07 08 09 10 11 12 01 02 03 04 05 06 07 08 09
2010

1396

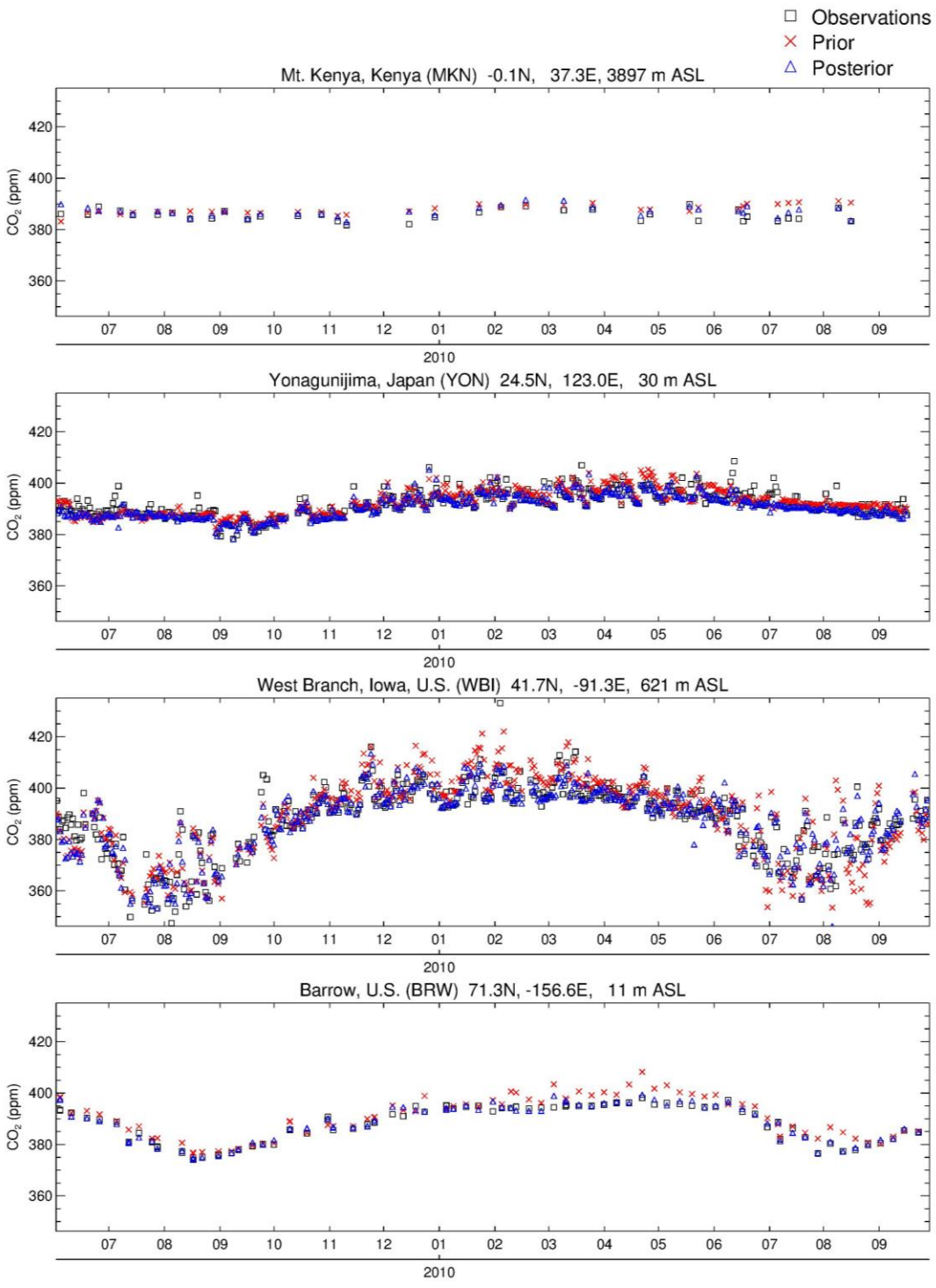

Figure 2. Comparison of model and observed time series of CO_2 mole fractions at selected surface sites. Posterior mole fractions are for the in situ-only inversion. Sites are arranged from

south to north. ~~Elevations~~ The elevation for the WBI site includes the intake heights~~s~~ on the towers~~ where applicable~~.

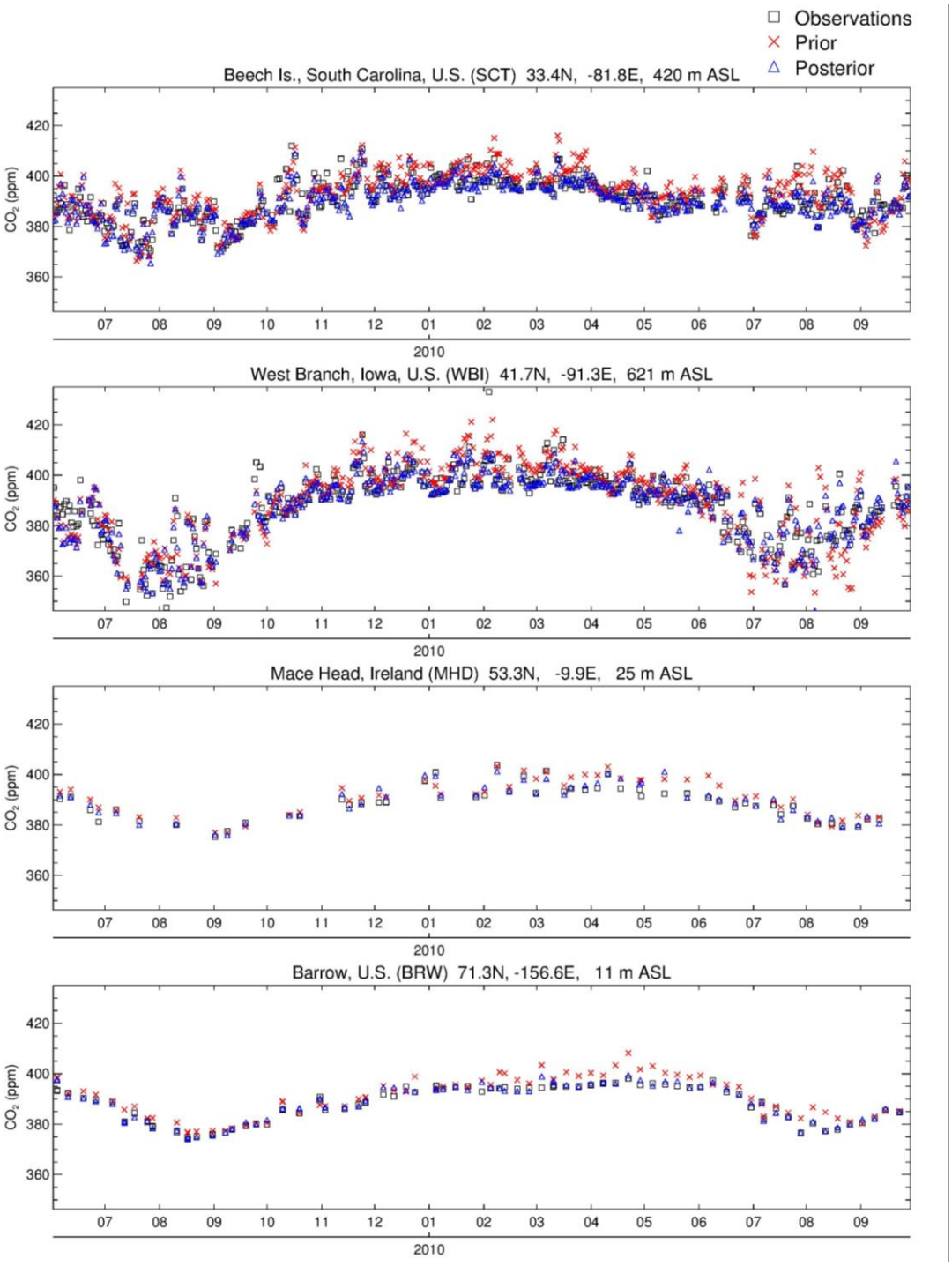

~~Figure 2.~~ ~~(continued)~~

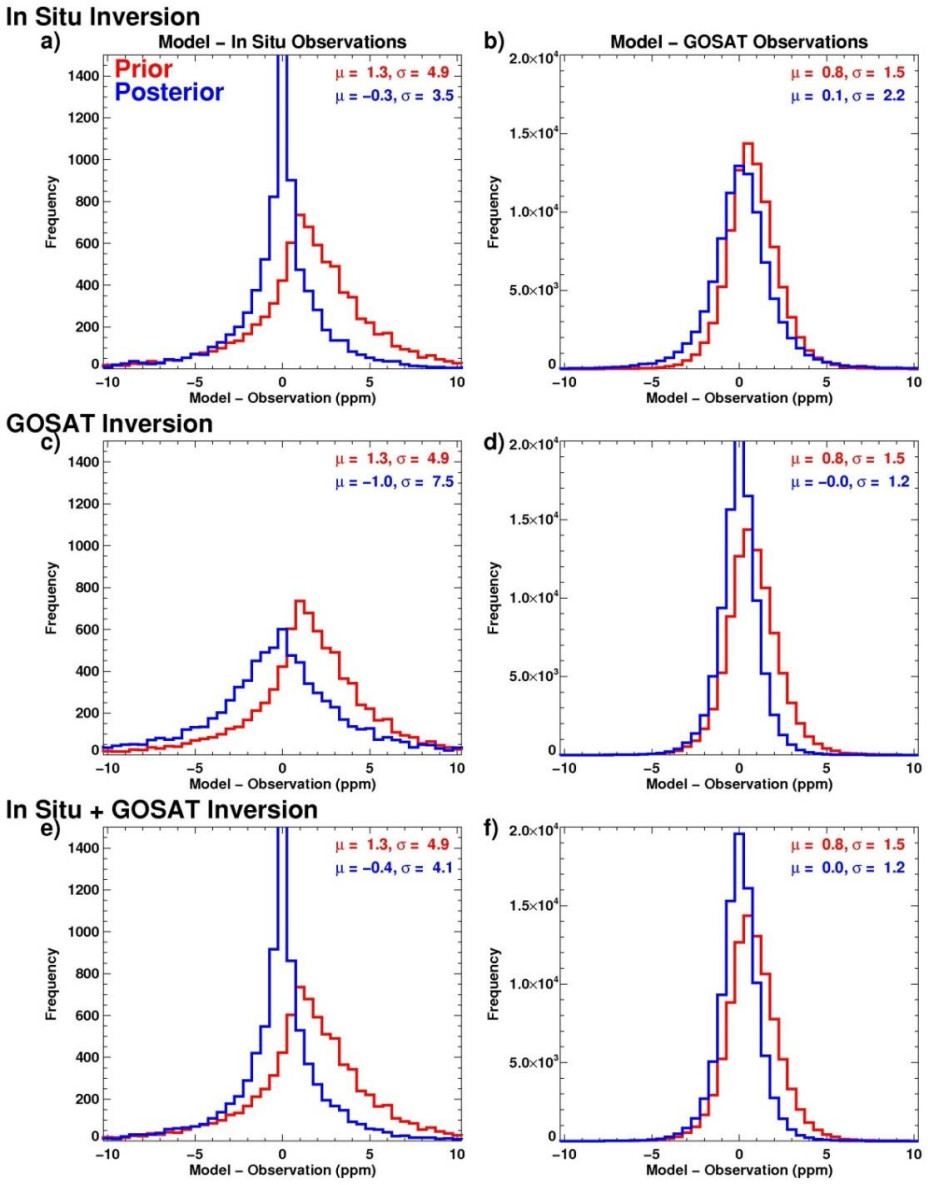

Figure 3. Full comparison of model and observations. Model-observation difference histograms are shown for (a) in situ-only inversion and in situ observations, (b) in situ-only inversion and GOSAT observations, (c) GOSAT-only inversion and in situ observations, (d) GOSAT-only inversion and GOSAT observations, (e) in situ + GOSAT inversion and in situ observations, and

1410 (f) in situ + GOSAT inversion and GOSAT observations. Mean differences and standard

1411 deviations are indicated in the panels.

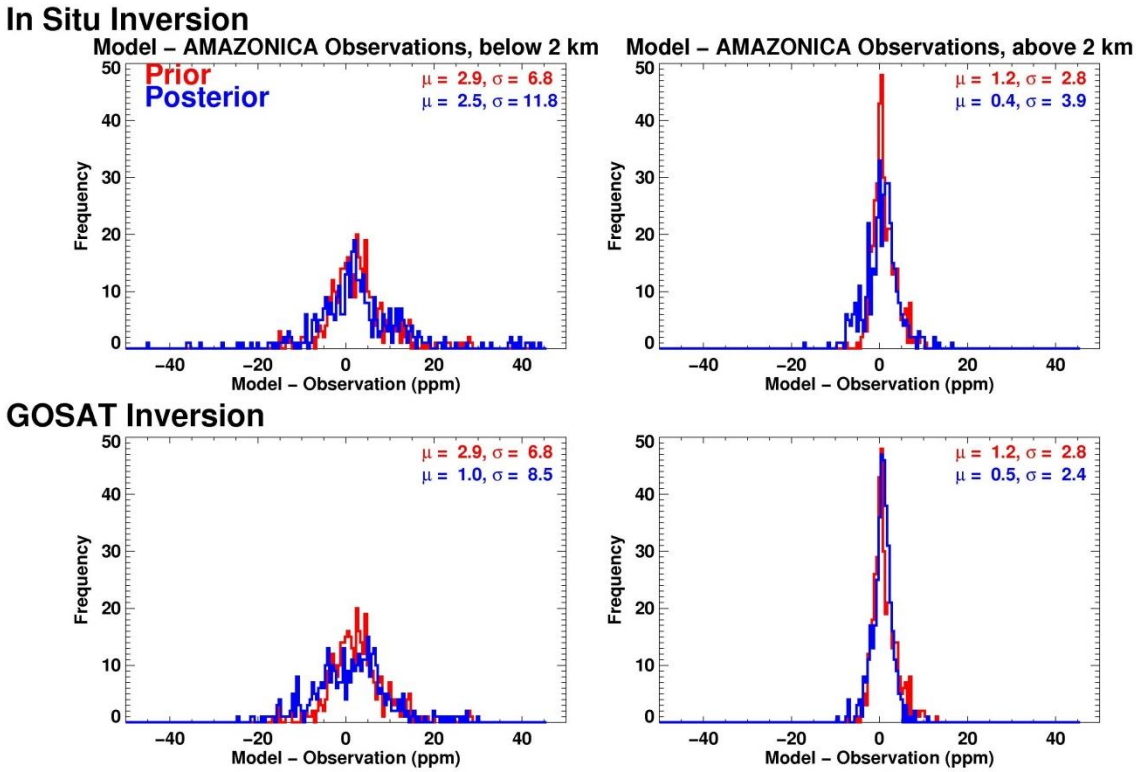

Figure 4. Comparison of model and Amazon aircraft observations (Amazonica project) over the period of overlap, Jan.-Sep. 2010. Top two panels show model-observation difference histograms for the in situ-only inversion and bottom two panels show results for the GOSAT-only inversion. Comparisons are shown separately for model and data below 2 km altitude (left) and above 2 km (right). Mean differences and standard deviations are indicated in the panels.

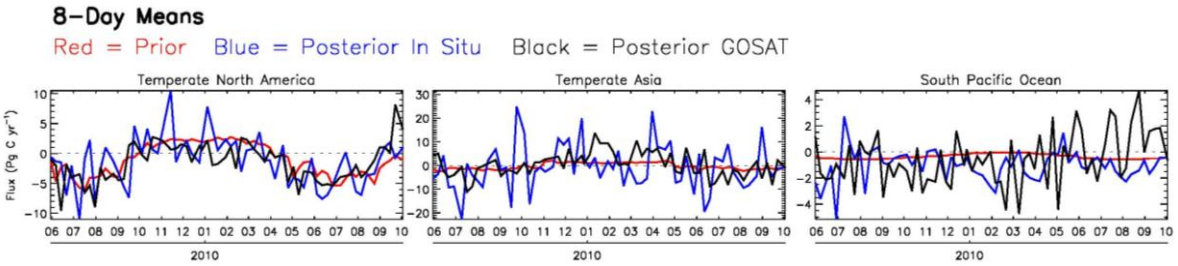

Figure 5. Prior, posterior in situ-only, and posterior GOSAT-only 8-day mean NEP (× -1) and ocean fluxes, aggregated over selected TransCom regions. Note that vertical scales are different in each of the panels.

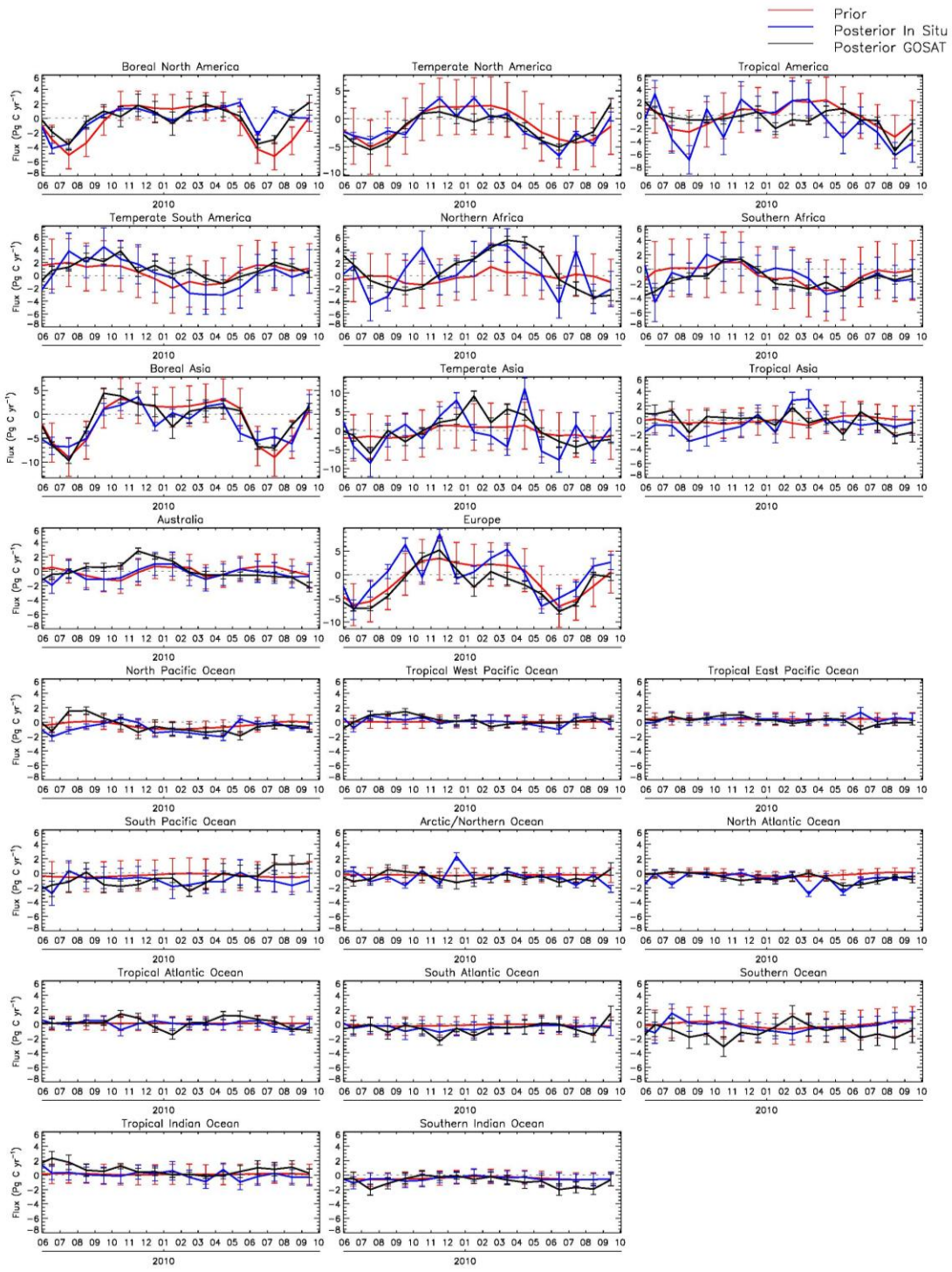

1424

1425 **Figure 6.** Same as Fig. 5, except showing monthly means of fluxes for all TransCom regions,

1426 with error bars that represent 1σ uncertainties. Component 8-day fluxes and error covariances

1427 are weighted by the proportions that lie within each particular month.

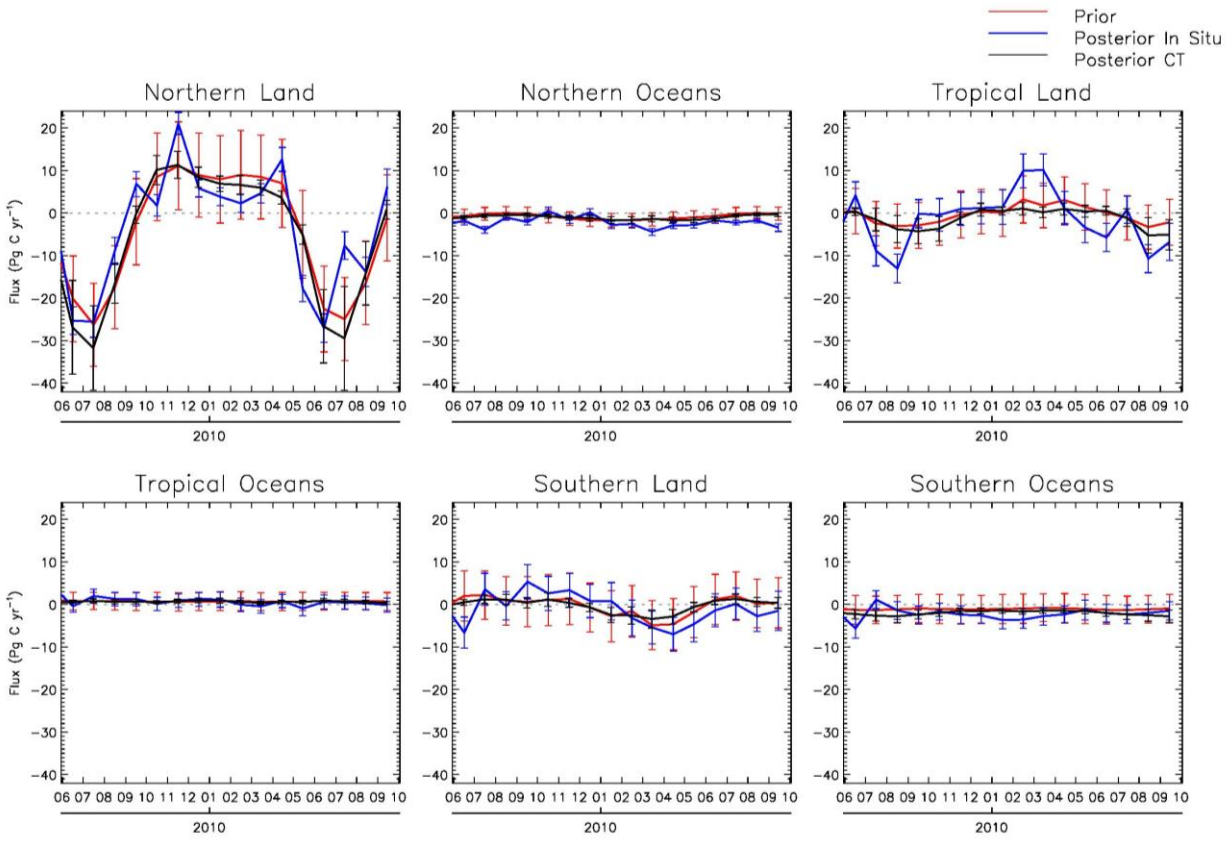

Figure 7. Comparison of our in situ-only inversion monthly mean NEP (× -1) and ocean fluxes, aggregated over large regions (as defined in TC3), with posterior fluxes from NOAA's CarbonTracker (CT2013B) data assimilation system. The priors shown are from our analysis; CT2013B priors are similar. Error bars represent 1σ uncertainties.

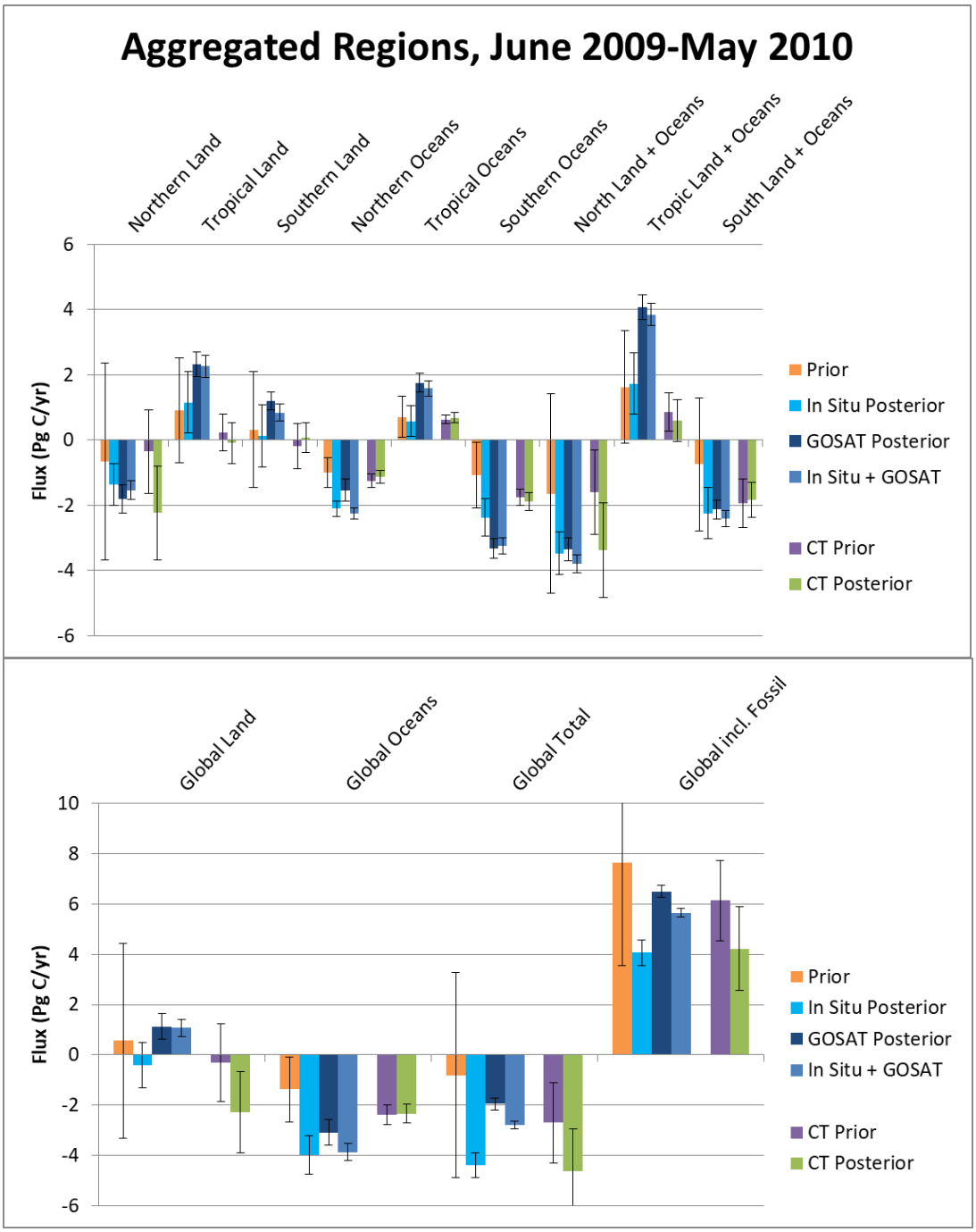

1435

1436

1437 **Figure 8.** Twelve-month mean NEP (× -1), fire, and ocean fluxes aggregated over large regions.

1438 Included are results for the in situ-only, GOSAT-only, and in situ + GOSAT inversions as well

1439 as priors. Shown for comparison are priors and posteriors from CT2013B. Error bars represent

1440 1σ uncertainties; for CT2013B, “external” (across a set of priors) as well as “internal” (within a
1441 particular inversion) uncertainties are included. In summing monthly CT2013B fluxes over the
1442 12 months, we assumed zero error correlation between months.
1443

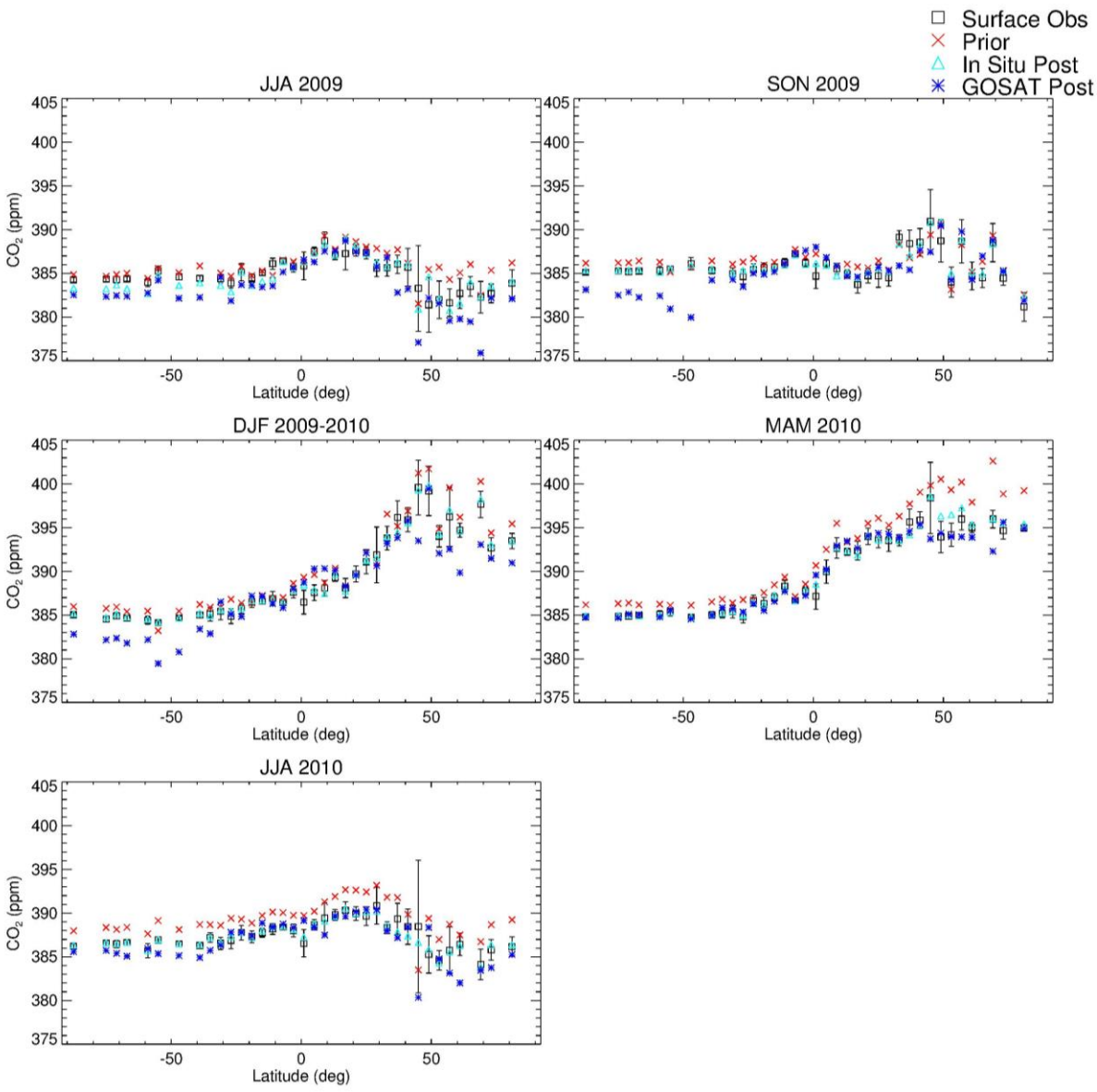

Figure 9. Latitudinal profiles of seasonal mean CO_2 mole fractions at surface sites for observations, prior, in situ-only posterior, and GOSAT-only posterior. Values are averaged in 4° bins. Error bars account for the spread of the observations within each season and bin as well as the uncertainty of each observation.

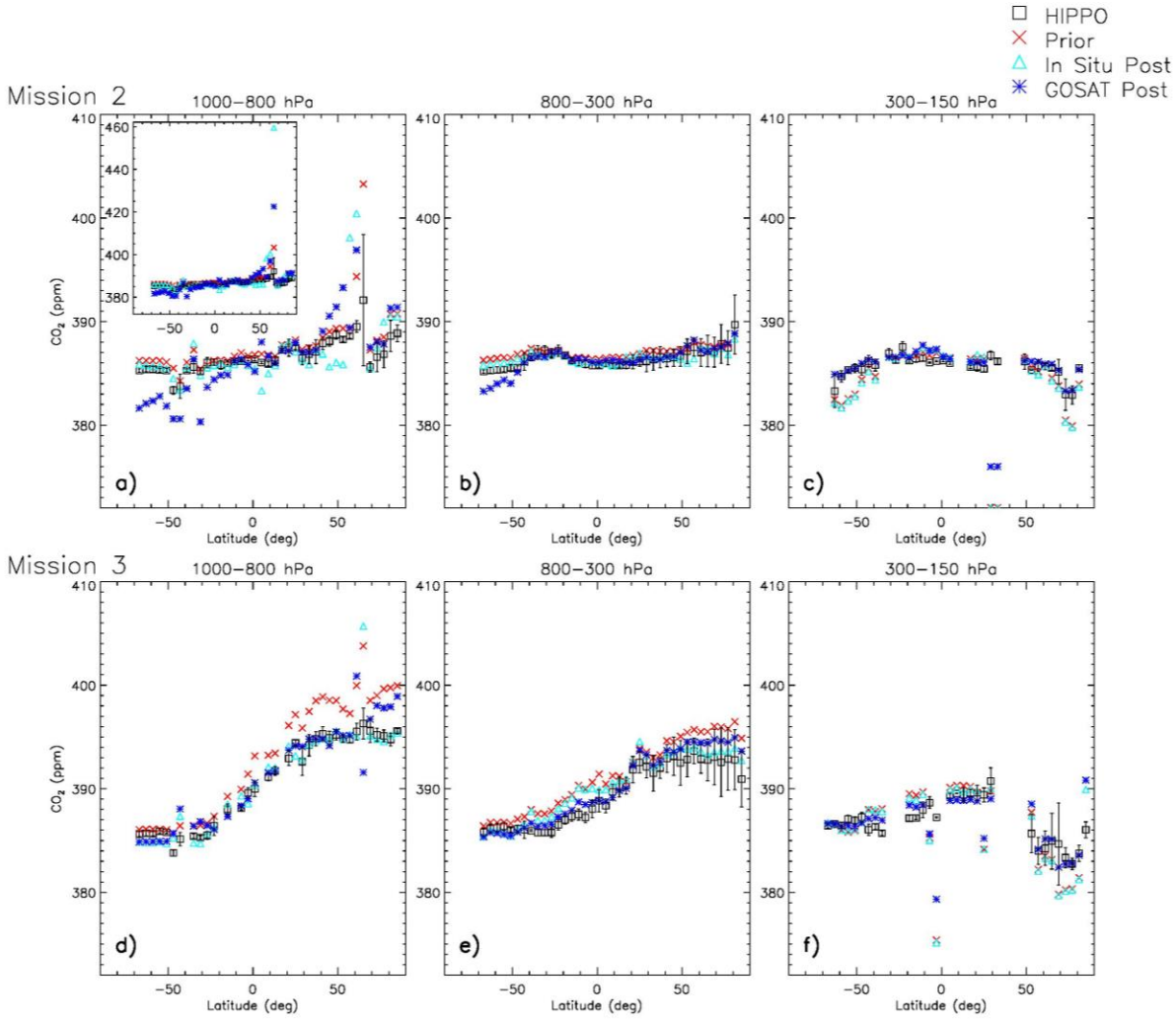

Figure 10. Latitudinal profiles of CO_2 mole fractions for HIPPO observations and co-sampled prior, in situ-only posterior, and GOSAT-only posterior. Mission 2 (panels a-c) took place during Oct 31-Nov 22, 2009; Mission 3 (d-f) took place Mar 24-Apr 16, 2010. Values are averaged in three altitude bins and 4° latitude bins. The inset in ~~the first panel~~a) contains an expanded y-axis range that shows two points that do not fit into the default range. Flight segments over the temperate North American continent (east of -130°) are excluded from this

comparison in order to focus on the Pacific. Error bars represent the standard deviations of the observations within each bin.

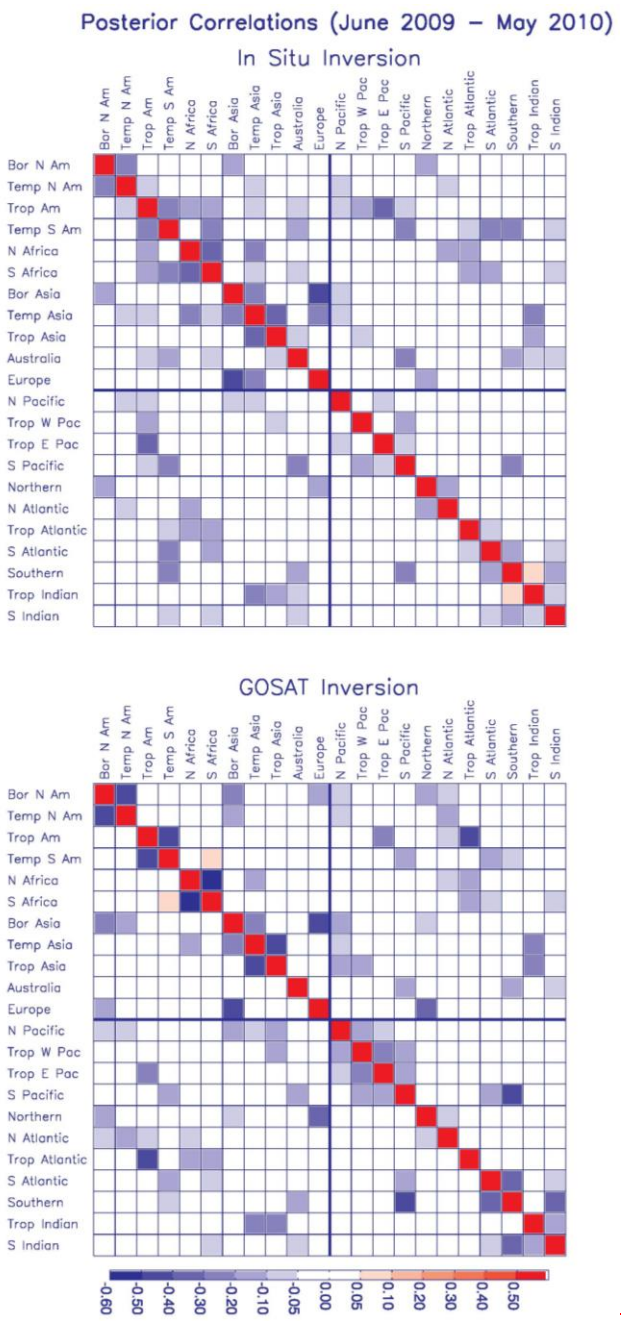
Posterior Correlations (June 2009 – May 2010)
In Situ Inversion
GOSAT Inversion
Bor N Am
Temp N Am
Trop Am
Temp S Am
N Africa
S Africa
Bor Asia
Temp Asia
Trop Asia
Australia
Europe
N Pacific
Trop W Pac
Trop E Pac
S Pacific
Northern
N Atlantic
Trop Atlantic
S Atlantic
Southern
Trop Indian
S Indian
-0.60
-0.50
-0.40
-0.30
-0.20
-0.10
-0.05
0.00
0.05
0.10
0.20
0.30
0.40
0.50

1458

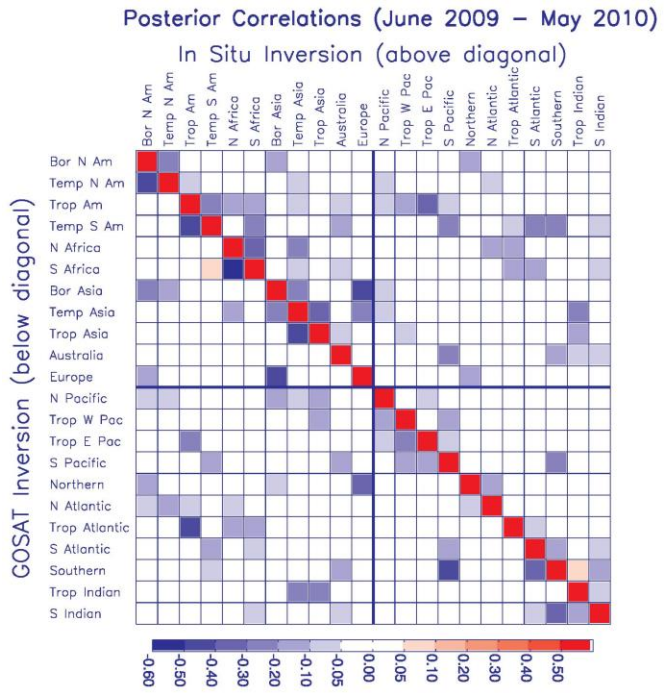

Figure 11. Posterior spatial flux error correlations, aggregated to TC3 regions and a 12-month period, for ~~(a)~~ the in situ-only inversion (for compactness, shown on and above the main diagonal), and ~~(b)~~ the GOSAT-only inversion (on and below the diagonal). The correlation is equal to the error covariance divided by the product of the corresponding flux uncertainties (σ). Values on the ~~main~~ diagonal are equal to 1.

1465

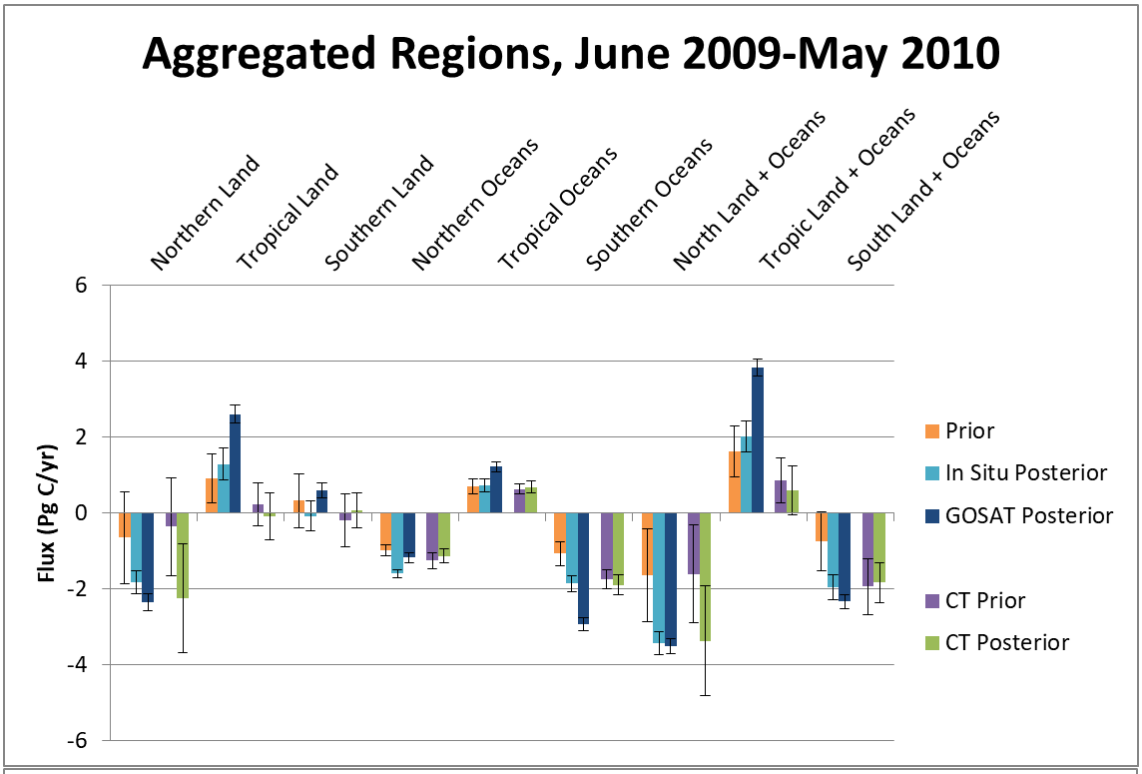

1466

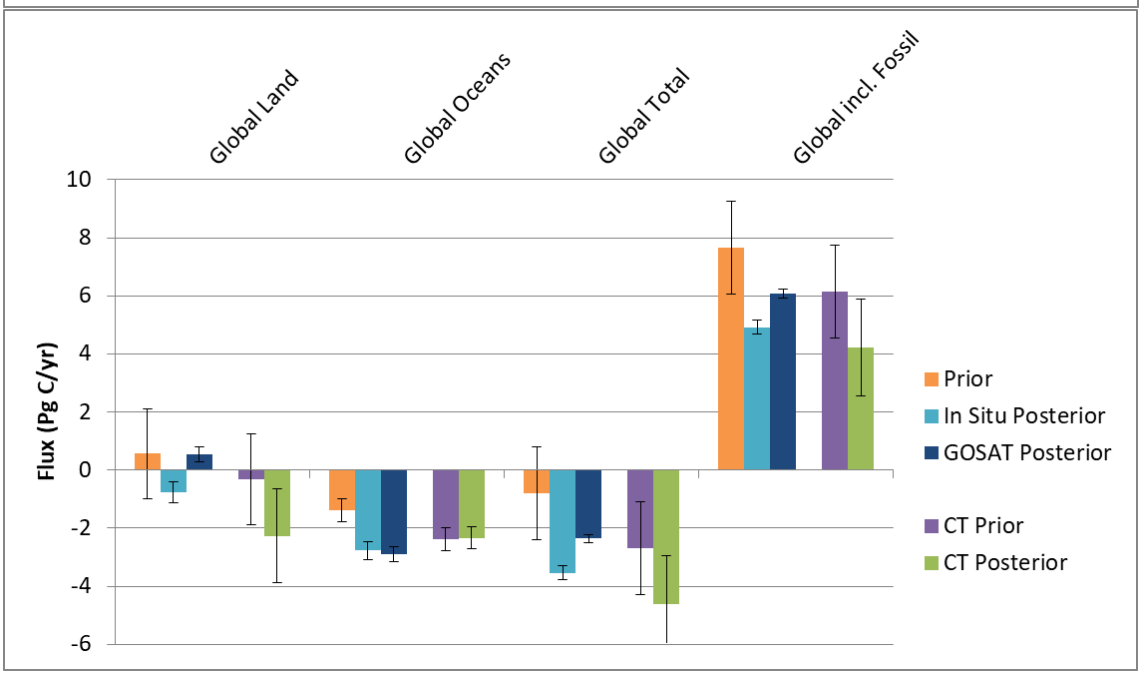

1467

Figure 12. Similar to Fig. 8, except showing results for inversions with tighter prior constraints (with prior uncertainties similar to CarbonTracker's). Included are results for the in situ-only and GOSAT-only inversions. CT2013B results shown in Fig. 8 are repeated here. Error bars represent 1σ uncertainties.

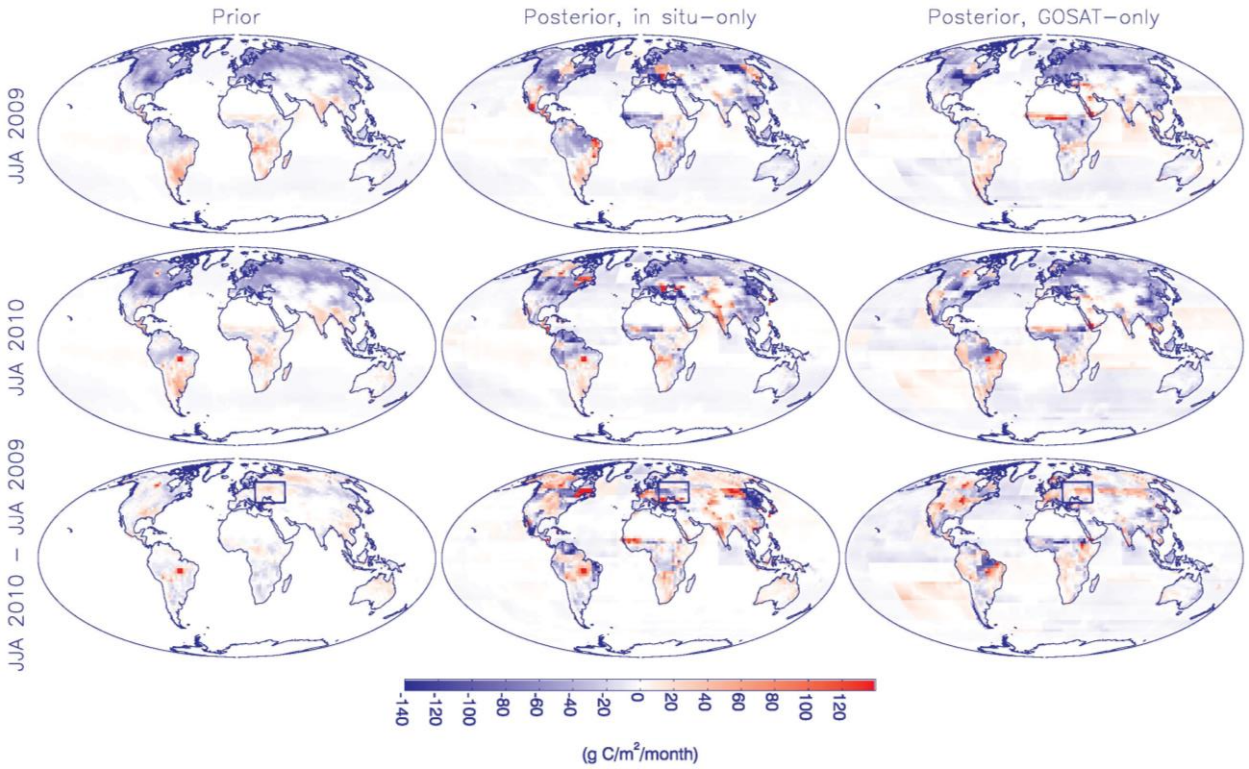

1473

1474 **Figure 13.** Comparison of spatial distribution of fluxes for June-July-August of 2010 vs. 2009.
1475 Included are natural and fire fluxes. Shown are fluxes for 2009 (top), 2010 (middle), and the
1476 2010-2009 difference (bottom), for the priors (left), in situ-only inversion (middle), and GOSAT-
1477 only inversion (right). In the bottom row, boxes enclose the region around western Russia where
1478 there were intense heat waves, severe drought, and extensive fires. Note that the grid-scale
1479 spatial variability shown is not optimized in the inversions, so only patterns at the scale of the
1480 108 flux regions contain information from the observations.

1481

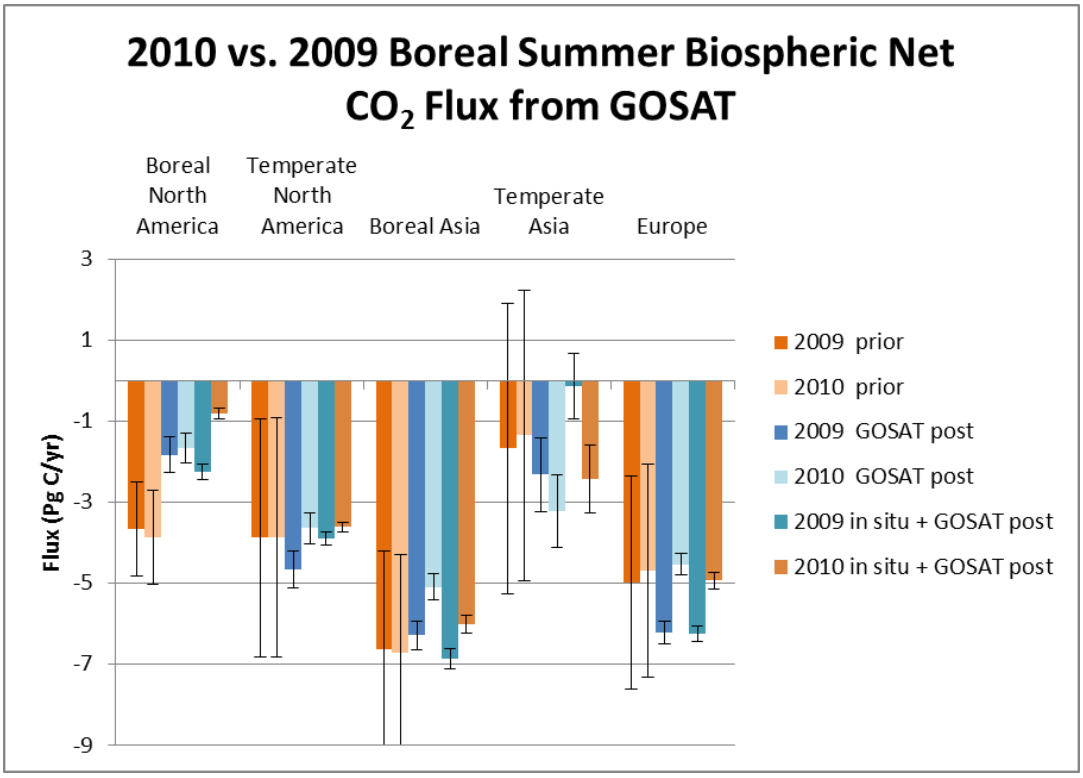

Figure 14. Comparison of prior, GOSAT-only posterior, and in situ + GOSAT posterior fluxes aggregated over northern regions for June-July-August of 2010 vs. 2009. Included are NEP (× -1) and fire fluxes. Error bars represent 1σ uncertainties.

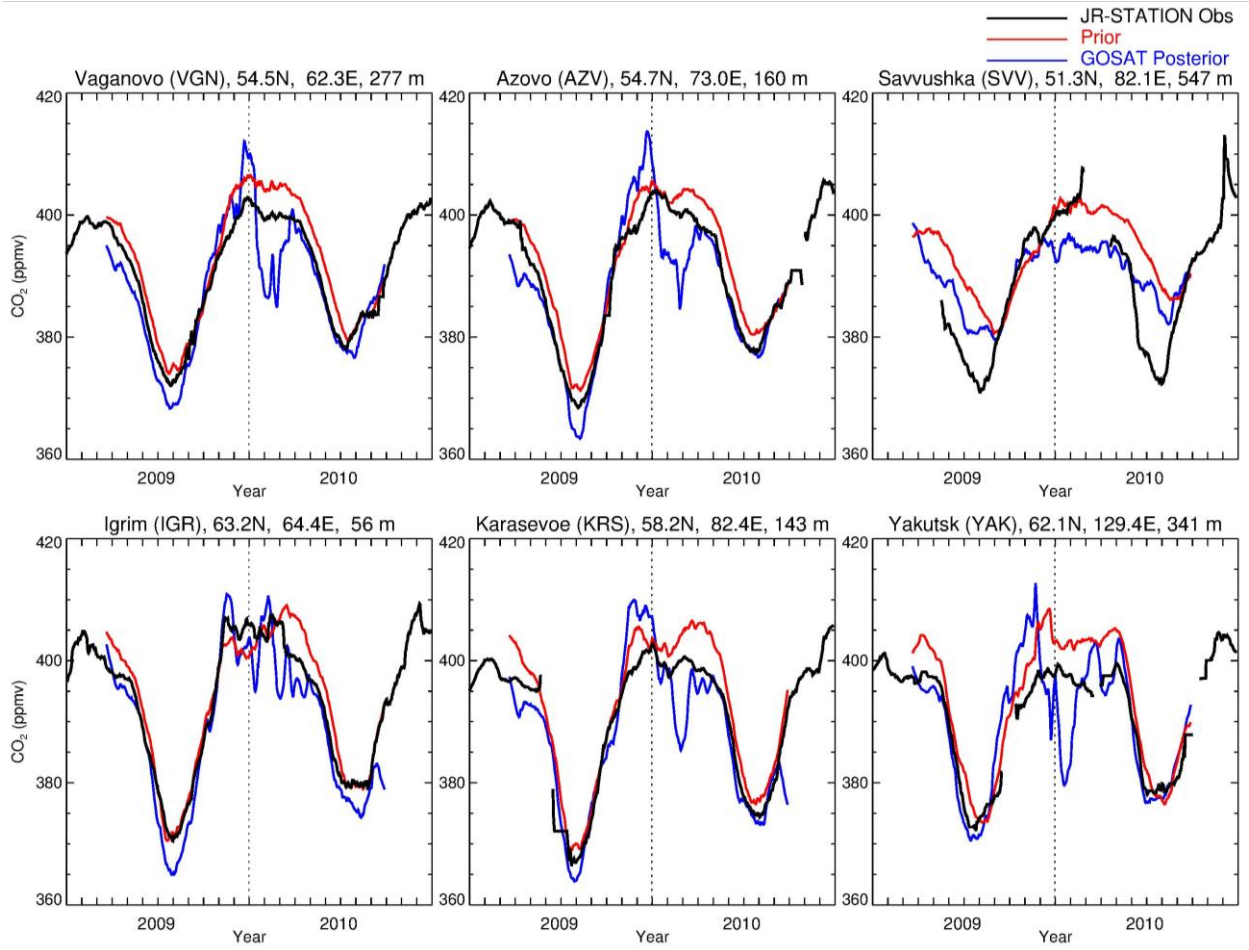

Figure 15. Evaluation of the prior model and GOSAT-only inversion against JR-STATION in situ observations in Siberia. Shown are daily afternoon average (1200-1700 local time) mole fractions from the highest level on each tower, the time series of which are smoothed with a 31-day window. Sites are arranged from west to east, first at lower latitudes and then at higher latitudes, excluding those with data gaps in the summer. Elevations shown include intake heights on towers.

Table S1. In Situ Observation Sites Used in Inversions.

Site Code[a]	Name and Country	Latitude	Longitude	Elevation (m ASL)	Agency	Obs Type[b]	Mismatch (ppm)[c]
ABP	Arembepe, Bahia, Brazil	-12.77	-38.17	1	NOAA	F	1.25
ALT	Alert, Nunavut, Canada	82.45	-62.52	190	NOAA	F	0.75
AMT107	Argyle, Maine, U.S.	45.03	-68.68	53	NOAA	C	--
ASC	Ascension Island, UK	-7.97	-14.4	85	NOAA	F	0.4
ASK	Assekrem, Algeria	23.18	5.42	2710	NOAA	F	0.75
AZR	Terceira Island, Azores, Portugal	38.77	-27.38	19	NOAA	F	0.75
BAL	Baltic Sea, Poland	55.35	17.22	3	NOAA	F	4
BAO300	Boulder Atmospheric Observatory, Colorado, U.S.	40.05	-105	1584	NOAA	C	--
BKT	Bukit Kototabang, Indonesia	-0.2	100.32	845	NOAA	F	4
BMW	Tudor Hill, Bermuda, UK	32.27	-64.88	30	NOAA	F	0.75
BRW	Barrow, Alaska, U.S.	71.32	-156.6	11	NOAA	F	0.75
BSC	Black Sea, Constanta, Romania	44.17	28.67	0	NOAA	F	4
CBA	Cold Bay, Alaska, U.S.	55.2	-162.72	21	NOAA	F	0.75
CGO	Cape Grim, Tasmania, Australia	-40.68	144.69	94	NOAA	F	0.4
CHR	Christmas Island, Kiribati	1.7	-157.17	0	NOAA	F	0.4
CIB	Centro de Investigacion de la Baja Atmosfera, Spain	41.81	-4.93	845	NOAA	F	2.5
CPT	Cape Point, South Africa	-34.35	18.49	230	NOAA	F	0.75
CRZ	Crozet Island, France	-46.45	51.85	197	NOAA	F	0.4
DRP	Drake Passage	-59	-64.69	0	NOAA	F	0.4
DSI	Dongsha Island, Taiwan	20.7	116.73	3	NOAA	F	0.75
EIC	Easter Island, Chile	-27.15	-109.45	47	NOAA	F	0.75
GMI	Guam, Mariana Islands	13.43	144.78	0	NOAA	F	0.75
HBA	Halley Station, Antarctica, UK	-75.58	-26.21	30	NOAA	F	0.4
HPB	Hohenpeissenberg, Germany	47.8	11.01	936	NOAA	F	4

HSU	Humboldt State University, U.S.	41.06	-124.75	0	NOAA	F	0.75
HUN	Hegyhatsal, Hungary	46.95	16.65	248	NOAA	F	4
ICE	Storhofdi, Vestmannaeyjar, Iceland	63.4	-20.29	118	NOAA	F	0.75
IZO	Izana, Tenerife, Canary Islands, Spain	28.3	-16.48	2373	NOAA	F	0.75
KEY	Key Biscayne, Florida, U.S.	25.67	-80.2	1	NOAA	F	1.25
KUM	Cape Kumukahi, Hawaii, U.S.	19.52	-154.82	3	NOAA	F	0.75
KZD	Sary Taukum, Kazakhstan	44.45	77.57	595	NOAA	F	1.25
KZM	Plateau Assy, Kazakhstan	43.25	77.88	2519	NOAA	F	1.25
LEF396	Park Falls, Wisconsin, U.S.	45.93	-90.27	472	NOAA	C	--
LLB	Lac La Biche, Alberta, Canada	54.95	-112.45	540	NOAA	F	1.5
LLN	Lulin, Taiwan	23.47	120.87	2862	NOAA	F	1.25
LMP	Lampedusa, Italy	35.52	12.62	45	NOAA	F	0.75
MEX	High Altitude Global Climate Observation Center, Mexico	18.98	-97.31	4464	NOAA	F	1.25
MHD	Mace Head, County Galway, Ireland	53.33	-9.9	5	NOAA	F	1.25
MID	Sand Island, Midway, U.S.	28.21	-177.38	11	NOAA	F	0.75
MKN	Mt. Kenya, Kenya	-0.05	37.3	3644	NOAA	F	1.25
MLO	Mauna Loa, Hawaii, U.S.	19.54	-155.58	3397	NOAA	F	0.75
MNM	Minamitorishima, Japan	24.3	153.97	8	JMA	C	--
NAT	Farol De Mae Luiza Lighthouse, Brazil	-5.51	-35.26	50	NOAA	F	0.75
NMB	Gobabeb, Namibia	-23.58	15.03	456	NOAA	F	1.25
NWR	Niwot Ridge, Colorado, U.S.	40.05	-105.58	3523	NOAA	F	0.75
OXK	Ochsenkopf, Germany	50.07	11.8	1022	NOAA	F	1.25
PAL	Pallas-Sammaltunturi, GAW Station, Finland	67.97	24.12	565	NOAA	F	1.25
POCN00	Pacific Ocean (0 N)	0	-163	10	NOAA	F	0.4
POCN05	Pacific Ocean (5 N)	5	-158	10	NOAA	F	0.4
POCN10	Pacific Ocean (10 N)	10	-152	10	NOAA	F	0.4

POCN15	Pacific Ocean (15 N)	15	-147	10	NOAA	F	0.4
POCN20	Pacific Ocean (20 N)	20	-140	10	NOAA	F	0.4
POCN25	Pacific Ocean (25 N)	25	-134	10	NOAA	F	0.4
POCN30	Pacific Ocean (30 N)	30	-126	10	NOAA	F	0.4
POCS05	Pacific Ocean (5 S)	-5	-168	10	NOAA	F	0.4
POCS10	Pacific Ocean (10 S)	-10	-174	10	NOAA	F	0.4
POCS15	Pacific Ocean (15 S)	-15	-178	10	NOAA	F	0.4
POCS20	Pacific Ocean (20 S)	-20	-178.5	10	NOAA	F	0.4
POCS25	Pacific Ocean (25 S)	-25	174	10	NOAA	F	0.4
POCS30	Pacific Ocean (30 S)	-30	169	10	NOAA	F	0.4
PSA	Palmer Station, Antarctica, U.S.	-64.92	-64	10	NOAA	F	0.4
PTA	Point Arena, California, U.S.	38.95	-126.23	17	NOAA	F	2.5
RPB	Ragged Point, Barbados	13.17	-59.43	15	NOAA	F	0.75
RYO	Ryori, Japan	39.03	141.83	260	JMA	C	--
SCT305	Beech Island, South Carolina, U.S.	33.41	-81.83	115	NOAA	C	--
SDZ	Shangdianzi, China	40.65	117.12	293	NOAA	F	4
SEY	Mahe Island, Seychelles	-4.67	55.17	2	NOAA	F	0.4
SGP	Southern Great Plains, Oklahoma, U.S.	36.8	-97.5	314	NOAA	F	1.25
SHM	Shemya Island, Alaska, U.S.	52.72	174.1	23	NOAA	F	1.25
SMO	Tutuila, American Samoa	-14.24	-170.57	42	NOAA	F	0.4
SPO	South Pole, Antarctica, U.S.	-89.98	-24.8	2810	NOAA	F	0.4
STM	Ocean Station M, Norway	66	2	0	NOAA	F	0.75
SUM	Summit, Greenland	72.58	-38.48	3210	NOAA	F	0.75
SYO	Syowa Station, Antarctica, Japan	-69.01	39.58	14	NOAA	F	0.4
TAP	Tae-ahn Peninsula, Republic of Korea	36.73	126.13	16	NOAA	F	4
TDF	Tierra del Fuego, Argentina	-54.87	-68.48	20	NOAA	F	0.4
THD	Trinidad Head, California, U.S.	41.05	-124.15	107	NOAA	F	1.25
UTA	Wendover, Utah, U.S.	39.9	-113.72	1327	NOAA	F	1.25
UUM	Ulaan Uul, Mongolia	44.45	111.1	1007	NOAA	F	1.25

WBI379	West Branch, Iowa, U.S.	41.72	-91.35	242	NOAA	C	--
WGC483	Walnut Grove, California, U.S.	38.27	-121.49	0	NOAA	C	--
WIS	Weizmann Institute of Science at the Arava Institute, Ketura, Israel	31.13	34.88	151	NOAA	F	1.25
WKT457	Moody, Texas, U.S.	31.32	-97.33	251	NOAA	C	--
WLG	Mt. Waliguan, China	36.29	100.9	3810	NOAA	F	1.25
YON	Yonagunijima, Japan	24.47	123.02	30	JMA	C	--
ZEP	Ny-Alesund, Svalbard, Norway and Sweden	78.91	11.88	474	NOAA	F	0.75

[a] Tower intake height appended where relevant

[b] F = Flask, C = Continuous

[c] Model-data mismatch component of observation error

Site Code[a]	Name and Country	Latitude	Longitude	Elevation (m ASL)	Agency	Obs Type[b]	Mismatch (ppm)[c]	Mean Total Uncertainty (ppm)[d]
ABP	Arembepe, Bahia, Brazil	-12.77	-38.17	1	NOAA	F	1.25	2.50
ALT	Alert, Nunavut, Canada	82.45	-62.52	190	NOAA	F	0.75	1.51
AMT107	Argyle, Maine, U.S.	45.03	-68.68	53	NOAA	C	--	1.09
ASC	Ascension Island, UK	-7.97	-14.4	85	NOAA	F	0.4	0.82
ASK	Assekrem, Algeria	23.18	5.42	2710	NOAA	F	0.75	1.52
AZR	Terceira Island, Azores, Portugal	38.77	-27.38	19	NOAA	F	0.75	1.50
BAL	Baltic Sea, Poland	55.35	17.22	3	NOAA	F	4	8.03
BAO300	Boulder Atmospheric Observatory, Colorado, U.S.	40.05	-105	1584	NOAA	C	--	2.00
BKT	Bukit Kototabang, Indonesia	-0.2	100.32	845	NOAA	F	4	8.01
BMW	Tudor Hill, Bermuda, UK	32.27	-64.88	30	NOAA	F	0.75	1.53
BRW	Barrow, Alaska, U.S.	71.32	-156.6	11	NOAA	F	0.75	1.53
BSC	Black Sea, Constanta, Romania	44.17	28.67	0	NOAA	F	4	8.01
CBA	Cold Bay, Alaska, U.S.	55.2	-162.72	21	NOAA	F	0.75	1.51
CGO	Cape Grim, Tasmania, Australia	-40.68	144.69	94	NOAA	F	0.4	0.82
CHR	Christmas Island, Kiribati	1.7	-157.17	0	NOAA	F	0.4	0.82

CIB	Centro de Investigacion de la Baja Atmosfera, Spain	41.81	-4.93	845	NOAA	F	2.5	5.01
CPT	Cape Point, South Africa	-34.35	18.49	230	NOAA	F	0.75	1.51
CRZ	Crozet Island, France	-46.45	51.85	197	NOAA	F	0.4	0.82
DRP	Drake Passage	-59	-64.69	0	NOAA	F	0.4	0.83
DSI	Dongsha Island, Taiwan	20.7	116.73	3	NOAA	F	0.75	1.52
EIC	Easter Island, Chile	-27.15	-109.45	47	NOAA	F	0.75	1.53
GMI	Guam, Mariana Islands	13.43	144.78	0	NOAA	F	0.75	1.52
HBA	Halley Station, Antarctica, UK	-75.58	-26.21	30	NOAA	F	0.4	0.81
HPB	Hohenpeissenberg, Germany	47.8	11.01	936	NOAA	F	4	8.01
HSU	Humboldt State University, U.S.	41.06	-124.75	0	NOAA	F	0.75	1.52
HUN	Hegyhatsal, Hungary	46.95	16.65	248	NOAA	F	4	8.00
ICE	Storhofdi, Vestmannaeyjar, Iceland	63.4	-20.29	118	NOAA	F	0.75	1.51
IZO	Izana, Tenerife, Canary Islands, Spain	28.3	-16.48	2373	NOAA	F	0.75	1.52
KEY	Key Biscayne, Florida, U.S.	25.67	-80.2	1	NOAA	F	1.25	2.51
KUM	Cape Kumukahi, Hawaii, U.S.	19.52	-154.82	3	NOAA	F	0.75	1.62
KZD	Sary Taukum, Kazakhstan	44.45	77.57	595	NOAA	F	1.25	2.52
KZM	Plateau Assy, Kazakhstan	43.25	77.88	2519	NOAA	F	1.25	2.52
LEF396	Park Falls, Wisconsin, U.S.	45.93	-90.27	472	NOAA	C	--	0.94
LLB	Lac La Biche, Alberta, Canada	54.95	-112.45	540	NOAA	F	1.5	3.02
LLN	Lulin, Taiwan	23.47	120.87	2862	NOAA	F	1.25	2.53
LMP	Lampedusa, Italy	35.52	12.62	45	NOAA	F	0.75	1.51
MEX	High Altitude Global Climate Observation Center, Mexico	18.98	-97.31	4464	NOAA	F	1.25	2.51
MHD	Mace Head, County Galway, Ireland	53.33	-9.9	5	NOAA	F	1.25	2.51
MID	Sand Island, Midway, U.S.	28.21	-177.38	11	NOAA	F	0.75	1.52
MKN	Mt. Kenya, Kenya	-0.05	37.3	3644	NOAA	F	1.25	2.52
MLO	Mauna Loa, Hawaii, U.S.	19.54	-155.58	3397	NOAA	F	0.75	1.52
MNM	Minamitorishima, Japan	24.3	153.97	8	JMA	C	--	0.30
NAT	Farol De Mae Luiza Lighthouse, Brazil	-5.51	-35.26	50	NOAA	F	0.75	1.51

NMB	Gobabeb, Namibia	-23.58	15.03	456	NOAA	F	1.25	2.51
NWR	Niwot Ridge, Colorado, U.S.	40.05	-105.58	3523	NOAA	F	0.75	1.52
OXK	Ochsenkopf, Germany	50.07	11.8	1022	NOAA	F	1.25	2.52
PAL	Pallas-Sammaltunturi, GAW Station, Finland	67.97	24.12	565	NOAA	F	1.25	2.51
POCN00	Pacific Ocean (0 N)	0	-163	10	NOAA	F	0.4	0.82
POCN05	Pacific Ocean (5 N)	5	-158	10	NOAA	F	0.4	0.82
POCN10	Pacific Ocean (10 N)	10	-152	10	NOAA	F	0.4	0.85
POCN15	Pacific Ocean (15 N)	15	-147	10	NOAA	F	0.4	0.82
POCN20	Pacific Ocean (20 N)	20	-140	10	NOAA	F	0.4	0.84
POCN25	Pacific Ocean (25 N)	25	-134	10	NOAA	F	0.4	0.83
POCN30	Pacific Ocean (30 N)	30	-126	10	NOAA	F	0.4	0.83
POCS05	Pacific Ocean (5 S)	-5	-168	10	NOAA	F	0.4	0.82
POCS10	Pacific Ocean (10 S)	-10	-174	10	NOAA	F	0.4	0.80
POCS15	Pacific Ocean (15 S)	-15	-178	10	NOAA	F	0.4	0.82
POCS20	Pacific Ocean (20 S)	-20	-178.5	10	NOAA	F	0.4	0.84
POCS25	Pacific Ocean (25 S)	-25	174	10	NOAA	F	0.4	0.82
POCS30	Pacific Ocean (30 S)	-30	169	10	NOAA	F	0.4	0.85
PSA	Palmer Station, Antarctica, U.S.	-64.92	-64	10	NOAA	F	0.4	0.82
PTA	Point Arena, California, U.S.	38.95	-126.23	17	NOAA	F	2.5	5.01
RPB	Ragged Point, Barbados	13.17	-59.43	15	NOAA	F	0.75	1.51
RYO	Ryori, Japan	39.03	141.83	260	JMA	C	--	2.45
SCT305	Beech Island, South Carolina, U.S.	33.41	-81.83	115	NOAA	C	--	1.51
SDZ	Shangdianzi, China	40.65	117.12	293	NOAA	F	4	8.00
SEY	Mahe Island, Seychelles	-4.67	55.17	2	NOAA	F	0.4	0.82
SGP	Southern Great Plains, Oklahoma, U.S.	36.8	-97.5	314	NOAA	F	1.25	2.52
SHM	Shemya Island, Alaska, U.S.	52.72	174.1	23	NOAA	F	1.25	2.51
SMO	Tutuila, American Samoa	-14.24	-170.57	42	NOAA	F	0.4	0.81
SPO	South Pole, Antarctica, U.S.	-89.98	-24.8	2810	NOAA	F	0.4	0.81
STM	Ocean Station M, Norway	66	2	0	NOAA	F	0.75	1.50
SUM	Summit, Greenland	72.58	-38.48	3210	NOAA	F	0.75	1.51
SYO	Syowa Station, Antarctica, Japan	-69.01	39.58	14	NOAA	F	0.4	0.81
TAP	Tae-ahn Peninsula, Republic of Korea	36.73	126.13	16	NOAA	F	4	8.16
TDF	Tierra del Fuego, Argentina	-54.87	-68.48	20	NOAA	F	0.4	0.83

THD	Trinidad Head, California, U.S.	41.05	-124.15	107	NOAA	F	1.25	2.52
UTA	Wendover, Utah, U.S.	39.9	-113.72	1327	NOAA	F	1.25	2.52
UUM	Ulaan Uul, Mongolia	44.45	111.1	1007	NOAA	F	1.25	2.59
WBI379	West Branch, Iowa, U.S.	41.72	-91.35	242	NOAA	C	--	1.82
WGC483	Walnut Grove, California, U.S.	38.27	-121.49	0	NOAA	C	--	2.35
WIS	Weizmann Institute of Science at the Arava Institute, Ketura, Israel	31.13	34.88	151	NOAA	F	1.25	2.51
WKT457	Moody, Texas, U.S.	31.32	-97.33	251	NOAA	C	--	1.05
WLG	Mt. Waliguan, China	36.29	100.9	3810	NOAA	F	1.25	2.54
YON	Yonagunijima, Japan	24.47	123.02	30	JMA	C	--	1.08
ZEP	Ny-Alesund, Svalbard, Norway and Sweden	78.91	11.88	474	NOAA	F	0.75	1.52

[a] Tower intake height appended where relevant

[b] F = Flask, C = Continuous

[c] Model-data mismatch component of observation error

[d] Includes factor of 2 overall increase

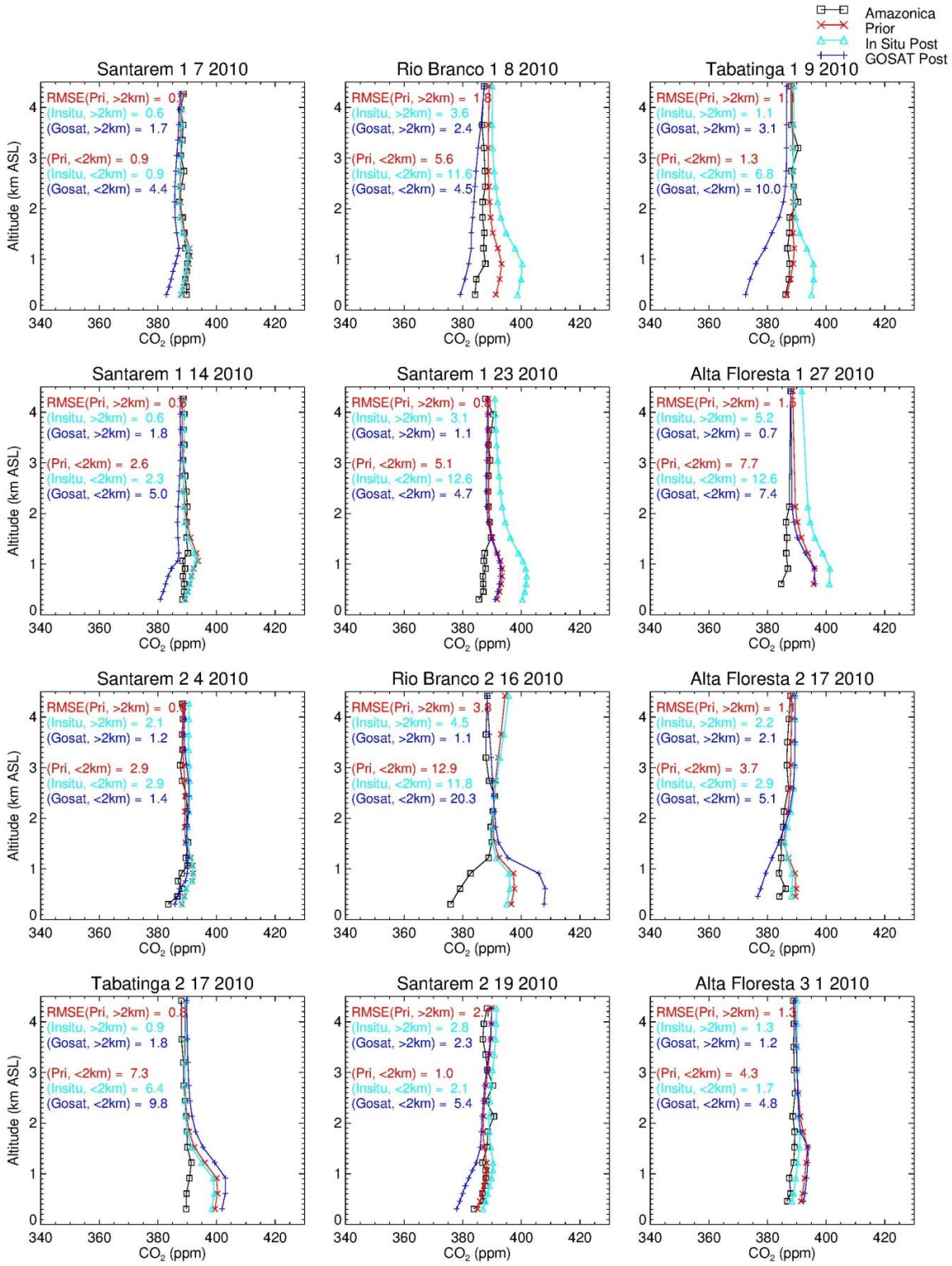

Figure S1. Comparison of prior, in situ-only posterior, GOSAT-only posterior, and Amazonica aircraft vertical profiles over 4 sites on different dates.

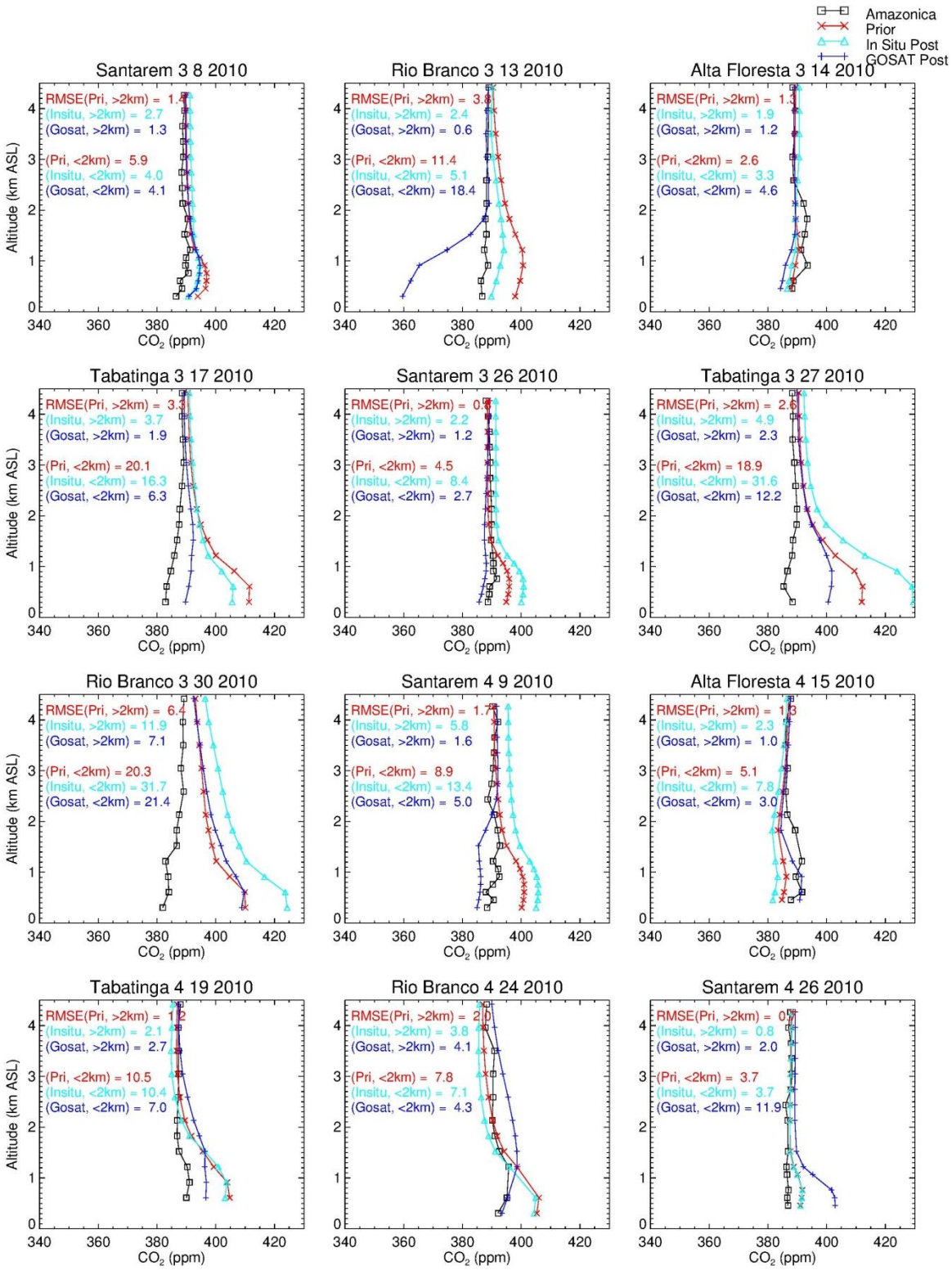

Figure S1. (continued)

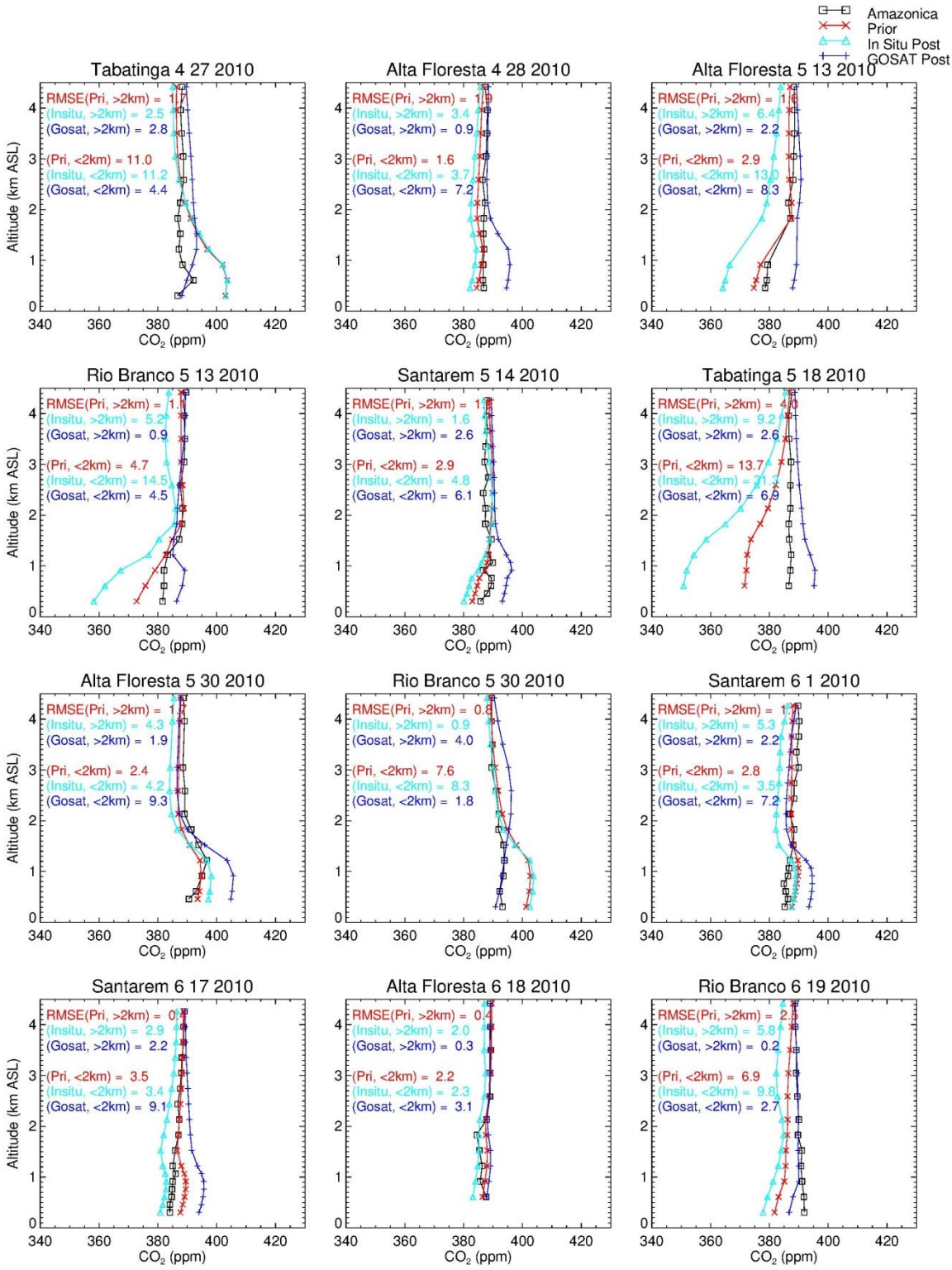

Figure S1. (continued)

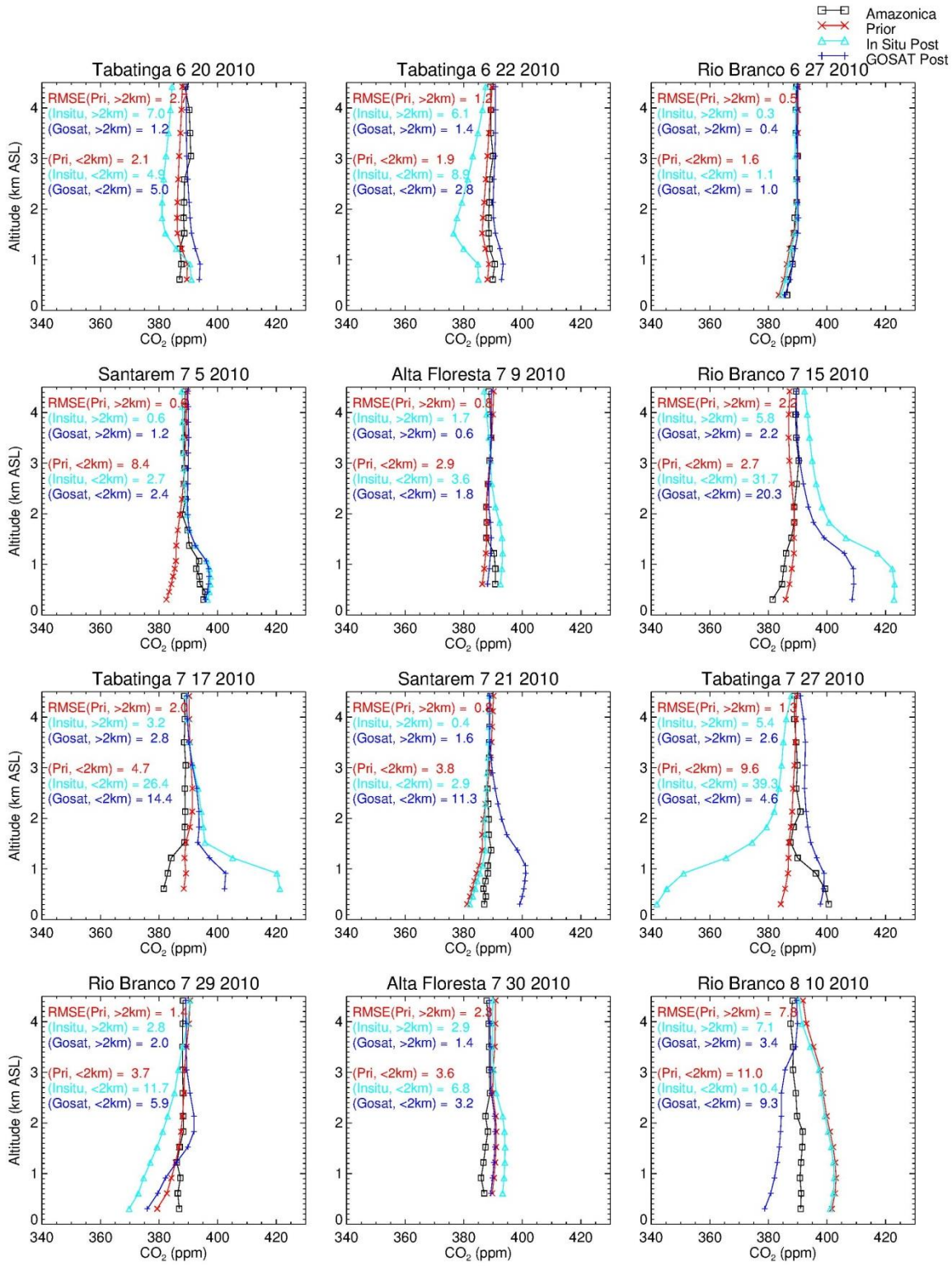

Figure S1. (continued)

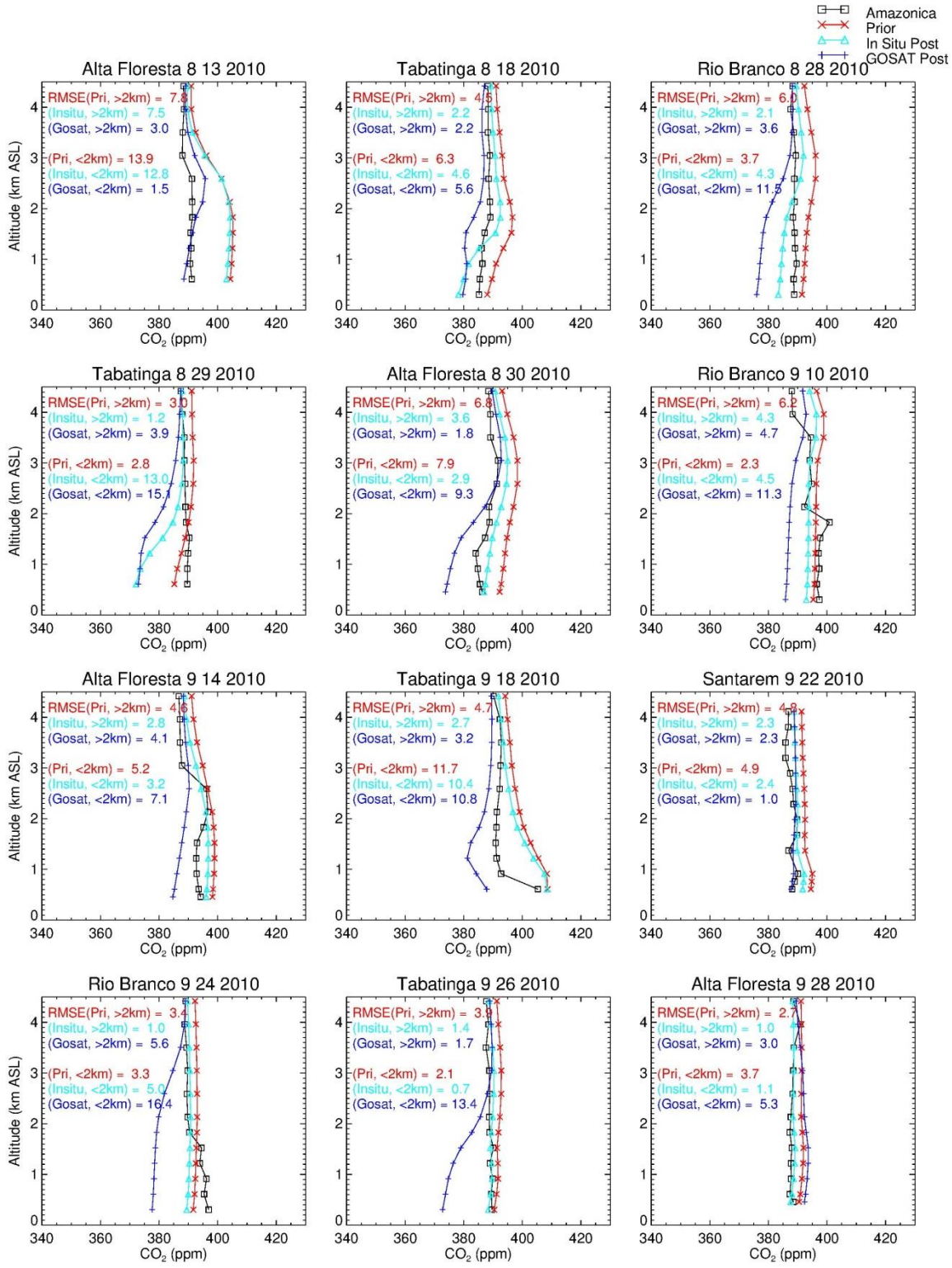

Figure S1. (continued)

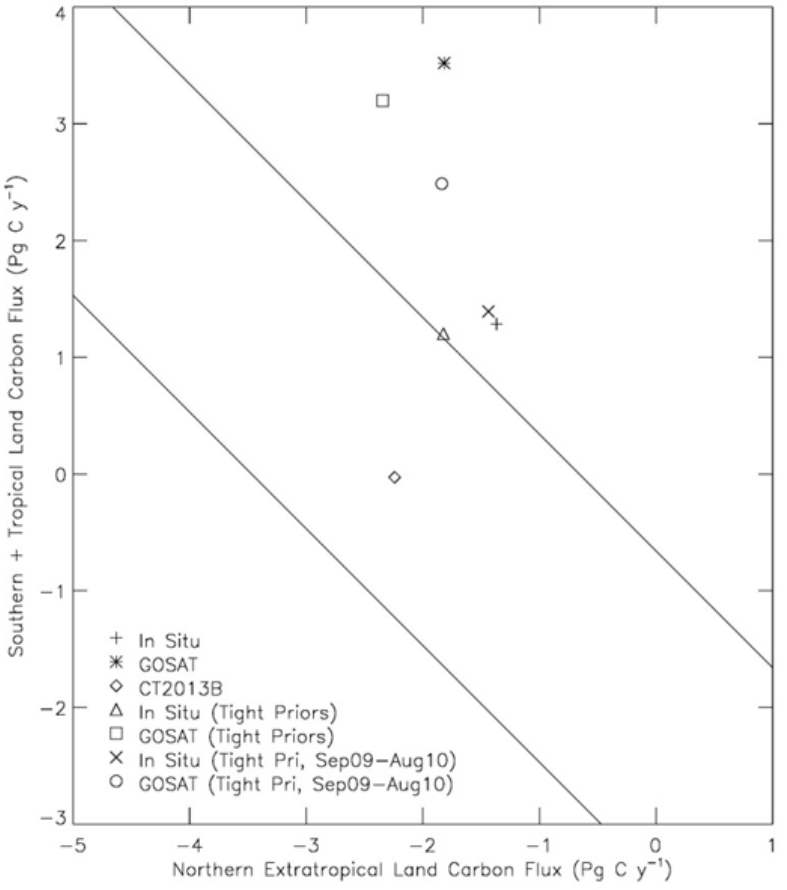

Figure S2. Posterior north-south land flux partitioning after Schimel et al. (2015). The diagonal lines are based on the global land carbon exchange (= land-use change emissions – land sink) estimated by GCP (2015) for the years relevant to the present analysis, i.e. 2009 and 2010, ± 1σ. Fluxes are for June 2009-May 2010 except where specified in the legend (for September 2009-August 2010). CT2013B refers to the CarbonTracker data assimilation system.

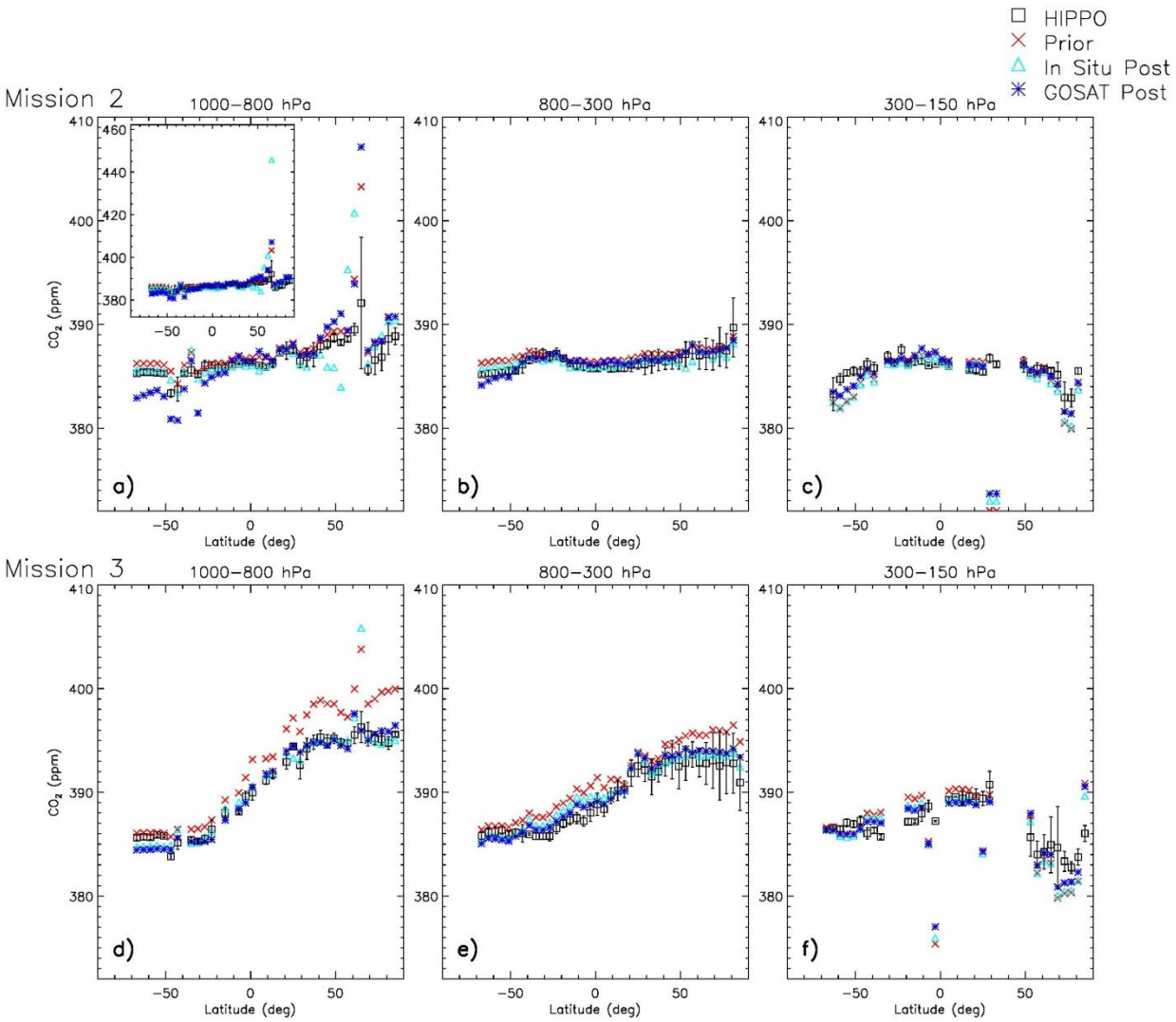

Figure S3. Same as Fig. 10 except showing inversions with tighter prior uncertainties.

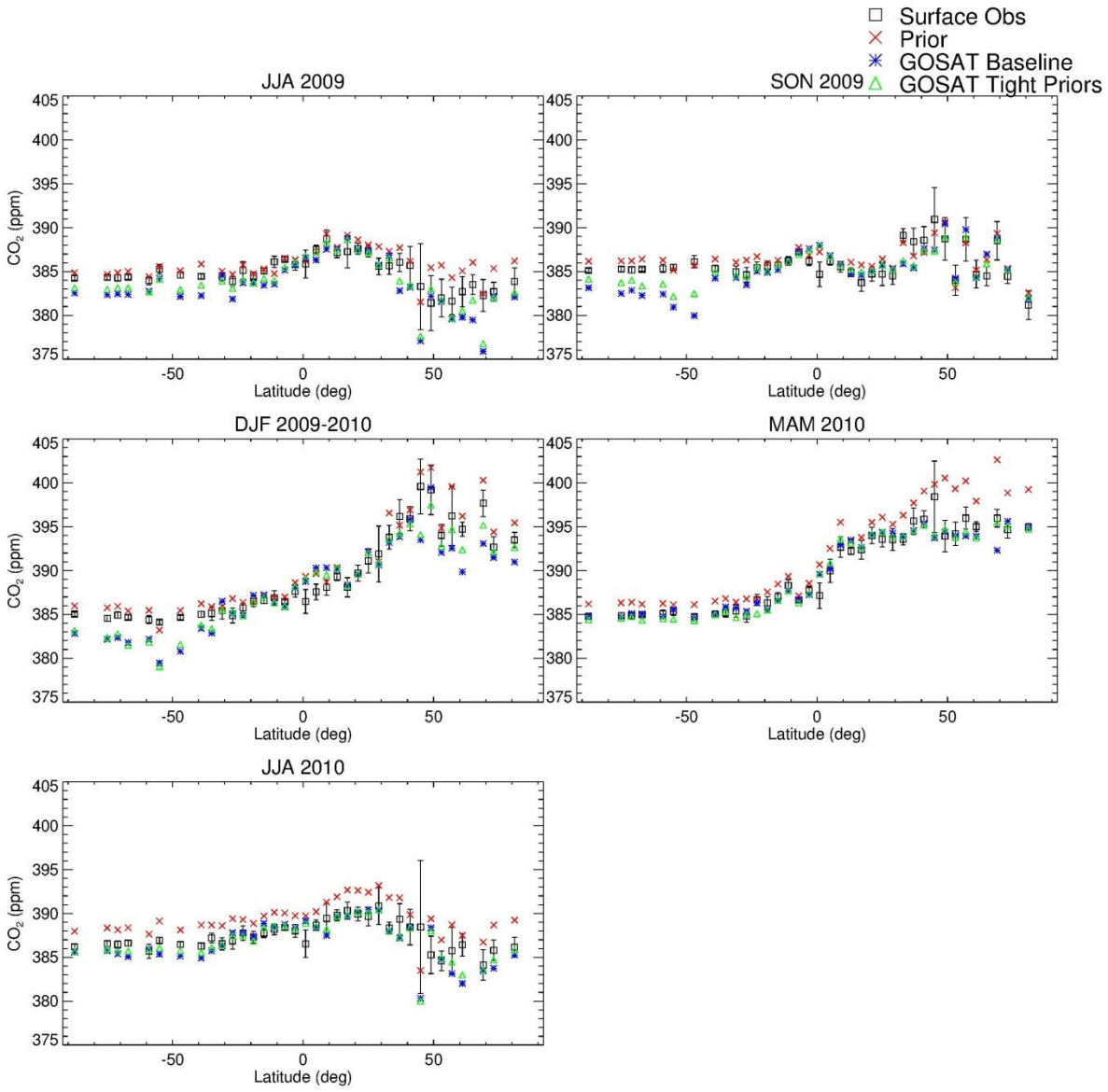

Figure S4. Same as Fig. 9 except showing GOSAT-only inversions with baseline vs. tighter prior uncertainties.